LBL-544

A PARTIAL WAVE ANALYSIS OF THE REACTION $\pi N \rightarrow N\pi\pi$ IN THE CMS ENERGY RANGE 1.6 BeV TO 2.0 BeV

David J. Herndon
(Ph.D. thesis)

May 30, 1972

AEC Contract No. W-7405-eng-48

DISCLAIMER

TABLE OF CONTENTS

A Partial Wave Analysis of the Reaction $\pi N \to N\pi\pi$ in the CMS Energy Range 1.6 BeV to 2.0 BeV

David J. Herndon

Lawrence Berkeley Laboratory

University of California

Berkeley, California

May 30, 1972

ABSTRACT

We present the results of an energy independent partial-wave analysis of the single-pion production reactions at nine center of mass energies from 1.6 to 2.0 GeV. This maximum likelihood analysis was based upon the Isobar Model. We use the results of a preliminary K-matrix analysis to remove the overall phase ambiguity at each of our energies. The Argand plots confirm the S11(2100) and P13(1850) resonances and show no evidence for the P31(1900) in our channels. There are indications of the existence of the D13(1700), badly needed by the quark model, and for a new P11 resonance around 2100 MeV.

INTRODUCTION

The πN elastic partial-wave analyses done during the middle 1960's generated great interest in a partial-wave analysis of the inelastic channels. These elastic analyses predicted a large number of new resonances with large couplings to the inelastic channels. The inelastic analyses would determine the couplings to the various inelastic channels and would determine the relative signs of the couplings.

This analysis concerns the single-pion production reactions. Of the five possible reactions,

$$\pi^- p \to n \pi^0 \pi^0 \qquad (1)$$
$$\to n \pi^- \pi^+ \qquad (2)$$
$$\to p \pi^- \pi^0 \qquad (3)$$
$$\pi^+ p \to p \pi^+ \pi^0 \qquad (4)$$
$$\to n \pi^+ \pi^+ \qquad (5)$$

we decided to look at reactions (2) and (3) in the region of the 1688 resonances. There are at least two dominant resonances, the D15 and F15, as well as other smaller resonances in this region. By using two channels, we hoped to be able to separate the Ispin -$\frac{1}{2}$ from the Ispin - $\frac{3}{2}$ contributions. At these energies we are far from threshold and many waves should be present, but we felt that with enough events we could separate the different waves. The practical reason for choosing this region was the large amount of LBL 72" hydrogen buble chamber film already exposed by others doing strange-particle analyses.

Looking at the data from the available 72" HBC film (fig 1), we see that it adequately covers only the lower half of the 1688 region. We proposed and were granted a run using the 30" MURA HBC at Argonne National Lab to fill in the gap in the 1688 data. Although the original proposal was expanded to include data from 1.4 to 2.0 GeV (fig 2), the data below 1.63 GeV was not sufficient to be used in the fitting. For a complete discussion of the data and its reduction see the paper by Brody et. al.[1]

After starting the analysis, we found that the π^- data alone was insufficient and that we also needed π^+ data. Bernard Deler was in Berkeley at that time and gave us ≈20000 π^+ events[2] covering our entire energy region. We later obtained ≈25000 π^+ events in the region 1.83 to 2.0 GeV from a UCR - LBL collaboration.[3] Table I and figures 3 - 6 give the breakdown by energy and reaction of all the data used. Mark numbers correspond to the reactions in equations 1 - 5, i.e. Mark 2 corresponds to $\pi^- p \to n\pi^-\pi^+$.

The analysis has progressed in three stages; program development, energy independent fitting, and energy dependent analysis. Because none of the available fitting programs could handle either the amount of data or the number of parameters (≤120) necessary for the analysis, Larry Miller wrote a new maximum likelihood fitting program.[4] While this work was going on, we developed as a framework for the analysis a generalized Isobar Model formalism[5] (hereafter called HSC) which allows arbitrary spins on all five particles.

Ronald Longacre[6] has written a program based upon the K-matrix formalism to do an energy dependent analysis of our final amplitudes. This report deals with the energy independent fitting and with the addition of an appendix on errors will appear as LBL-544. In the first section we develop the actual equations used in the analysis and discuss the fitting procedure. Section two is a discussion of our final amplitudes.

I. EQUATIONS AND PROCEDURES

We summarize the formalism of HSC for the general case of $a + b \to 1 + 2 + 3$ where a is the beam, b the target, and 1, 2, 3 are the three outgoing particles. We let j, k, l represent any cyclic permutation of 1, 2, 3. The diparticle (fig 7) is always composed of particles k and l with all diparticle quantities indexed by a subscript j. Figure 7 illustrates the following quantities and equation 6 relates the different angular momenta.

a. Total CMS energy and angular momentum - W, J

b. Four-momenta in CMS - $p_a\ p_b\ Q_j\ Q_k\ Q_l$

c. Particle spins - $\sigma_a\ \sigma_b\ \sigma_j\ \sigma_k\ \sigma_l$

d. Helicities in CMS - $\mu_a\ \mu_b\ \mu_j\ \mu_k\ \mu_l$

e. Mass of diparticle - w_j

f. Spin and CMS helicity of the diparticle - $j_j\ \lambda_j$

g. Incident orbital angular momentum and total spin - $L\ S$

h. Outgoing orbital angular momentum and total spin - $L_j\ S_j$

In the diparticle rest-frame we have the quantities

i. Four-momenta of the decay particles - $q_k\ q_l$

j. Helicities of the decay particles - $\nu_k\ \nu_l$

k. Orbital angular momentum and total spin of decay particles - $l_j\ s_j$

The angular momenta are coupled in the following manner:

$$\begin{aligned}
\vec{S} &= \vec{\sigma}_a + \vec{\sigma}_b \\
\vec{J} &= \vec{L} + \vec{S} \\
\vec{s}_j &= \vec{\sigma}_k + \vec{\sigma}_l \\
\vec{j}_j &= \vec{l}_j + \vec{s}_j \\
\vec{S}_j &= \vec{\sigma}_j + \vec{j}_j \\
\vec{J} &= \vec{L}_j + \vec{S}_j
\end{aligned} \qquad (6)$$

We assume that L, L_j, and l_j are chosen so as to conserve parity. We use μ with no subscript to represent a fixed set of all five helicities. The index n represents the set of quantities

$$n = (j;\ J;\ L\ S;\ L_j\ S_j;\ j_j\ l_j\ s_j). \qquad (7)$$

The differential cross-section is written as

$$d\sigma = \frac{\pi^2}{F}\ \bar{\sum_{\mu}}\ |f_\mu|^2\ dp \qquad (8)$$

where

$$\bar{\sum_{\mu}} = \frac{1}{(2\sigma_a+1)(2\sigma_b+1)}\ \sum_{\mu} \qquad (9)$$

and

$$f_\mu = \sum_n g_n^\mu\ T_n(W, \omega_j) \qquad (10)$$

The $T_n(W,w_j)$ are such that at a fixed energy W_o

$$\int |T_n(W_o,\omega_j)|^2 d\omega_j \leq 1/2 \qquad (11)$$

Letting p and Q_j be the magnitude of the incoming and outgoing momenta in the center of mass and q_k be the decay momentum in the diparticle rest-frame,

$$g_n^\mu = \frac{W}{\pi}\sqrt{\frac{\omega_j}{\pi p Q_j q_k}}\sqrt{(2L+1)(2L_j+1)(2l_j+1)}$$
$$C(\sigma_a,\sigma_b,S|\mu_a,-\mu_b)\,C(L,S,J|0,\mu_a-\mu_b)$$
$$\sum_{\lambda_j} C(\sigma_j,I_j,S_j|\mu_j,-\lambda_j)\,C(L_j,S_j,J|0,\mu_j-\lambda_j)\,\mathcal{D}^{J}_{\mu_j-\lambda_j\ \mu_a-\mu_b}(\alpha_j,\beta_j,\gamma_j) \qquad (12)$$
$$\sum_{\mu_k\mu_\ell} C(\sigma_k,\sigma_\ell,I_j|\mu_k,\mu_\ell)\,C(l_j,I_j,I_j|0,\mu_k-\mu_\ell)\,\mathcal{D}^{I_j}_{\mu_k-\mu_\ell}(\theta_j)$$
$$\mathcal{D}^{\sigma_k}_{\mu_k\mu_a}(\theta_j^k)\,\mathcal{D}^{\sigma_\ell}_{\mu_\ell\mu_b}(-\theta_j^k)\,\mathcal{D}^{I_j}_{(-1)^{\sigma_j}\lambda_j\ \mu_k-\mu_\ell}$$

Although not exact, we use the Watson final-state interaction term for the final-state enhancement factor. Since the Watson form includes the barrier factor for the decay, we only need to include the incoming and outgoing barrier terms. We used p^L and $Q_j{}^L{}_j$, but these are inadequate and should be corrected.[7] Explicitly writing the isospin vector addition coefficients and assuming no other w_j dependence, T_n can be written as

$$T_n(W,\omega_j) = C(I_a^a,I_b^b,I|I_z^a,I_z^b)\,C(I_j^j,I_j^D,I|I_z^j,I_z^k+I_z^\ell)$$
$$C(I_k^k,I_j^\ell,I^D|I_z^k,I_z^\ell)\,\frac{1}{4W}\,p^{L+\frac{1}{2}}\,Q_j^{L_j+\frac{1}{2}} \qquad (13)$$
$$\frac{e^{i\delta}\sin\delta}{q_k^{l_j+1}}\sqrt{\frac{q_k}{4\omega_j}}\;A_n(W)$$

Absorbing the factor $\frac{\pi^2}{F}(2\sigma_a+1)^{\frac{1}{2}}(2\sigma_b+1)^{\frac{1}{2}}$ into f_μ, we have

$$d\sigma = \sum_\mu |f_\mu'|^2\, d\rho \qquad (14)$$

where

$$f_\mu' = \sum_n X_{n\mu}\,A_n(W) \qquad (15)$$

and

$$X_{n\mu} = C(I_a^a,I_b^b,I|I_z^a,I_z^b)\,C(I_j^j,I_j^D,I|I_z^j,I_z^k+I_z^\ell)$$
$$C(I_k^k,I_j^\ell,I^D|I_z^k,I_z^\ell)\,\frac{4}{\sqrt{W\rho\pi}}\left[(2\sigma_a+1)(2\sigma_b+1)\right]^{-\frac{1}{2}}$$
$$p^L\,Q_j^{L_j}\,\frac{e^{i\delta}\sin\delta}{q_k^{l_j+1}}$$

$$\left[(2L+1)(2L_j+1)(2l_j+1)\right]^{\frac{1}{2}}\,C(\sigma_a,\sigma_b,S|\mu_a,-\mu_b)\,C(L,S,J|0,\mu_a-\mu_b) \qquad (16)$$
$$\sum_{\lambda_j} C(\sigma_j,I_j,S_j|\mu_j,-\lambda_j)\,C(L_j,S_j,J|0,\mu_j-\lambda_j)$$
$$\mathcal{D}^{J}_{\mu_j-\lambda_j\ \mu_a-\mu_b}(\alpha_j,\beta_j,\gamma_j)$$
$$\sum_{\mu_k\mu_\ell} C(\sigma_k,\sigma_\ell,I_j|\mu_k,-\mu_\ell)\,C(l_j,I_j,I_j|0,\mu_k-\mu_\ell)$$
$$\mathcal{D}^{I_j}_{-\lambda_j\ \mu_k-\mu_\ell}(\theta_j)\,\mathcal{D}^{\sigma_k}_{\mu_k\mu_a}(\theta_j^k)\,\mathcal{D}^{\sigma_\ell}_{\mu_\ell\mu_b}(-\theta_j^\ell)\,(-1)^{\sigma_\ell-\mu_\ell}$$

For our case with three of the five particles having zero spin, the expression for $X_{n\mu}$ is much simplier. Since we have divided the data into energy bins and are doing an energy independent analysis, we removed the term p^L as being constant over each bin and assumed that $A_n(W)$ is a constant for each bin. It is these constant A_n that are the actual fitting parameters.

Types of Diparticles We consider three final-state resonances: the $\Delta(1236)$ $(L+1, I=\frac{3}{2}, J=\frac{3}{2})$ πN resonance, the $\rho(760)$ $(L=I=J=1)$ resonance, and the $\sigma(800)$ $(L=I=J=0)$ $\pi\pi$ enhancement. In the case of the ρ there are two possible values for S_j, $\frac{1}{2}$ and $\frac{3}{2}$; these will be denoted by ρ_1 and ρ_3 respectively. We consider all waves with L and L_j less than 4 which meant 60 possible waves.

LL$_j$ (2J)

Δ	ρ_3	ρ_1	σ
PP 1	PP 1	SS 1	PS 1
SD 1	SD 1	PP 1	SP 1
DS 3	DS 3	PP 3	DP 3
PP 3	PP 3	DD 3	PD 3
DD 3	DD 3	DD 5	FD 5
PF 3	PF 3	FF 5	DF 5
FP 5	FP 5	FF 7	
DD 5	DD 5		
FF 5	FF 5		
FF 7	FF 7		
I = 1/2, 3/2	I = 1/2, 3/2	I = 1/2, 3/2	I = 1/2
10 waves x 2 isospins = 20	+ 10 waves x 2 isospins = 20	+ 7 waves x 2 isospins = 14	+ 6 waves x 1 isospin = 6

We use a seven-character label for each wave. The first three characters designate the type of diparticle, P33, RH3, RH1, SIG; the last four characters are L, L_j, (2I), and (2J). Thus an incoming F15 wave going to a $\Delta\pi$ final state with $L_j = 1$ is denoted by P33 FP15. These labels appear at the lower left of each Argand plot.

For the Delta phase in the Watson final-state interaction term, we used a table look-up from CERN-TH[8] with linear interpolation (quadratic interpolation from threshold to 1.089 GeV.) For energies above 1.794 GeV, we fixed $\delta = 180°$. Figure 8 gives δ and $e^{i\delta}\sin\delta/q^{2l+1}$ for the Delta. Figure 9 shows the same plots for the Rho. The Rho phases come from the parametrization of Morgan,[9]

$$\cot\delta = \frac{(m_\pi^2 - 0.1536q^2)(m_\pi^2 + 0.028q^2)\sqrt{m_\pi^2+q^2}}{0.035\, m_\pi^2\, q^3} \qquad (17)$$

For the Sigma (now called the ε), we split the energy region into three parts. For energies above 0.66 GeV, we used the phase from a Breit-Wigner with $E_r = 0.9$ GeV and $\Gamma_r = 0.74$ GeV.

$$\cot\delta = 2(0.9 - \omega_\sigma)/0.74 \qquad (18)$$

This form was chosen to correspond to the old "up-down" solution. For energies below 0.4 GeV, we used a scattering length approximation,

$$\frac{q}{\omega_\sigma}\cot\delta = \frac{1}{0.32} - 109.5q^2 + 1114.0q^4 \qquad (19)$$

The constant term corresponds to a scattering length $a_o = 0.16$.[9] The other two terms were added to give a smooth joining of equations 18 and 19 at 0.53 GeV. Rather than actually extending each form to 0.53 GeV, we drew a hand-drawn curve between 0.4 and 0.66 GeV and used a table look-up with linear interpolation from points on this curve.

There has recently been a new coupled channel analysis of the $\pi\pi$ and $K\bar{K}$ channels by Serban Protopopescu.[10] Any new analysis should use the new values for the phases. Figure 10 shows our final-state factor for the Sigma with the new phases plotted as a dashed curve on the phase plot. Our fits are reasonably insensitive to changes in the phases and thus our fits would not be changed by using the new phases.

Symmetry Check Since we always maintain the cyclic order of 1, 2, 3, we need to check the behavoir of f'_μ under interchange of the two pions. Equations 74 - 76 of HSC give the effect on g^μ_n of interchanging the pions, whicle the Ispin vector addition coefficients give a factor $(-1)^{I^R+I^R-I^D}$. Thus, letting μ_i = the incident nucleon helicity, and μ_f = the final nucleon helicity, we have under interchange

$$X_{n\mu}(\Delta_1) \to (-1)^{-\mu_i+\mu_f}(-1)^{\ell_\Delta}(-1)(-1)^{I^\pi+I^N-I^\Delta}X_{n\mu}(\Delta_2) = (-1)^{\mu_i-\mu_f}X_{n\mu}(\Delta_2)$$

$$X_{n\mu}(\Delta_2) \to (-1)^{-\mu_i+\mu_f}(-1)^{\ell_\Delta}(-1)(-1)^{I^\pi+I^N-I^\Delta}X_{n\mu}(\Delta_1) = (-1)^{-\mu_i-\mu_f}X_{n\mu}(\Delta_1)$$

$$X_{n\mu}(\rho) \to (-1)^{\mu_i-\mu_f}(-1)^{\ell_\rho}(-1)^{I^\pi+I^\pi-I^\rho}X_{n\mu}(\rho) = (-1)^{-\mu_i-\mu_f}X_{n\mu}(\rho) \qquad (20)$$

$$X_{n\mu}(\sigma) \to (-1)^{-\mu_i-\mu_f}(-1)^{\ell_\sigma}(-1)^{I^\pi+I^\pi-I^\sigma}X_{n\mu}(\sigma) = (-1)^{\mu_i-\mu_f}X_{n\mu}(\sigma)$$

Thus

$$f'_\mu \to (-1)^{\mu_i-\mu_f} f'_\mu \qquad (21)$$

and since we are only interested in unpolarized cross-sections, the overall phase change is unimportant.

Cross-check of Programs As a check on our amplitude program, we obtained the amplitude programs from three other analyses.[11-13] Although for a given event we could not check the quantities $X_{n\mu}$ directly (we used a different coordinate system), we could compare the quantities

$$s_i = \sum_\mu |X_{n\mu}|^2 \qquad (22)$$

To eliminate any extra constant factors, we used the ratio of each quantity to the corresponding quantity for the first event, s_i / s_1. After correcting the bugs in our program and one in a new addition to the Deler programs, we got agreement for all waves individually. To check for relative sign differences between different waves, we also made the same check for various combinations of waves. Again in all cases we got agreement.

Monte Carlo Fitting Test To test the fitting programs and to establish the best technique for fitting, we generated artificial data from eleven "known" amplitudes (see fig 11) and then fit for these amplitudes. To generate these data, we took a sample of Monte Carlo events generated uniformly over phase space and formed the probability ratio p_i / p_{max}, where the probability p_i for the

i^{th} event is

$$P_i = \sum_{\mu} |f_{\mu}'|^2 \qquad (23)$$

When p_i / p_{max} was greater than a generated random number, the event was kept as part of the artificial data. In this manner we generated 4733 Mark 2 events and 2850 Mark 3 events.

To obtain a set of reasonable starting values for fitting the artificial data, we randomly generated 2000 sets of A's and kept the twenty sets with the highest likelihood. These twenty sets typically reduced to five separate solutions after fitting. Any wave, for which the modulus was within one standard deviation of zero in at least three of the five solutions, was considered statistically insignificant and eliminated. After elimination, we refit with fewer waves and again tried to eliminate waves. In the end the five separate solutions has coalesced into one solution, and the number of waves had reduced from 60 to 24. These 24 waves consisted of the original eleven waves and another thirteen extra waves each of which had $|T| < 0.028$. Figure 12a shows the fitted amplitudes corresponding to the original eleven waves and figure 12b shows the extra thirteen waves. On all Argand plots, the scale maximum is given at the lower right.

Fitting For our first attempts at fitting the data we chose energy bins 20 MeV wide. We were unable to get satisfactory fits as discussed by Miller.[4] We recombined the data into bins 40 MeV wide and we label each bin by its midpoint, eg. 1650.

Initially we worked with just the five lowest bins, 1650 - 1810. At each energy we generated 2000 random sets of starting A's and, using

those with the highest likelihood, fit with as many sets as necessary to generate five distinct 60-wave solutions. At each energy, we then made a list of all waves whose modulus was within 1.25 standard deviations of zero in any of the five solutions. Any wave which was considered statistically insignificant in a majority (3/5) of the energy bins was then eliminated and the whole procedure repeated. In the case of the rho waves, we have the problem of the two types of waves, RH1 and RH3. In all cases in which the different types also had different L_j values, the program chose the wave with the lower value of L_j. In the three cases, P13, P31, and F37, in which both rho waves have the same value of L_j, we fit with only one wave and then with only the other wave choosing that wave giving the higher likelihood in a majority of the energy bins. In all cases the difference in likelihoods was insignificant and the fits would be unchanged if the other wave was used. Using this technique we reduced the number of waves from 60 to 30.

At this point we still had three or four solutions at each energy. To look for continuity, we used each solution as a starting value in the energy bin above and below its own. In this manner we were able to find a continuous chain over all five energies. Except for 1730 which had two solutions (one when going up from 1690 and one when coming down from 1770) each energy had just one solution which fit into the chain.

We were now ready to try the four highest energies, 1850 - 1970. Again we generated 2000 random sets of A's but, because of computer

time, kept only enough sets to give four separate solutions after fitting. Rather than again going through the procedure of eliminating waves, we tried to use the 30 waves from the lower energies plus the F35 and F37 waves which had not been used at the lower energies. By eliminating some waves and extending the new waves down to the lower bins, we were able to get a 28 wave chain that included eight of the nine bins. It was impossible to include 1930 in the chain. By looking at plots of the amplitudes we removed any wave which seemed small at all energies and any wave whose behavoir was erratic. We also removed the F35 and F37 waves from the lowest two bins. This reduced the number of waves to 24 (23 at 1730 and 20 at 1650 and 1690.) We were now able to include 1930 in the chain and to resolve the ambiguity at 1730. The chain was completely continuous upwards and downwards in energy.

We need to check our judgement in removing the waves. The effect on both χ^2 and the likelihood are discussed in detail in ref. 6, but here we give brief re-assurance. Taking the log of the likelihood, we have

$$\ln \mathcal{L} = F = -\frac{\chi^2}{2} + \text{Constant} \qquad (24)$$

Thus any wave (2 parameters) that is statistically insignificant should cause a change in F of ≈1 when removed. We find that the change from 30 waves to 28 waves caused a change in F of about 10 or 5/wave. On the other hand, the reduction of 24 waves caused a change in F of 25/wave at 1650 up to 50/wave at 1970. Clearly we are removing waves which the program feels are needed. As a check to see how important these changes really are, we removed the

P33 DD15 wave at 1650 and the P33 FP15 wave at 1690. Since the P33 DD15 wave is the only D15 wave and since it is large at 1650, one would expect a drastic change in F. The P33 FP15, however, is one of three F15 waves and is only "medium" in size, and one would expect a smaller change in F. The changes were 584 and 186 respectively. Thus it appears that we did not remove any waves that were really needed by the fit.

During the fitting, we imposed a unitarity constraint. We added for each incoming partial wave an extra term in the likelihood of the form

$$e^{-\alpha^2\left(\frac{\sigma_{INEL}-\sigma_{CALC}}{\delta\sigma_{INEL}}\right)^2} \qquad (25$$

σ_{inel} and $\delta\sigma_{inel}$ came from averaging the inelastic cross-sections predicted by the different elastic phase-shift analyses[8] and using their external error. The parameter α was taken to be zero if $\sigma_{inel} > \sigma_{calc}$, and for $\sigma_{inel} < \sigma_{calc}$, we adjusted α so that $\delta\sigma_{inel} = \alpha\,\delta\sigma_{calc}$. When we removed the small F35 waves at 1650 and 1690, the F15 cross-section increased and at 1690 it just violates unitarity.

The fitting program, RUMBLE, is designed to be invariant to overall scale changes in the amplitudes.[4] After fitting, we must normalize the final fitted amplitudes to the known cross-sections. For our fits, RUMBLE adjusts the scale factor so that the sum of the claculated cross-sections for channels 2, 3, and 4 equals the sum of the experimental cross-sections for these channels. Table II

gives the values of the input cross-sections and the final calculated values. Figures 13 - 17 give the experimental cross-sections for each channel with our calculated cross-sections, σ_{calc}, marked by x's. We are always low in our claculated value of the $\pi^+p \to n\pi^+\pi^+$ cross-section, and it gets worse as the energy increases. This is probably due to an increasing contribution to the cross-section from the $N^*\pi$ channels.

II. RESULTS

To get a feeling for the quality of our fits, Larry Miller wrote a program[15] that allows one to bin the data in up to four variables and to then compare the actual bin population to a predicted bin population. The predicted population is obtained by binning Monte Carlo events, each weighted by p_i (see eq. 21.) For our four variables, we chose Φ, $\cos\theta$, $M(N\pi)$, and $M(\pi\pi)$ where (θ,Φ) are the angles of the beam and the π in the $(N\pi)$ combination has the same sign as the beam. Figures 18 - 23 show these comparisons for Marks 2, 3, and 4 at 1690 and 1930. Figure a is always the four-dimensional plot and figures b and c are the two two-dimensional plots. To ensure enough statistics in each bin, the four-dimensional plots have each variable divided into only four bins and the two-dimensional plots have each variable divided into ten bins. In each bin the dashed tombstone indicates the real event population and the solid tombstone indicates the predicted population. The population is proportional not to the area but to the height (or width) of the tombstone. To the

top and right of each two-dimensional plot are the projections of what is below and to the left. With the increase in statistics due to making projections, the number of bins is increased. From the figures, we see that our solution predicts the distribution of events well in all areas of the four-dimensional kinematic space in all three channels.

By doing an energy independent analysis, one is unable to determine the relative phase between fits at different energies. Thus one is unable to make Argand plots and to look for resonances. One can, however, use the less reliable method of plotting $|T|^2$ and looking for resonance bumps. One can also compare the calculated inelastic cross-section, σ_{calc}, with the cross-section predicted by the elastic analyses, σ_{inel}. We have included both types of plots in figures 29 - 40.

Since Argand plots are so useful, one looks for different methods to fix the relative phase between the different energies. One can make the phase of a particular wave constant with energy, but trying to guess which wave is difficult. (with hindsight, we could fix the phase of the RH3 DS33 wave in our case.) One can assume that one wave is resonating and give that wave the appropriate phase at each energy. Still another method is the least path method. Here one adjusts the relative phase between the amplitudes at energy E_n and energy E_{n+1} so as to minimize the quantity $\sum_j |T_j(E_n) - T_j(E_{n+1})|$. This was the method used by Miller.[4] When most of the waves are moving with energy, this method tends to remove the motion. A more sophisticated method,

and therefore more open to discussion, is to try and relate the inelastic phases to the elastic phases using the K-matrix formalism. Longacre's program fits each incoming partial wave with a factorizable pole and a constant non-factorizable background. He adjusts the overall phase at each energy to give the best combined fit to the four partial waves D15, F15, F35, and F37. Figures 24 - 28 are our final amplitudes with this phase adjustment. The errors are approximately the size of the letter representing each point and have been surpressed for legibility. Tables III - XI give our final 24 amplitudes and the parameters of the two-dimensional error ellipse[16] at each energy. The appendix in LBL-544 will be a more detailed discussion of the errors.

There are two general features of our amplitudes. The Delta in general is coupled to the resonances in the lower part of our energy region and the Rho is coupled to those resonances in the upper part of our energy region and to those resonances just above our energy region. This probably reflects the opening of the Rho channel at a CM energy of 1700 MeV.

Figures 29 - 40 give our amplitudes rearranged by incoming partial wave. In each figure we give the Argand plot and $|T|^2$ plot for each of our amplitudes along with a plot of the calculated inelastic cross-section, σ_{calc}. On the cross-section plots, we show the predicted inelastic cross-sections, σ_{inel} and $\delta\sigma_{inel}$, as vertical lines slightly offset. For the following discussion we use the new

πN phase-shift analysis of Almehed and Lovelace[17] as the "elastic analysis." Table XII is a copy of their Table 3 with an extra column added showing which diparticle couples to each resonance.

S11 We clearly see the elastic S11(1670) in the σN channel; in the ρN channel the S11(1670) seems to be there but not strongly. The ρN channel also gives evidence for a resonance above our energy region corresponding to the S11(2100).

P11 The P11(1720) seems to be mostly Δπ whereas the σN channel suggests a new resonance at about 2100 MeV.

P13 We definitely have a resonance at about 1900 in the ρN channel with a width of ≈300 MeV.

D13 Both the Δπ(DS13) and the σN channels suggest that the D13(1700), badly needed by the quark model,[18] does exist. Point H in the RH3 DS13 wave is probably a bad point and should be out with G and I. In which case, this channel is coupled to the D13(2075).

D15 As we should, we see the D15(1683) but only in the Δπ channel. We see no evidence for the D15(2100); probably because we have not included the ρN channel in the final fit.

F15 The F15(1688) appears in all three channels and about equally in each. No indication of the F15(2175) but it is probably too far above our energies.

F17 We found that the F17 waves were insignificant at our energies.

S31 Both the $\Delta\pi$ and ρN channels indicate the presence of the S31(1620) just below our energy region.

P31 We see nothing in the P31 channel.

P33 The $\Delta\pi$ amplitude is consistent with just a decreasing background.

D33 We see the D33(1700) in the $\Delta\pi$ channel with no structure in the ρN channel.

D35 We found the D35 channels insignificant.

F35 The F35(1875) is clearly shown by the ρN channel. No apparent structure in the $\Delta\pi$ channel.

F37 The F37(1925) is clearly seen in both the $\Delta\pi$ and ρN channels.

In looking at the large $\Delta\pi$ F15 and D15 channels, we find that solution B of our earlier paper[19] can be discarded. We find that the relative sign of the couplings of these resonances to the $\Delta\pi$ channel is negative, and that the F15 is coupled about equally to the $\Delta\pi$, ρN, and σN channels.

* * * * * * * * *

We have presented the results of an energy independent partial wave analysis of the single-pion production reactions at nine energies. Using the results of a K-matrix analysis, we have removed the arbitrary overall phase at each energy. The Argand plots confirm the two resonances S11(2100) and P13(1850) observed only weakly in the elastic channel. We also see evidence for a new resonance around 2100 VeV in P11, and no evidence for the P31(1900). We also see some evidence for the D13(1700). Furthur study[6] is planned of each incoming partial wave using the K-matrix to give the proportion of background to resonance and the resonance parameters.

ACKNOWLEDGMENTS

First and foremost I wish to thank my wife. Her loving support and encouragement made even the drudgery seem worthwhile.

I wish to thank my advisor, Art Rosenfeld, for his guidance and patient understanding. I also want to thank all the physicists with whom I worked and who were always ready to answer all my questions: LeRoy Price, Roger Cashmore, Paul Söding, Ben Shen, Gerard Smadja, Bernard Deler, Tony Brody, and David Leith.

My thanks to my fellow graduate students on this experiment, Larry Miller and Ron Longacre. Ron gets special thanks because he was always ready to do the tasks that I did not want to do.

I also want to thank the LBL computer operations staff. They were always helpful and gave me much special attention without which I would never have finished.

Finally I want to thank the other members of my thesis committee, William Chinowsky and Loren Meissner, for their helpful suggestions and criticisms.

TABLE I: Events per channel for each energy bin

Energy Range	Bin Name	Mark 2 Events (n-+)	Mark 3 Events (p-0)	Mark 4 Events (p+0)	Total Events
1630 - 1670	1650	6061	3757	2467	12285
1670 - 1710	1690	5901	3689	1139	10729
1710 - 1750	1730	3455	2630	4061	10146
1750 - 1790	1770	3214	2352	2853	8419
1790 - 1830	1810	2447	1541	3855	7843
1830 - 1870	1850	3931	3183	6372	13486
1870 - 1910	1890	5072	3170	12690	20932
1910 - 1950	1930	5817	4080	4298	14195
1950 - 1990	1970	5277	3544	7744	16565

TABLE II: Input and calculated cross-sections for each channel

ENERGY	MARK 1 (n00)		MARK 2 (n-+)		MARK 3 (p-0)		MARK 4 (p+0)		MARK 5 (n++)	
Bin	INPUT	CALC	INPUT	CALC	INPUT	CALC	INPUT	CALC	INPUT	CALC
1650	3.54		10.10	10.40	6.21	5.81	9.90	10.00	0.93	
1690	3.96		11.81	12.21	7.29	6.86	10.10	10.13	1.01	
1730	2.57		8.07	8.37	5.93	5.68	9.70	9.66	0.91	
1770	2.14		7.75	8.00	5.68	5.40	10.20	10.22	0.72	
1810	2.13		8.30	8.42	4.79	4.75	10.90	10.82	0.74	
1850	1.86		8.00	7.99	4.50	4.50	11.50	11.52	0.74	
1890	1.81		8.70	8.51	4.90	4.86	11.20	11.43	0.76	
1930	1.68		7.50	7.40	4.80	4.75	11.50	11.65	0.67	
1970	1.29		6.60	6.44	4.50	4.36	8.60	8.91	0.49	

TABLE III: 1650 Partial-wave amplitudes with error ellipse parameters (semi-major axis, semi-minor axis, and angle of semi-major axis wrt the x-axis.)

WAVE LABEL	AMPLITUDE REAL	AMPLITUDE IMAG	ERROR ELLIPSE MAJOR	ERROR ELLIPSE MINOR	ERROR ELLIPSE ANGLE(°)
P33 PP11	-0.288	0.063	0.037	0.037	-41.28
P33 DS13	0.225	-0.054	0.032	0.029	55.31
P33 DD13	-0.083	-0.103	0.028	0.024	43.40
P33 FP15	-0.035	0.266	0.025	0.020	- 0.85
P33 DD15	-0.200	-0.346	0.024	0.018	43.53
P33 PP31	0.084	-0.061	0.035	0.030	75.07
P33 SD31	0.123	-0.338	0.038	0.023	5.02
P33 DS33	0.177	0.168	0.029	0.023	-59.67
P33 PP33	0.086	0.306	0.041	0.012	55.85
P33 FF35					
P33 FF37					
RH3 DS13	0.033	-0.070	0.026	0.022	-80.63
RH3 FP15	0.132	0.234	0.018	0.016	41.19
RH3 DS33	0.192	0.007	0.025	0.024	74.20
RH3 FP35					
RH3 FF37					
RH1 SS11	0.171	0.074	0.035	0.028	-86.15
RH1 PP13	-0.073	0.040	0.024	0.021	-61.18
RH1 SS31	0.222	0.207	0.041	0.025	-69.73
RH1 PP31	0.087	-0.027	0.037	0.037	-54.88
SIG PS11	0.153	0.022	0.043	0.035	-67.75
SIG SP11	-0.178	-0.133	0.047	0.040	-58.69
SIG DP13	-0.214	-0.041	0.034	0.026	-71.04
SIG FD15	0.131	0.202	0.018	0.014	-42.71

TABLE IV: 1690 Partial-wave amplitudes with error ellipse parameters (semi-major axis, semi-minor axis, and angle of semi-major axis wrt the x-axis.)

WAVE LABEL	AMPLITUDE REAL	AMPLITUDE IMAG	ERROR ELLIPSE MAJOR	ERROR ELLIPSE MINOR	ERROR ELLIPSE ANGLE(°)
P33 PP11	-0.248	-0.145	0.044	0.042	-39.20
P33 DS13	0.254	0.105	0.032	0.031	-56.26
P33 DD13	0.011	-0.080	0.032	0.027	-33.87
P33 FP15	-0.214	0.256	0.026	0.023	-74.10
P33 DD15	-0.033	-0.447	0.033	0.018	-37.25
P33 PP31	0.094	0.051	0.051	0.037	82.08
P33 SD31	0.281	-0.213	0.041	0.037	-75.08
P33 DS33	0.014	0.268	0.033	0.028	-31.74
P33 PP33	-0.138	0.337	0.039	0.017	76.08
P33 FF35					
P33 FF37					
RH3 DS13	-0.035	-0.040	0.032	0.024	-43.50
RH3 FP15	-0.069	0.306	0.023	0.018	69.54
RH3 DS33	0.137	0.071	0.031	0.029	-51.53
RH3 FP35					
RH3 FF37					
RH1 SS11	0.196	0.207	0.038	0.032	-66.11
RH1 PP13	-0.160	-0.059	0.027	0.026	-35.27
RH1 SS31	0.073	0.303	0.054	0.034	-45.73
RH1 PP31	0.036	-0.038	0.050	0.044	73.20
SIG PS11	0.077	0.163	0.050	0.043	-38.76
SIG SP11	0.016	-0.266	0.042	0.041	-27.49
SIG DP13	-0.233	-0.163	0.030	0.029	-69.67
SIG FD15	-0.025	0.250	0.018	0.018	61.25

TABLE V: 1730 Partial-wave amplitudes with error ellipse parameters (semi-major axis, semi-minor axis, and angle of semi-major axis wrt the x-axis.)

WAVE LABEL	AMPLITUDE REAL	AMPLITUDE IMAG	ERROR ELLIPSE MAJOR	ERROR ELLIPSE MINOR	ERROR ELLIPSE ANGLE(°)
P33 PP11	-0.098	-0.329	0.048	0.048	68.91
P33 DS13	0.089	0.163	0.040	0.029	- 2.41
P33 DD13	0.052	-0.037	0.041	0.028	5.76
P33 FP15	-0.263	0.152	0.035	0.023	-46.10
P33 DD15	0.206	-0.193	0.036	0.023	10.88
P33 PP31	0.077	-0.030	0.035	0.034	-65.24
P33 SD31	0.252	-0.122	0.042	0.032	-51.97
P33 DS33	-0.077	0.216	0.032	0.022	- 7.32
P33 PP33	-0.058	0.338	0.021	0.015	-14.93
P33 FF35	0.004	0.120	0.026	0.019	1.11
P33 FF37	0.087	0.088	0.015	0.013	28.07
RH3 DS13	0.003	0.054	0.030	0.029	23.00
RH3 FP15	-0.243	0.106	0.033	0.018	-46.51
RH3 DS33	0.168	0.103	0.028	0.020	-82.98
RH3 FP35	-0.167	-0.014	0.020	0.016	-29.29
RH3 FF37					
RH1 SS11	-0.049	0.238	0.051	0.040	1.36
RH1 PP13	-0.063	-0.214	0.034	0.031	-28.71
RH1 SS31	-0.004	0.124	0.034	0.033	84.07
RH1 PP31	0.049	0.147	0.037	0.035	82.09
SIG PS11	0.063	0.177	0.058	0.049	9.02
SIG SP11	0.169	-0.221	0.059	0.053	17.22
SIG DP13	-0.148	-0.179	0.034	0.031	34.39
SIG FD15	-0.177	0.194	0.022	0.019	-74.91

TABLE VI: 1770 Partial-wave amplitudes with error ellipse parameters (semi-major axis, semi-minor axis, and angle of semi-major axis wrt the x-axis.)

WAVE LABEL	AMPLITUDE REAL	AMPLITUDE IMAG	ERROR ELLIPSE MAJOR	ERROR ELLIPSE MINOR	ERROR ELLIPSE ANGLE(°
P33 PP11	0.156	-0.296	0.055	0.040	35.08
P33 DS13	0.083	0.210	0.038	0.036	-89.13
P33 DD13	0.105	-0.010	0.038	0.037	9.76
P33 FP15	-0.294	-0.005	0.029	0.026	-79.01
P33 DD15	0.067	-0.116	0.032	0.027	89.52
P33 PP31	0.113	0.029	0.042	0.040	12.78
P33 SD31	0.263	-0.095	0.044	0.030	- 7.41
P33 DS33	-0.028	0.114	0.031	0.029	-57.76
P33 PP33	0.089	0.300	0.044	0.016	74.29
P33 FF35	-0.033	0.083	0.027	0.024	17.24
P33 FF37	0.055	0.161	0.029	0.016	75.93
RH3 DS13	-0.104	-0.008	0.033	0.030	-24.47
RH3 FP15	-0.212	0.037	0.029	0.023	- 4.07
RH3 DS33	0.250	0.039	0.032	0.023	-71.41
RH3 FP35	-0.228	-0.108	0.026	0.013	-68.20
RH3 FF37	-0.031	0.037	0.022	0.016	-68.71
RH1 SS11	-0.020	0.311	0.045	0.042	-84.60
RH1 PP13	-0.013	-0.359	0.040	0.030	76.72
RH1 SS31	0.009	0.150	0.040	0.037	58.86
RH1 PP31	0.033	0.120	0.048	0.040	-69.82
SIG PS11	0.032	0.307	0.051	0.047	-87.22
SIG SP11	0.238	-0.147	0.061	0.041	-19.78
SIG DO13	-0.081	-0.241	0.036	0.031	79.17
SIG FD15	-0.178	0.086	0.027	0.025	77.04

TABLE VII: 1810 Partial-wave amplitudes with error ellipse parameters (semi-major axis, semi-minor axis, and angle of semi-major axis wrt the x-axis.)

WAVE LABEL	AMPLITUDE REAL	AMPLITUDE IMAG	ERROR ELLIPSE MAJOR	ERROR ELLIPSE MINOR	ERROR ELLIPSE ANGLE(°)
P33 PP11	0.119	-0.292	0.066	0.049	-73.52
P33 DS13	0.041	0.160	0.044	0.040	-86.23
P33 DD13	0.018	-0.195	0.042	0.040	80.74
P33 FP15	-0.242	-0.003	0.036	0.033	- 1.82
P33 DD15	0.143	0.026	0.035	0.033	-17.57
P33 PP31	0.079	0.059	0.043	0.037	-82.92
P33 SD31	0.218	-0.034	0.035	0.034	- 0.08
P33 DS33	-0.088	0.079	0.029	0.027	-87.59
P33 PP33	-0.036	0.285	0.017	0.011	84.73
P33 FF35	0.053	0.102	0.026	0.023	-22.10
P33 FF37	0.070	0.218	0.025	0.011	-27.50
RH3 DS13	-0.178	-0.049	0.038	0.035	56.88
RH3 FP15	-0.137	0.090	0.032	0.026	49.00
RH3 DS33	0.224	0.072	0.034	0.020	15.32
RH3 FP35	-0.185	-0.206	0.021	0.019	-54.75
RH3 FF37	-0.074	0.043	0.018	0.016	- 8.07
RH1 SS11	-0.091	0.224	0.067	0.045	-78.10
RH1 PP13	0.112	-0.411	0.039	0.021	-89.45
RH1 SS31	-0.058	0.169	0.038	0.038	77.93
RH1 PP31	0.083	0.096	0.045	0.043	30.87
SIG PS11	-0.058	0.342	0.064	0.054	85.54
SIG SP11	0.294	-0.035	0.071	0.071	32.44
SIG DP13	-0.021	-0.236	0.042	0.041	78.82
SIG FD15	-0.238	0.096	0.037	0.028	-27.23

TABLE VIII: 1850 Partial-wave amplitudes with error ellipse parameters (semi-major axis, semi-minor axis, and angle of semi-major axis wrt the x-axis.)

WAVE LABEL	AMPLITUDE REAL	AMPLITUDE IMAG	ERROR ELLIPSE MAJOR	ERROR ELLIPSE MINOR	ERROR ELLIPSE ANGLE(°)
P33 PP11	0.154	-0.291	0.046	0.037	67.33
P33 DS13	-0.022	0.210	0.032	0.030	77.72
P33 DD13	0.079	-0.045	0.037	0.032	60.50
P33 FP15	-0.231	-0.067	0.028	0.024	-37.63
P33 DD15	-0.037	0.020	0.026	0.026	-52.01
P33 PP31	0.104	0.172	0.031	0.030	47.94
P33 SD31	0.247	0.064	0.031	0.021	-37.79
P33 DS33	-0.080	0.085	0.020	0.020	46.53
P33 PP33	0.010	0.242	0.024	0.024	-51.32
P33 FF35	-0.008	0.127	0.023	0.017	56.30
P33 FF37	-0.073	0.230	0.022	0.013	52.09
RH3 DS13	-0.143	-0.094	0.029	0.025	9.52
RH3 FP15	-0.136	0.040	0.022	0.020	26.46
RH3 DS33	0.240	0.033	0.021	0.017	-39.34
RH3 FP35	-0.143	-0.289	0.020	0.012	-82.47
RH3 FF37	-0.131	0.063	0.013	0.012	24.15
RH1 SS11	-0.182	0.229	0.043	0.029	72.12
RH1 PP13	0.289	-0.329	0.013	0.006	74.42
RH1 SS31	-0.044	0.043	0.035	0.030	-79.57
RH1 PP31	0.013	-0.022	0.037	0.032	-78.11
SIG PS11	-0.215	0.272	0.050	0.038	65.47
SIG SP11	0.282	-0.041	0.049	0.045	33.56
SIG DP13	0.092	-0.291	0.036	0.028	56.62
SIG FD15	-0.210	0.048	0.027	0.026	-55.18

TABLE IX: 1890 Partial-wave amplitudes with error ellipse parameters (semi-major axis, semi-minor axis, and angle of semi-major axis wrt the x-axis.)

WAVE	AMPLITUDE		ERROR ELLIPSE		
LABEL	REAL	IMAG	MAJOR	MINOR	ANGLE(°)
P33 PP11	0.130	-0.350	0.044	0.033	-57.58
P33 DS13	-0.089	0.096	0.031	0.028	52.02
P33 DD13	0.123	-0.063	0.036	0.031	69.32
P33 FP15	-0.223	0.006	0.024	0.023	85.49
P33 DD15	-0.162	-0.066	0.026	0.025	53.70
P33 PP31	0.116	0.185	0.026	0.026	1.40
P33 SD31	0.230	0.124	0.027	0.020	30.23
P33 DS33	-0.118	0.077	0.017	0.015	56.16
P33 PP33	-0.066	0.150	0.018	0.017	-46.77
P33 FF35	-0.001	0.180	0.018	0.016	50.64
P33 FF37	-0.193	0.173	0.014	0.012	47.37
RH3 DS13	-0.167	-0.212	0.025	0.025	6.01
RH3 FP15	-0.087	0.112	0.024	0.018	59.66
RH3 DS33	0.210	0.057	0.017	0.013	26.79
RH3 FP35	-0.064	-0.299	0.015	0.013	- 6.43
RH3 FF37	-0.195	0.040	0.010	0.010	86.20
RH1 SS11	-0.270	0.241	0.041	0.025	55.91
RH1 PP13	0.411	-0.240	0.033	0.014	61.18
RH1 SS31	-0.072	0.045	0.026	0.025	- 4.66
RH1 PP31	-0.024	-0.068	0.028	0.027	-82.71
SIG PS11	-0.199	0.258	0.042	0.037	-53.12
SIG SP11	0.222	0.010	0.046	0.042	85.82
SIG DP13	0.142	-0.213	0.033	0.029	51.49
SIG FD15	-0.286	0.031	0.021	0.020	-50.53

TABLE X: 1930 Partial-wave amplitudes with error ellipse parameters (semi-major axis, semi-minor axis, and angle of semi-major axis wrt the x-axis.)

WAVE	AMPLITUDE		ERROR ELLIPSE		
LABEL	REAL	IMAG	MAJOR	MINOR	ANGLE(°)
P33 PP11	0.236	-0.098	0.047	0.036	-77.48
P33 DS13	-0.133	0.227	0.028	0.027	80.78
P33 DD13	0.077	-0.168	0.030	0.030	80.23
P33 FP15	-0.171	-0.084	0.026	0.022	59.43
P33 DD15	-0.094	-0.019	0.027	0.022	88.13
P33 PP31	0.059	-0.006	0.033	0.033	-60.46
P33 SD31	0.197	0.265	0.029	0.025	- 6.35
P33 DS33	-0.076	-0.102	0.023	0.022	2.19
P33 PP33	-0.061	0.044	0.030	0.021	-88.89
P33 FF35	-0.076	0.153	0.023	0.021	85.33
P33 FF37	-0.241	0.139	0.025	0.014	-84.75
RH3 DS13	-0.033	-0.056	0.031	0.022	-74.11
RH3 FP15	-0.150	-0.007	0.020	0.019	-57.34
RH3 DS33	0.226	0.151	0.022	0.020	74.62
RH3 FP35	-0.033	-0.314	0.018	0.015	27.93
RH3 FF37	-0.207	-0.094	0.017	0.013	65.13
RH1 SS11	-0.281	0.253	0.042	0.029	-86.43
RH1 PP13	0.437	-0.200	0.035	0.013	-81.04
RH1 SS31	0.165	0.002	0.038	0.035	69.89
RH1 PP31	0.101	-0.033	0.039	0.038	14.08
SIG PS11	-0.396	0.037	0.043	0.030	-66.80
SIG SP11	0.295	0.064	0.043	0.038	48.93
SIG DP13	0.162	-0.220	0.029	0.027	84.64
SIG FD15	-0.225	0.046	0.025	0.024	-89.14

TABLE XI: 1970 Partial-wave amplitudes with error ellipse parameters (semi-major axis, semi-minor axis, and angle of semi-major axis wrt the x-axis.)

WAVE	AMPLITUDE		ERROR ELLIPSE		
LABEL	REAL	IMAG	MAJOR	MINOR	ANGLE(°)
P33 PP11	0.160	-0.260	0.042	0.030	-46.79
P33 DS13	-0.126	-0.062	0.030	0.028	-85.96
P33 DD13	0.097	0.097	0.034	0.030	55.62
P33 FP15	-0.181	-0.039	0.024	0.020	35.71
P33 DD15	-0.098	-0.098	0.027	0.026	29.86
P33 PP31	-0.033	0.110	0.028	0.026	30.12
P33 SD31	0.211	0.214	0.025	0.019	60.88
P33 DS33	-0.115	-0.080	0.020	0.016	43.73
P33 PP33	0.012	-0.035	0.026	0.015	-89.20
P33 FF35	-0.107	0.150	0.019	0.016	78.64
P33 FF37	-0.211	0.018	0.018	0.012	-79.83
RH3 DS13	0.041	-0.293	0.022	0.022	-66.04
RH3 FP15	-0.089	0.029	0.021	0.018	-76.57
RH3 DS33	0.146	0.177	0.016	0.015	65.81
RH3 FP35	0.069	-0.263	0.015	0.012	-58.78
RH3 FF37	-0.199	-0.121	0.015	0.009	48.92
RH1 SS11	-0.415	-0.016	0.038	0.025	-78.19
RH1 PP13	0.467	0.035	0.017	0.013	-72.40
RH1 SS31	-0.087	0.047	0.028	0.027	-58.52
RH1 PP31	0.088	-0.112	0.032	0.030	- 9.06
SIG PS11	-0.342	0.141	0.038	0.027	78.39
SIG SP11	0.169	-0.108	0.047	0.037	-81.45
SIG DP13	0.183	0.040	0.036	0.025	87.69
SIG FD15	-0.262	0.040	0.022	0.016	80.62

TABLE XII This is Table 3 of Almehed and Lovelace[17] with the addition of an extra column giving our channel to which the resonance couples.*

Approximate resonance parameters(MeV)

Wave	Mass	Γ_{tot}	Γ_{el}/Γ_{tot}	Grade	Inel. Wave
S31	1620	140	0.35	A	Δ ρ
P31	1900	200	0.33	B	
P33(i)	1235	129	1.0	A	
P33(ii)	1680	220	0.1	D	
P33(iii)	2150	200	0.3	C	
D33	1700	260	0.16	A	Δ
D35	?2200	?600	?0.25	D	
F35	1875	250	0.18	A	ρ
F37	1925	200	0.4	A	Δ ρ
S11(i)	1500	50	0.25	A	
S11(ii)	1670	120	0.5	A	ρ σ
S11(iii)	2100	200	0.5	D	ρ
P11(i)	1470	220	0.65	A	
P11(ii)	≈1720	≈160	0.2	A	Δ
P13	≈1850	≈300	≈0.25	C	ρ
D13(i)	1520	120	0.58	A	< Δ σ
< (1700)					
D13(ii)	2075	150	0.3	B	ρ
D15(i)	1683	150	0.45	A	Δ
D15(ii)	2100	150	0.2	C	
F15(i)	1688	140	0.65	A	Δ ρ σ
F15(ii)	≈2175	≈150	≈0.25	D	
F17	2000	200	0.15	C	
G17	≈2225	≈150	≈0.35	C	

*We have inserted the D13(1700) which is not seen in the elastic channels.

REFERENCES AND FOOTNOTES

1. A. D. Brody, R. J. Cashmore, A. Kernan, D. W. G. S. Leith, B. G. Levi, A. Minten, B. C. Shen, J. P. Berge, B. Deler, D. J. Herndon, R. Longacre, L. R. Miller, A. H. Rosenfeld, and P. Söding, PHYSICAL REVIEW D4, 2963 (1971)

2. Philippe Chavanon, thesis, College de France, 1971

3. S. Y. Fung, A. Kernan, U. Mehtani, T. L. Schalk, Y. Williamson, W. Michael, R. W. Birge, G. E. Kalmus.

4. Larry R. Miller, LBL - 38 (Ph.D. Thesis)

5. David J. Herndon, Paul Söding, Roger J. Cashmore, LBL - 543

6. Ronald Longacre, LBL - 938 (Ph.D. Thesis)

7. F. von Hippel and C. Quigg, PHYSICAL REVIEW D5, 624 (1972)

8. David J. Herndon, Angela Barbaro-Galtieri, Arthur H. Rosenfeld, UCRL - 20030πN

9. David Morgan, PHYSICAL REVIEW D2, 520 (1970)

10. S. D. Protopopescu, M. Alston-Garnjost, A. Barbaro-Galtieri, S. M. Flatté, J. H. Friedman, T. A. Lasinski, G. R. Lynch, M. S. Rabin, and F. T. Solmitz, LBL - 787

11. B. Deler and G. Valladas, NUOVO CIMENTO 45A, 1309 (1966)

12. D. H. Saxon, J. H. Mulvey, W. Chinowsky, PHYSICAL REVIEW D2, 1790 (1970)

13. M. G. Bowler and R. J. Cashmore, NUCLEAR PHYSICS B17, 331 (1970)

14. E. Flaminio, J. D. Hansen, D. R. O. Morrison, N. Tovey, Compilation of Cross-sections IV π^+ induced reactions, CERN/HERA 70-5 and Compilation of Cross-sections VI π^- induced reactions, CERN/HERA 70-7

15. Rawmeat, Group A Programming Note #P-214

16. In reference 4, Miller discusses the two-dimensional error ellipse for the real and imaginary part of each amplitude. In the tables we give the length of the semi-major axis and semi-minor axis and the angle θ the major axis makes with the x-axis, $-90° < \theta < 90°$.

17. S. Almehed and C. Lovelace, NUCLEAR PHYSICS B40, 157 (1972)

18. R. Dalitz, in Pion-nucleon Scattering, ed. Shaw and Wong (Wiley, New York, 1969)
O. Greenberg, Proceedings of the Lund Conference, 1969
R. Feynman et. al. PHYSICAL REVIEW D2, 1267 (1970)

19. A. D. Brody, R. J. Cashmore, A. Kernan, D. W. G. S. Leith, D. J. Herndon, L. R. Price, A. H. Rosenfeld, P. Söding, PHYSICS LETTERS 34B, 665 (1971)

20. Ron Longacre and Gerard Smadja are working on fits to a collection of the low energy data. Reference 6 and this paper will cover the energy region from threshold to 1.53 GeV.

FIGURE CAPTIONS

1. 72" HBC $\pi^- p \to N \pi \pi$ events per 10 MeV, arrows indicate the energies 1690-70 and 1690+70 (half-widths above and below 1690.) Total of 28111 events.

2. 30" HBC $\pi^- p \to N \pi \pi$ events per 10 MeV. Total of 59510 events.

3. Total $\pi^- p \to n \pi^- \pi^+$ events per 10 MeV. Total of 41210 events.

4. Total $\pi^- p \to p \pi^- \pi^0$ events per 10 MeV. Total of 27306 events.

5. Total $\pi^+ p \to p \pi^+ \pi^0$ events per 10 MeV. Total of 45474 events.

6. All events per 10 MeV. Total of 113990 events

7. Summary of kinematic quantities for the general Isobar Model.

8. Final-state factor for the Delta.

9. Final-state factor for the Rho.

10. Final-state factor for the Sigma. Dashed line on 6 plot from reference 10.

11. Generating amplitudes for the artificial data.

12. Final fitted amplitudes from the artificial data. 12a contains the amplitudes corresponding to the generating set, 12b contains the extra thirteen waves. The box about the origin in figure 12a shows the relative size of figure 12b.

13. Mark 1 cross-sections - experimental values from ref. 14

14. Mark 2 cross-sections - experimental values from ref. 1

15. Mark 3 cross-sections - experimental values from ref. 1

16. Mark 4 cross-sections - experimental values from ref. 14

17. Mark 5 cross-sections - experimental values from ref. 14

18. Comparison of data to prediction for Mark 2 events at 1690

19. Comparison of data to prediction for Mark 3 events at 1690

20. Comparison of data to prediction for Mark 4 events at 1690

21. Comparison of data to prediction for Mark 2 events at 1930

22. Comparison of data to prediction for Mark 3 events at 1930

23. Comparison of data to prediction for Mark 4 events at 1930

All Argand plots have the wave label in the lower left and the scale maximum in the lower right. The number after the energy in the legend is the identification number for that set of waves. These plots also appear in figures 29 - 40 but in a different order.

24. Argand plots for Delta waves with incoming Ispin = 1/2

25. Argand plots for Delta waves with incoming Ispin = 3/2

26. Argand plots for Rho waves with $S_j = 3/2$

27. Argand plots for Rho waves with $S_j = 1/2$

28. Argand plots for Sigma waves.

29. Argnad plots, $|T|^2$ plots and cross-section plot for S11

30. Argand plots, $|T|^2$ plots and cross-section plot for P11

31. Argand plots, $|T|^2$ plots and cross-section plot for P13

32. Argand plots, $|T|^2$ plots and cross-section plot for D13

33. Argand plots, $|T|^2$ plots and cross-section plot for D15

34. Argand plots, $|T|^2$ plots and cross-section plot for F15

35. Argand plots, $|T|^2$ plots and cross-section plot for S31

36. Argand plots, $|T|^2$ plots and cross-section plot for P31

37. Argand plots, $|T|^2$ plots and cross-section plot for P33

38. Argand plots, $|T|^2$ plots and cross-section plot for D33

39. Argand plots, $|T|^2$ plots and cross-section plot for F35

40. Argand plots, $|T|^2$ plots and cross-section plot for F37

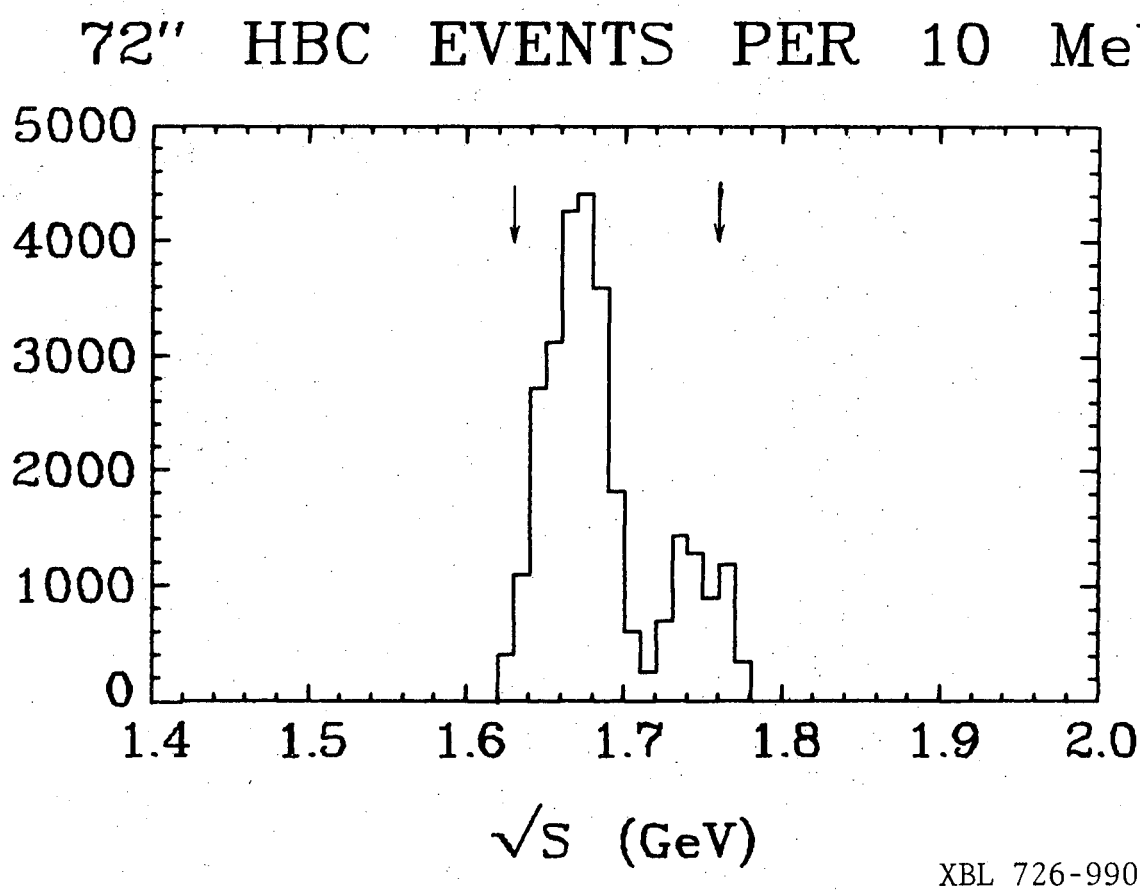

XBL 726-990

Fig. 1.

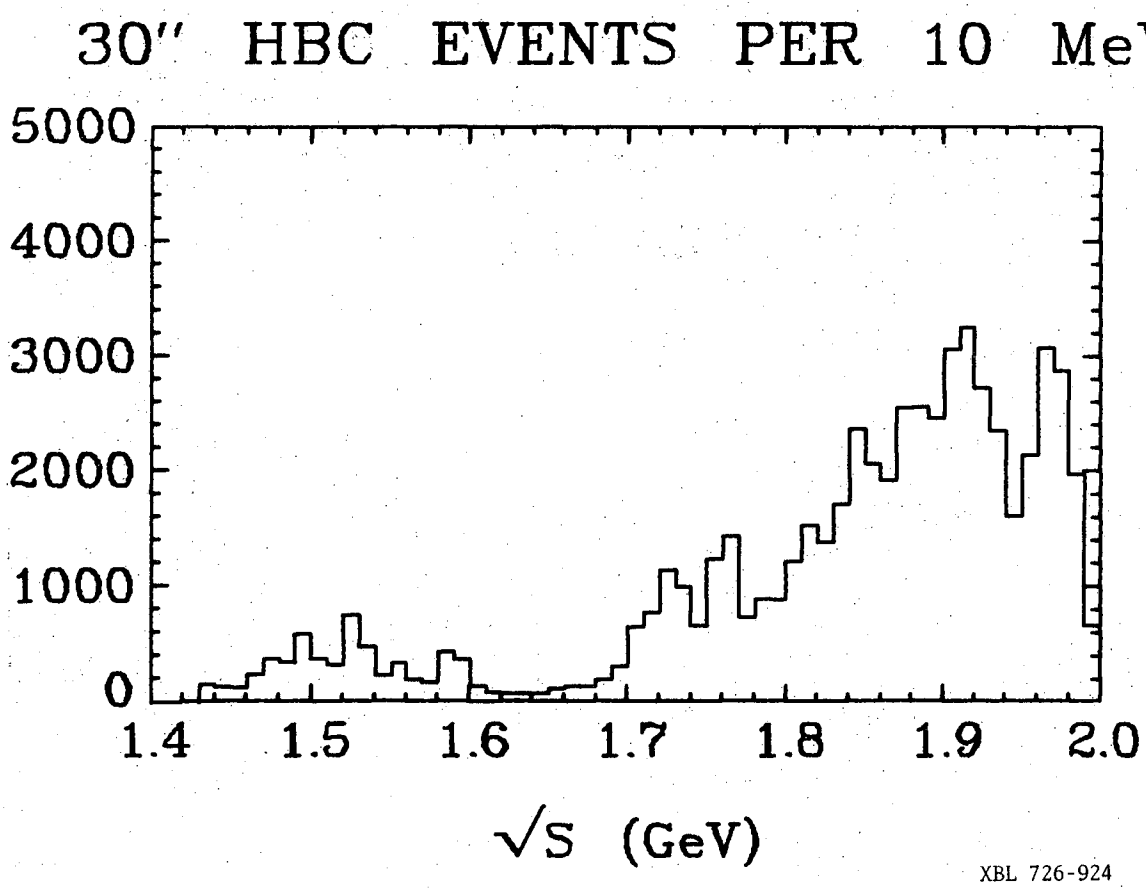
30" HBC EVENTS PER 10 MeV
5000
4000
3000
2000
1000
0
1.4
1.5
1.6
1.7
1.8
1.9
2.0
√S (GeV)
XBL 726-924

Fig. 2.

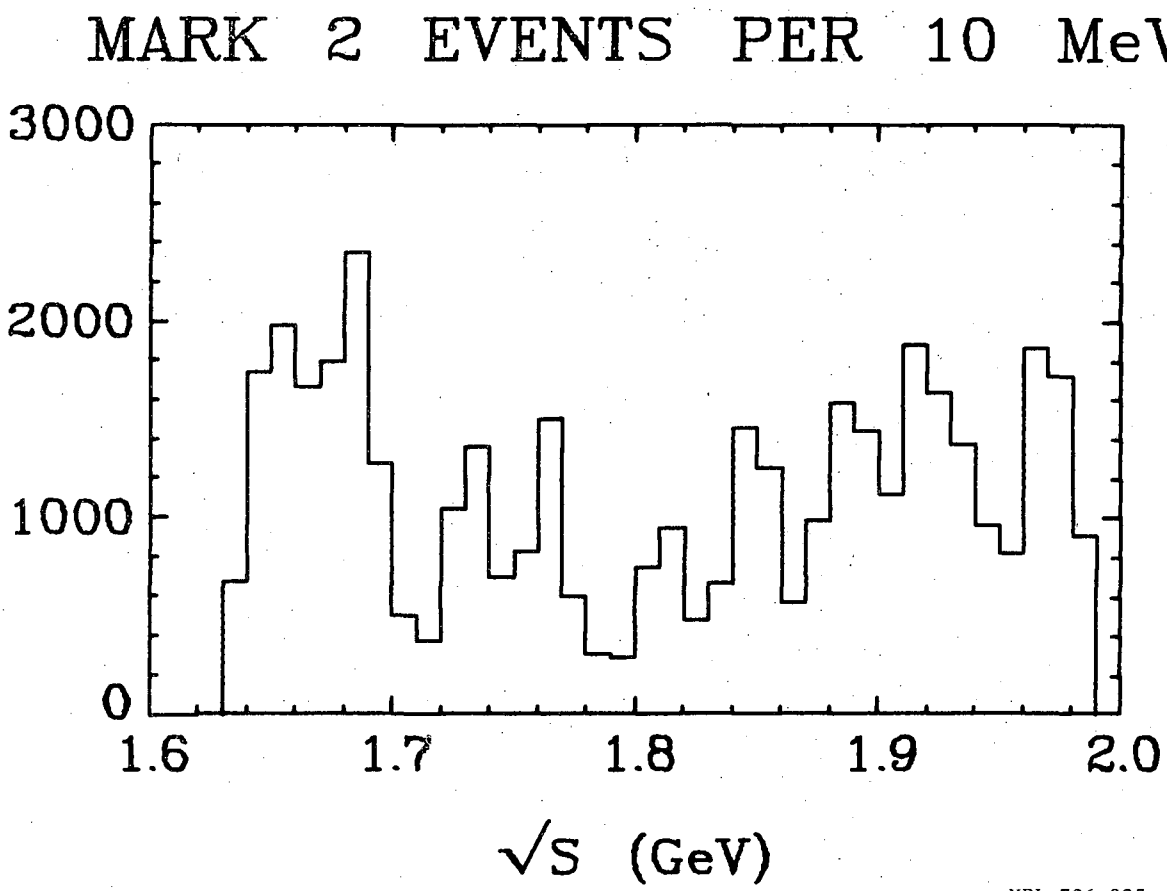

XBL 726-925

Fig. 3.

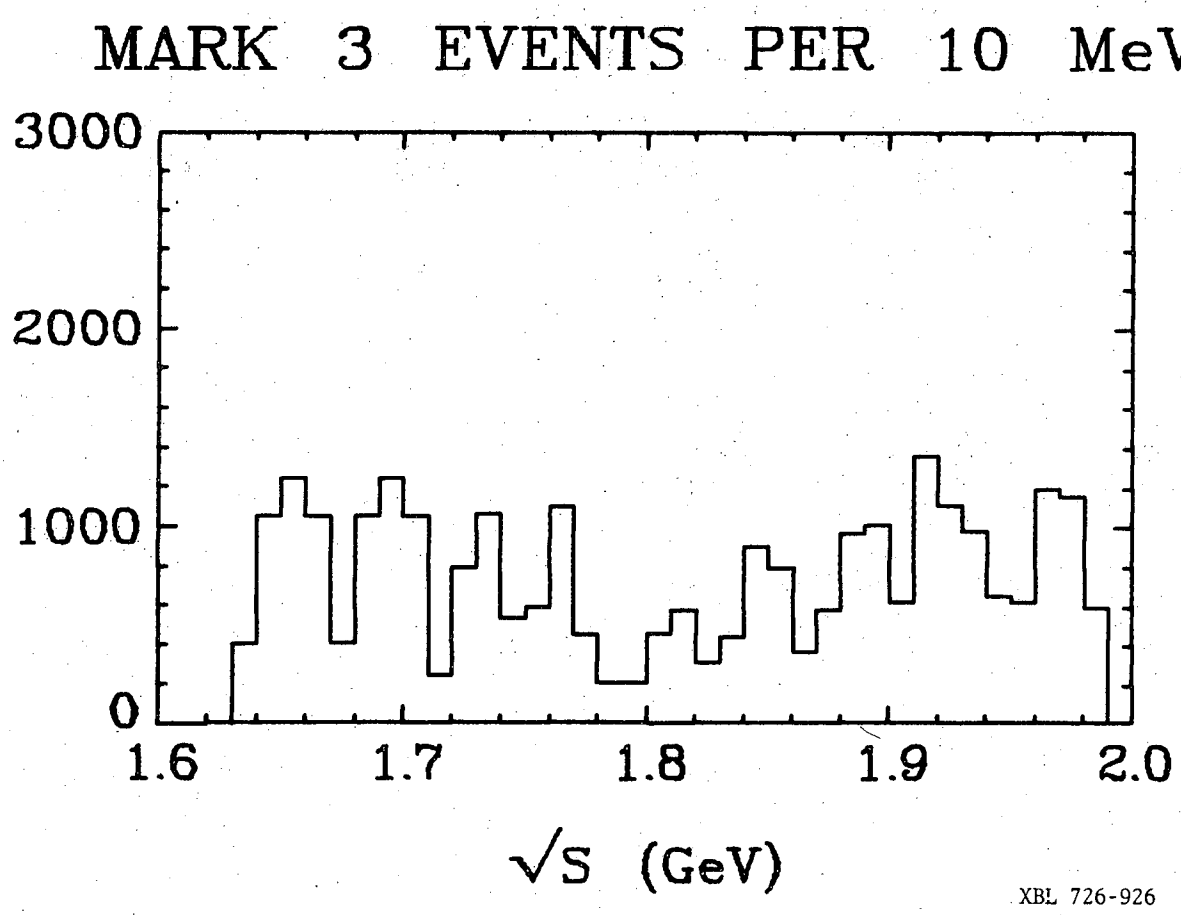
MARK 3 EVENTS PER 10 MeV
3000
2000
1000
0
1.6
1.7
1.8
1.9
2.0
√S (GeV)
XBL 726-926

Fig. 4.

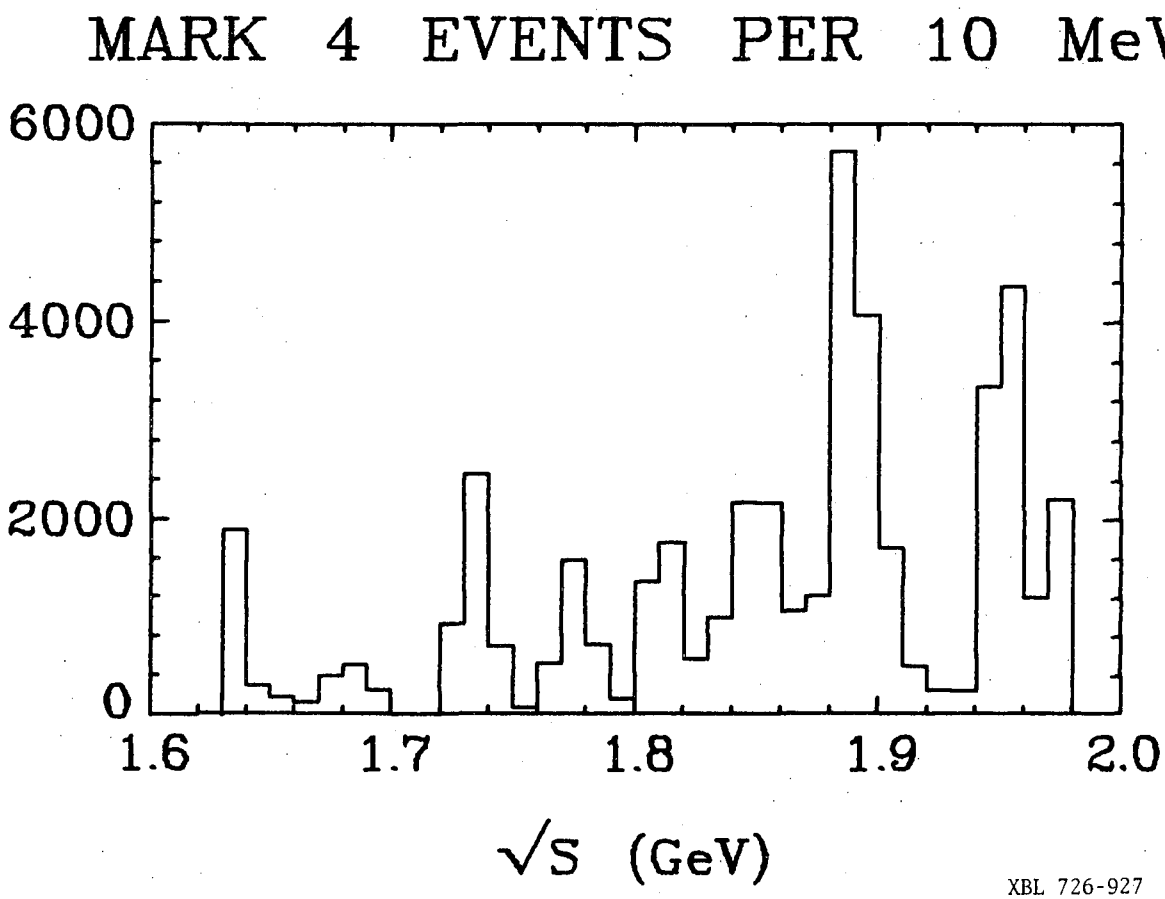

Fig. 5.

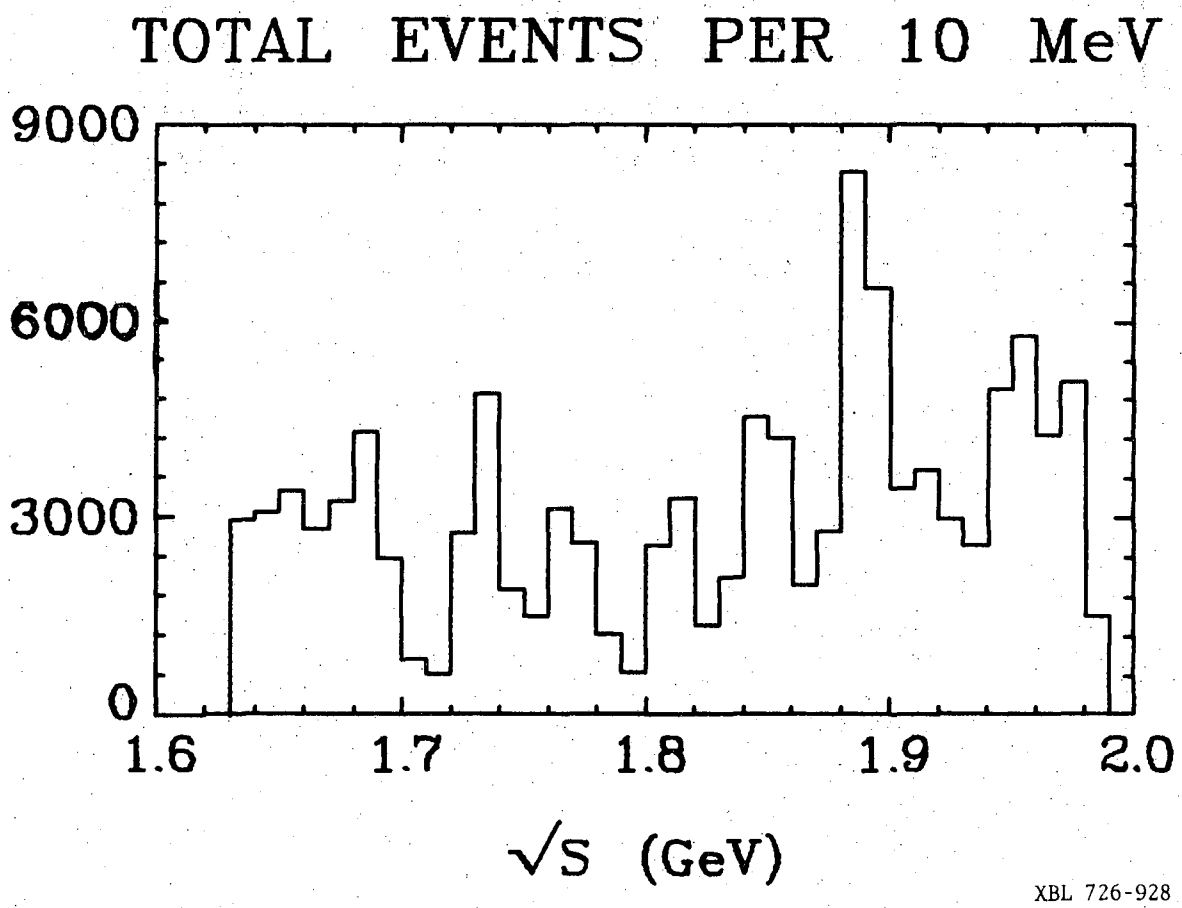
TOTAL EVENTS PER 10 MeV
9000
6000
3000
0
1.6
1.7
1.8
1.9
2.0
√S (GeV)
XBL 726-928

Fig. 6.

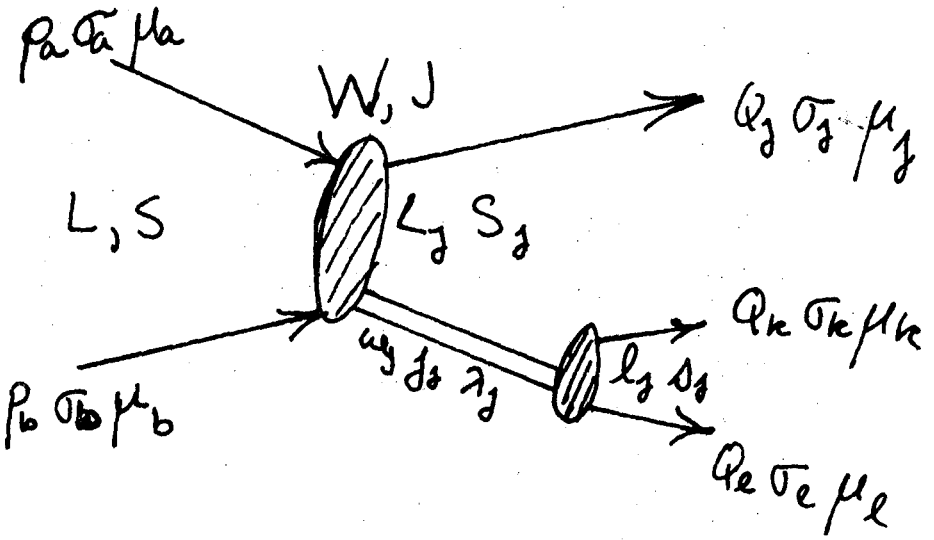

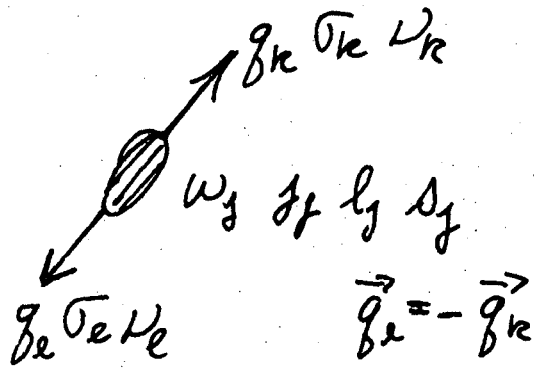

XBL 726-929

Fig. 7.

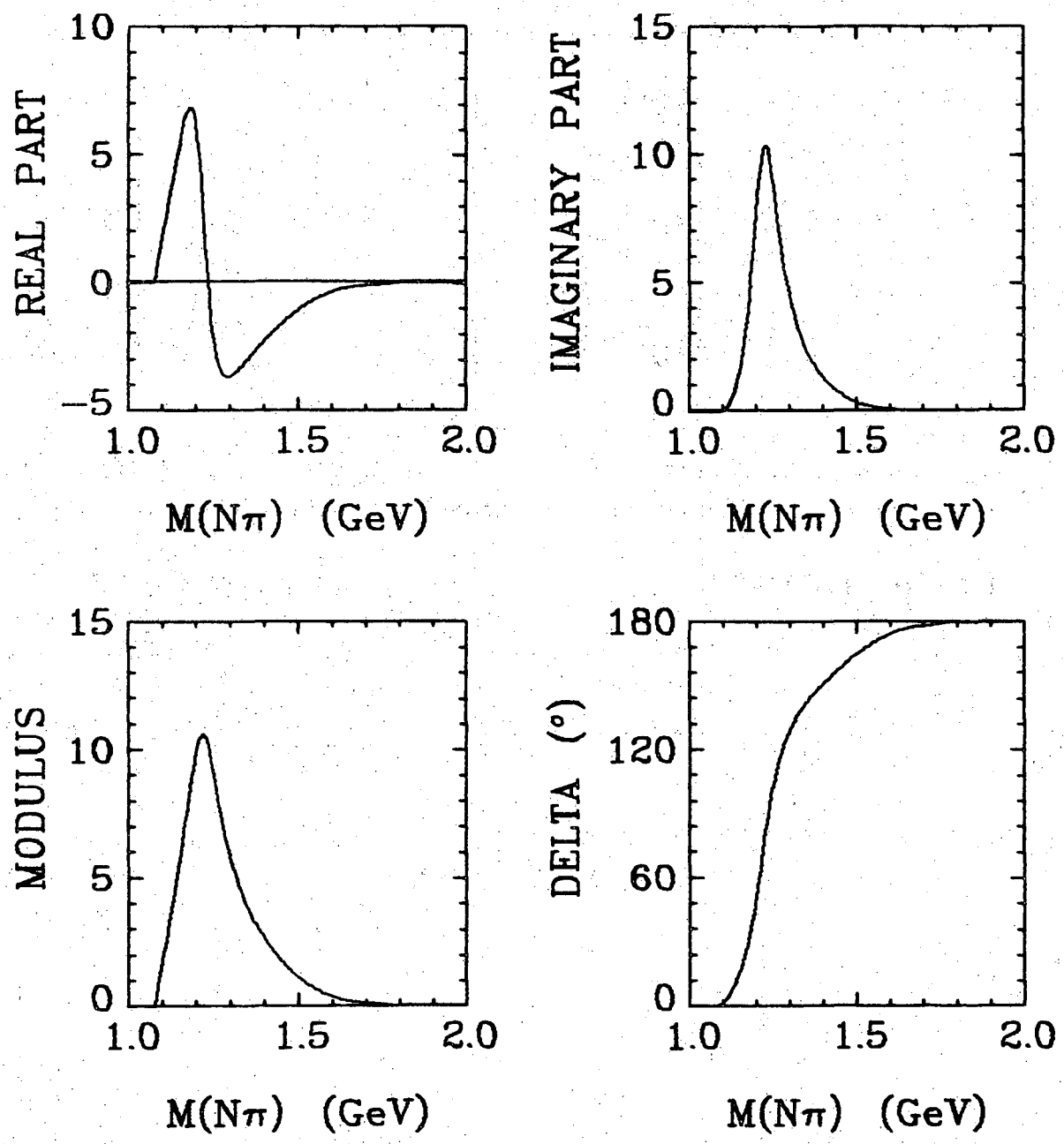
REAL PART
10
5
0
−5
1.0
1.5
2.0
M(Nπ) (GeV)
IMAGINARY PART
15
10
5
0
1.0
1.5
2.0
M(Nπ) (GeV)
MODULUS
15
10
5
0
1.0
1.5
2.0
M(Nπ) (GeV)
DELTA (°)
180
120
60
0
1.0
1.5
2.0
M(Nπ) (GeV)
XBL 726-930

Fig. 8.

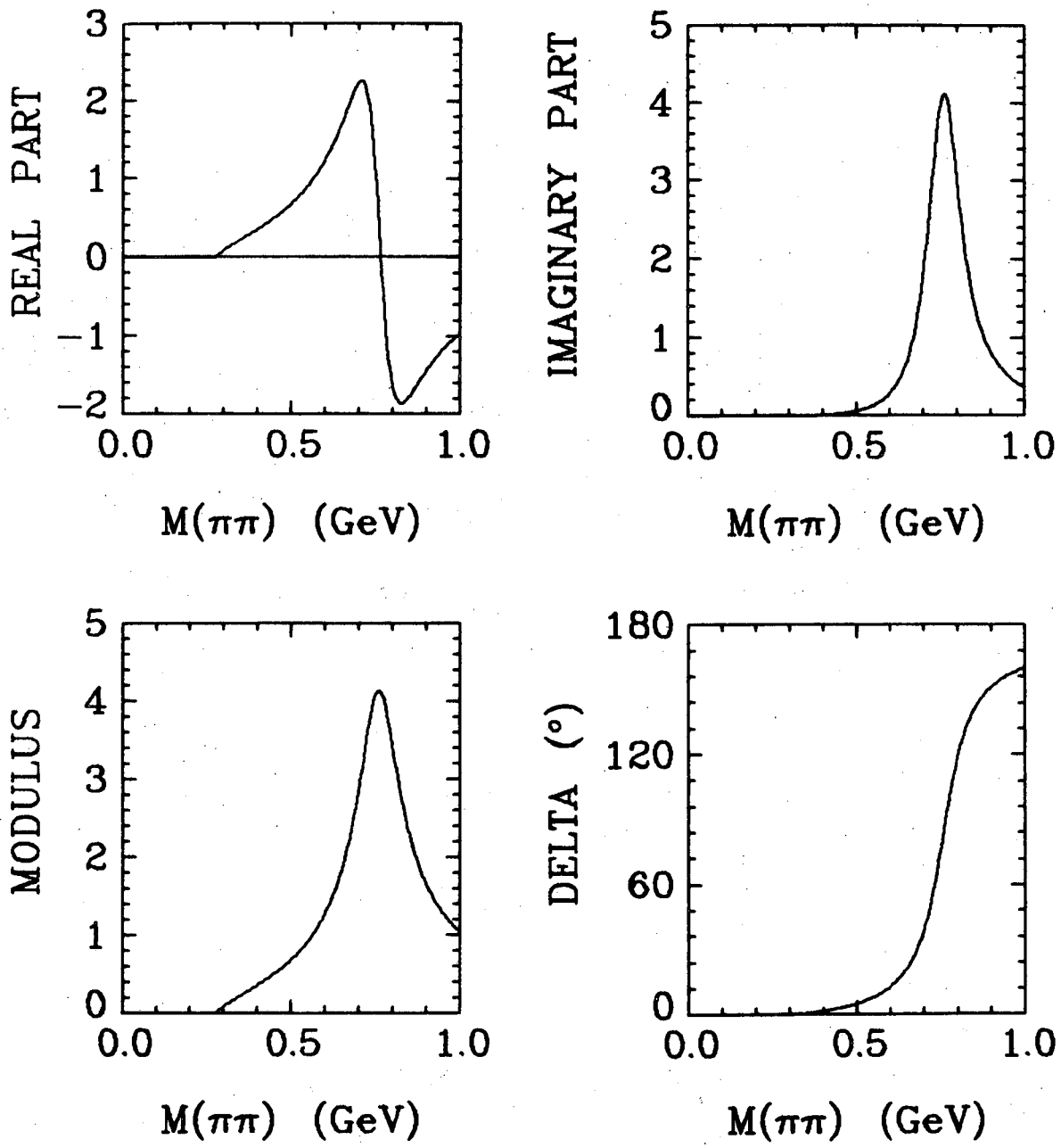

Fig. 9.

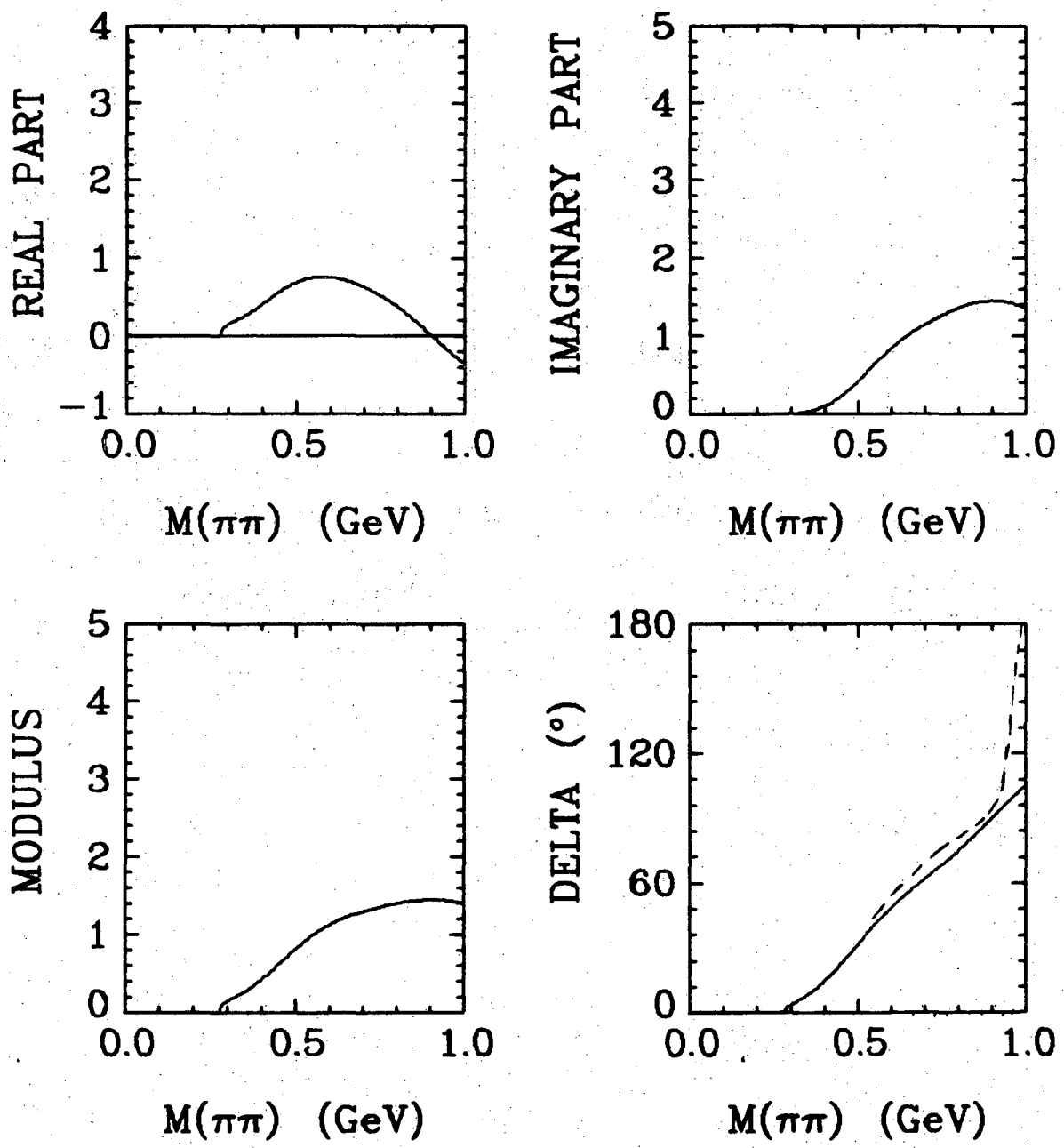
REAL PART
IMAGINARY PART
MODULUS
DELTA (°)
M(ππ) (GeV)
M(ππ) (GeV)
M(ππ) (GeV)
M(ππ) (GeV)
XBL 726-932

Fig. 10.

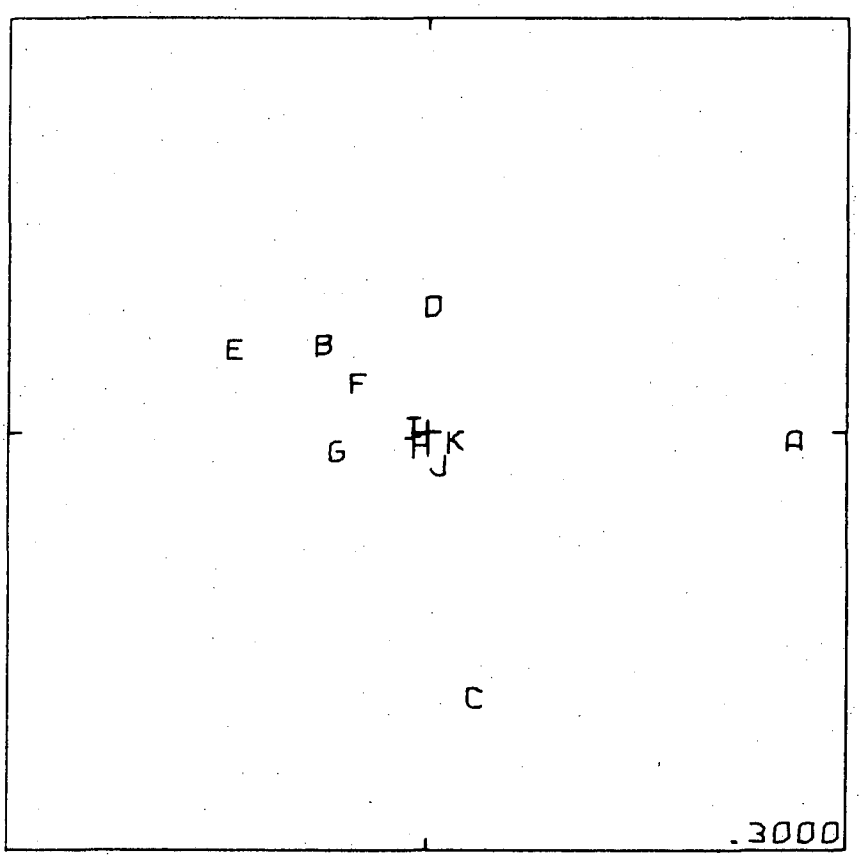

A	P33	PP11
B	P33	SD11
C	P33	DD13
D	P33	DD15
E	P33	SD31
F	RH3	DS13
G	RH3	PP13
H	RH3	DD13
I	RH3	PF13
J	SIG	FD15
K	SIG	DF15

XBL 726-933

Fig. 11.

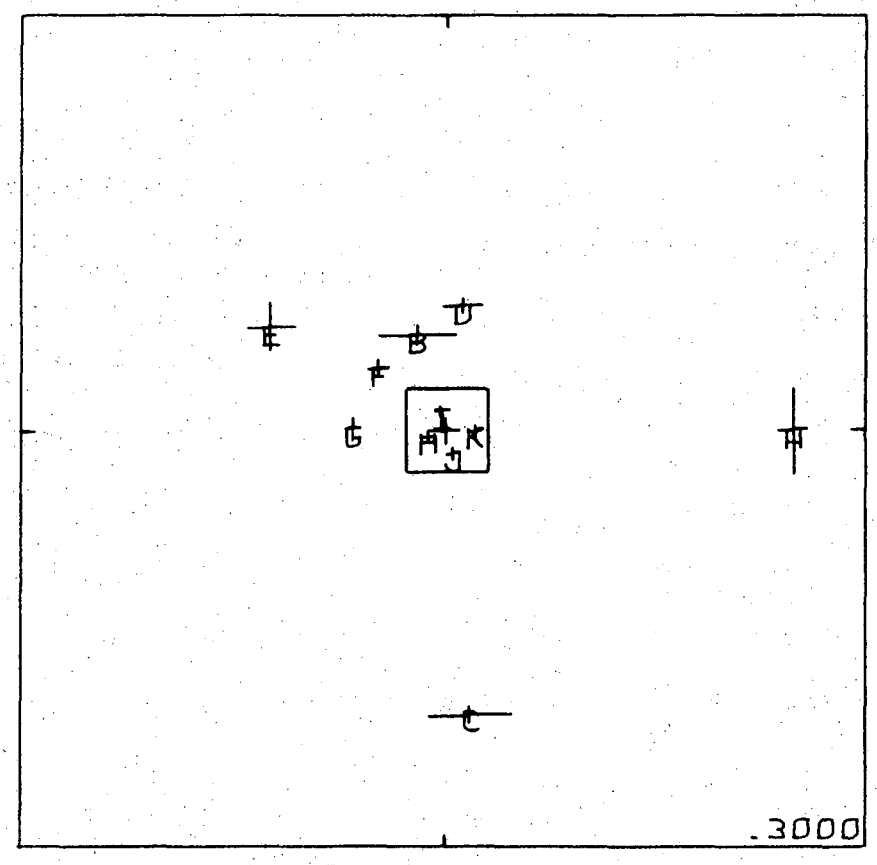

A	P33	PP11
B	P33	SD11
C	P33	DD13
D	P33	DD15
E	P33	SD31
F	RH3	DS13
G	RH3	PP13
H	RH3	DD13
I	RH3	PF13
J	SIG	FD15
K	SIG	DF15

FITTED AMPLITUDES

XBL 726-934

Fig. 12a.

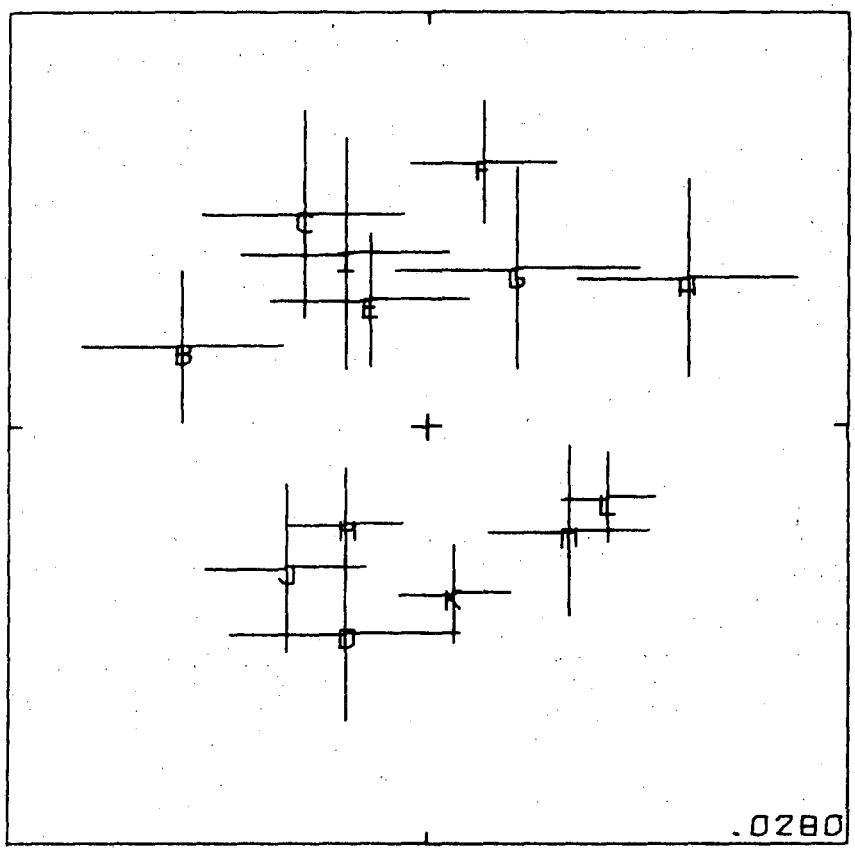

A	P33	DS13
B	P33	FF15
C	P33	DS33
D	P33	DD33
E	P33	FF35
F	P33	FF37
G	RH3	SD11
H	RH3	FP15
I	RH3	PP31
J	RH3	DS33
K	RH3	FF35
L	RH1	FF37
M	SIG	PD13

XBL 726-935

Fig. 12b.

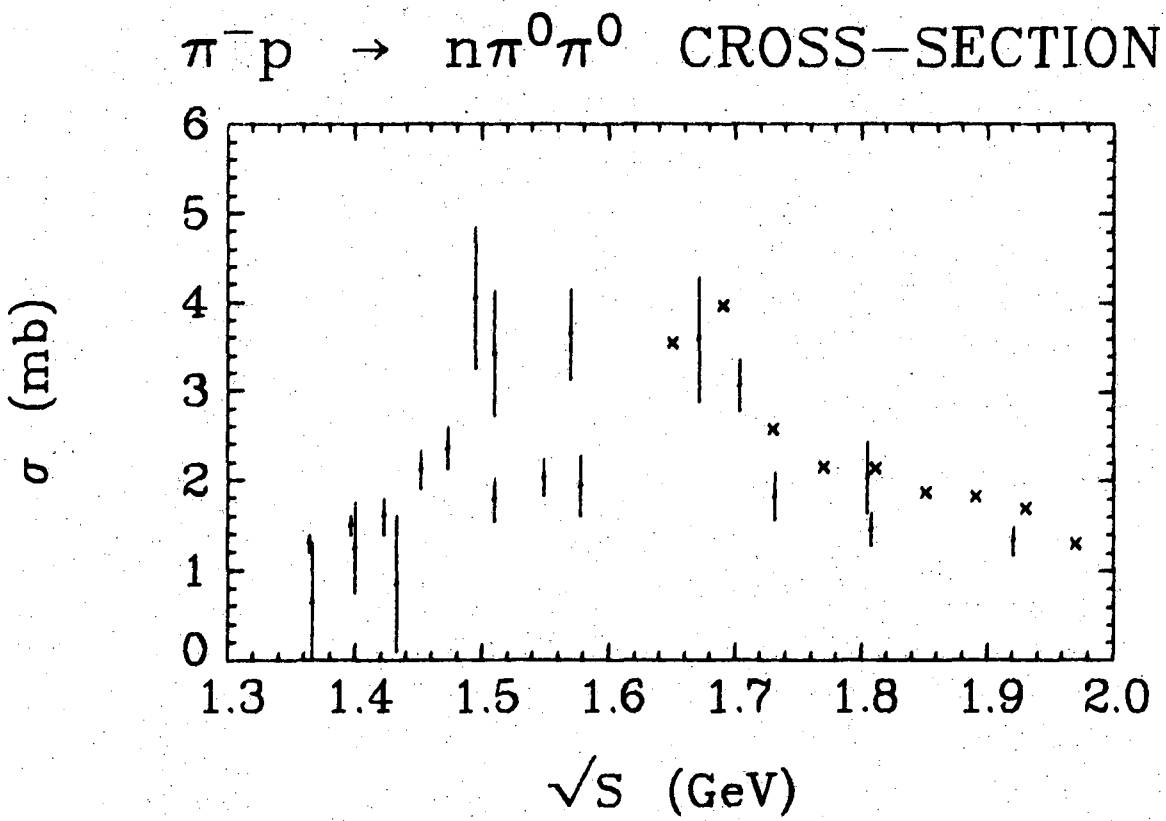
$\pi^- p \rightarrow n\pi^0\pi^0$ CROSS-SECTION
σ (mb)
0
1
2
3
4
5
6
1.3
1.4
1.5
1.6
1.7
1.8
1.9
2.0
√S (GeV)
XBL 726-936

Fig. 13.

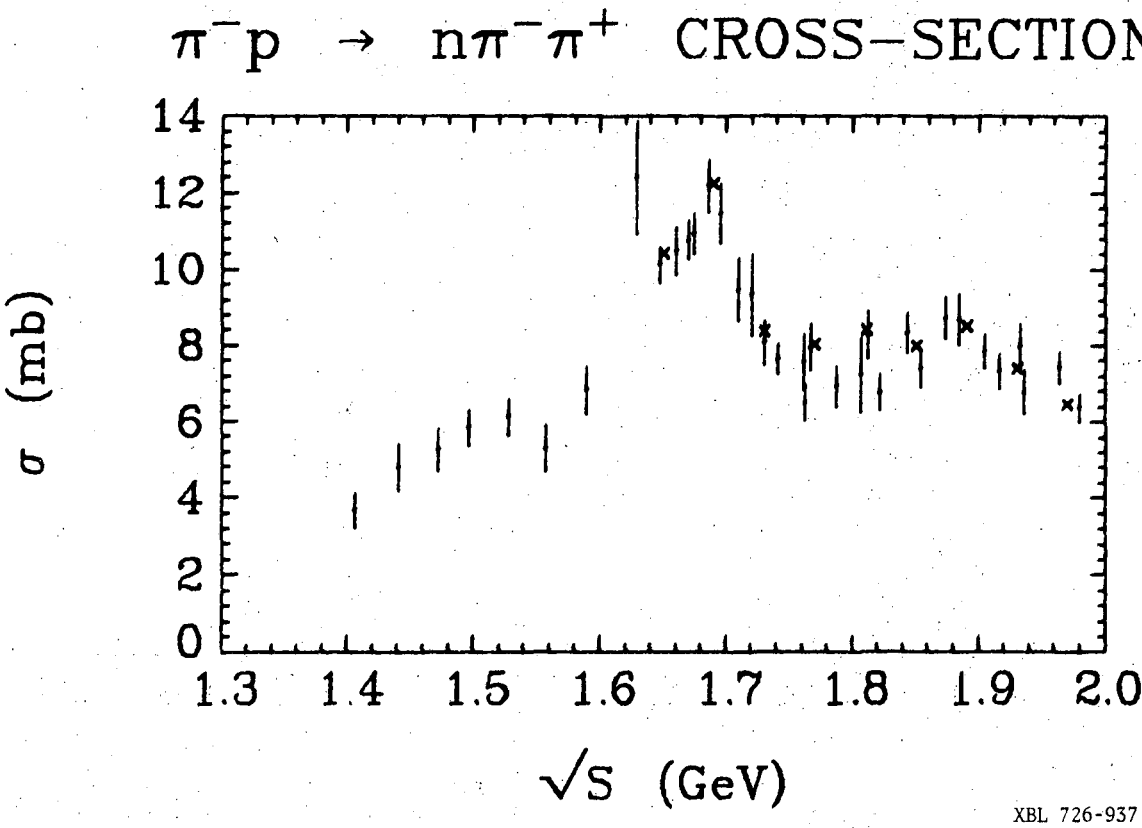

Fig. 14.

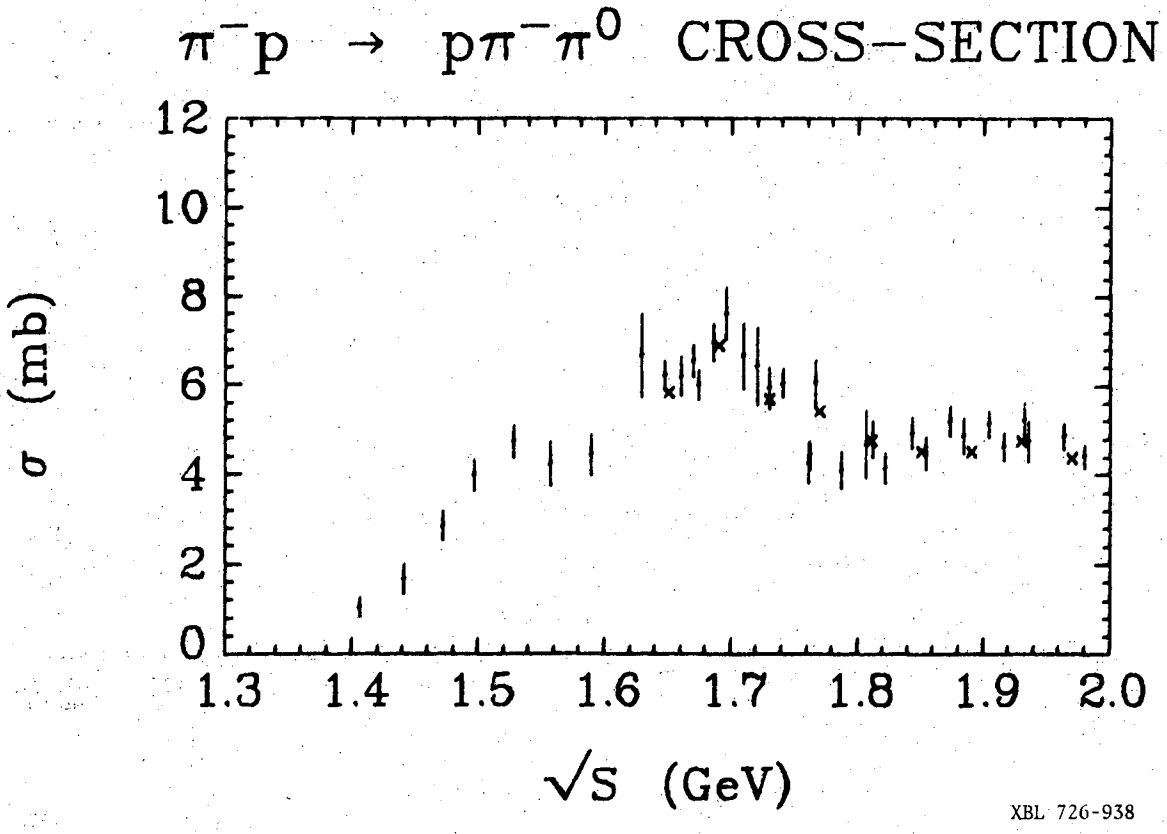
$\pi^- p \rightarrow p\pi^-\pi^0$ CROSS-SECTION
σ (mb)
12
10
8
6
4
2
0
1.3
1.4
1.5
1.6
1.7
1.8
1.9
2.0
√S (GeV)
XBL 726-938

Fig. 15.

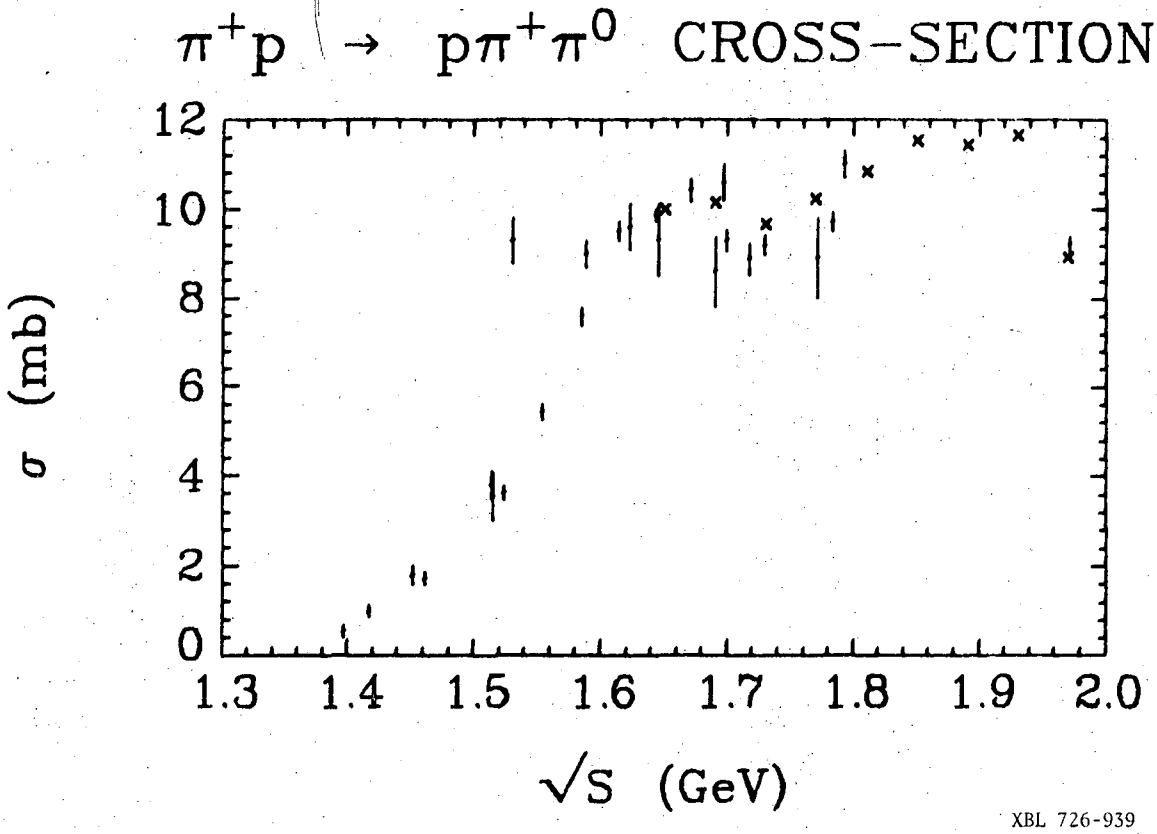

Fig. 16.

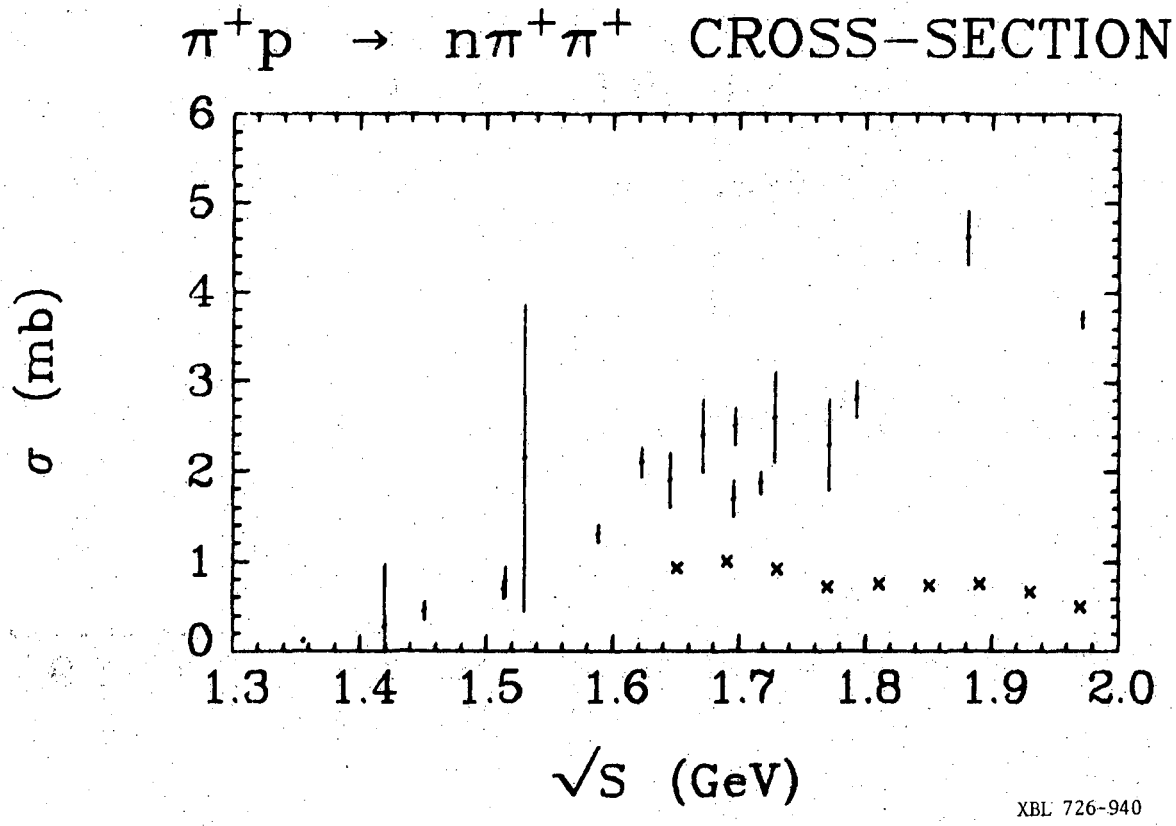
$\pi^+p \rightarrow n\pi^+\pi^+$ CROSS-SECTION
σ (mb)
0
1
2
3
4
5
6
1.3
1.4
1.5
1.6
1.7
1.8
1.9
2.0
√S (GeV)
XBL 726-940

Fig. 17.

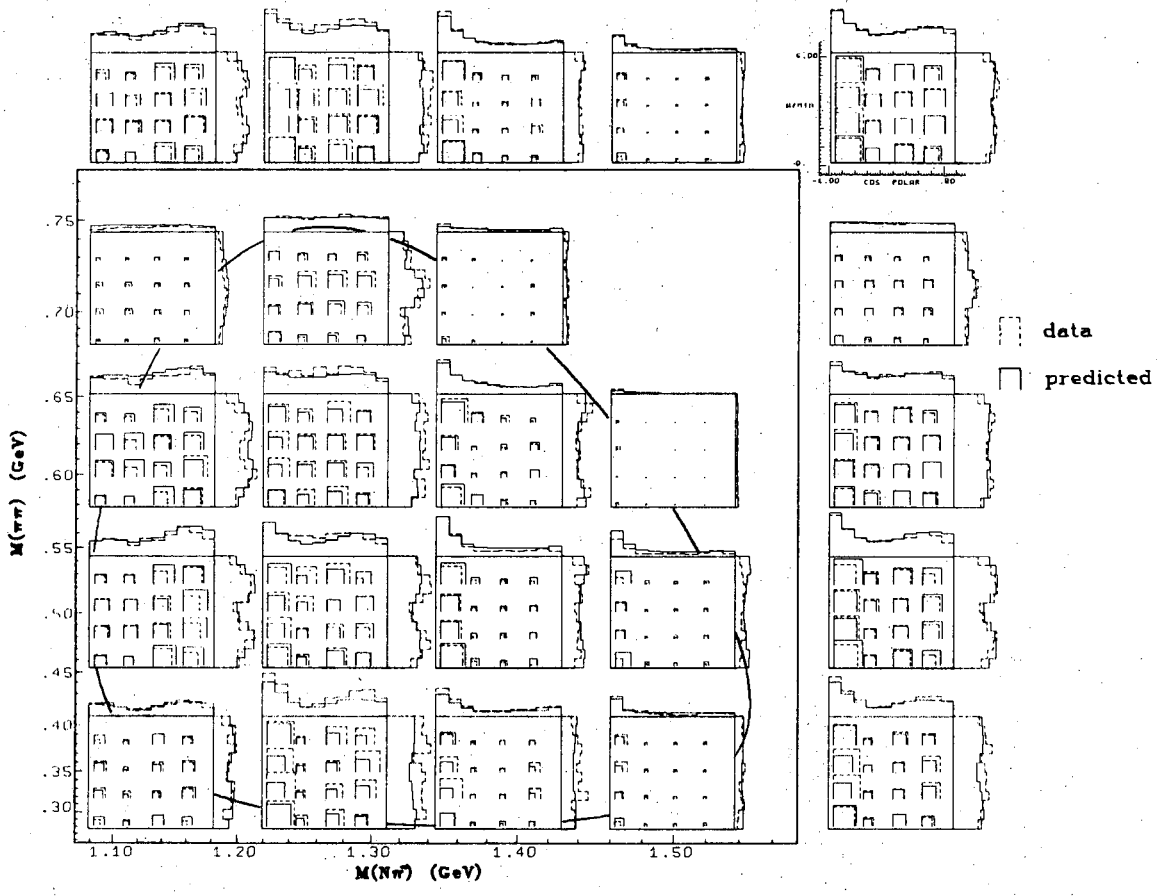

XBL 726-941

Fig.18a.

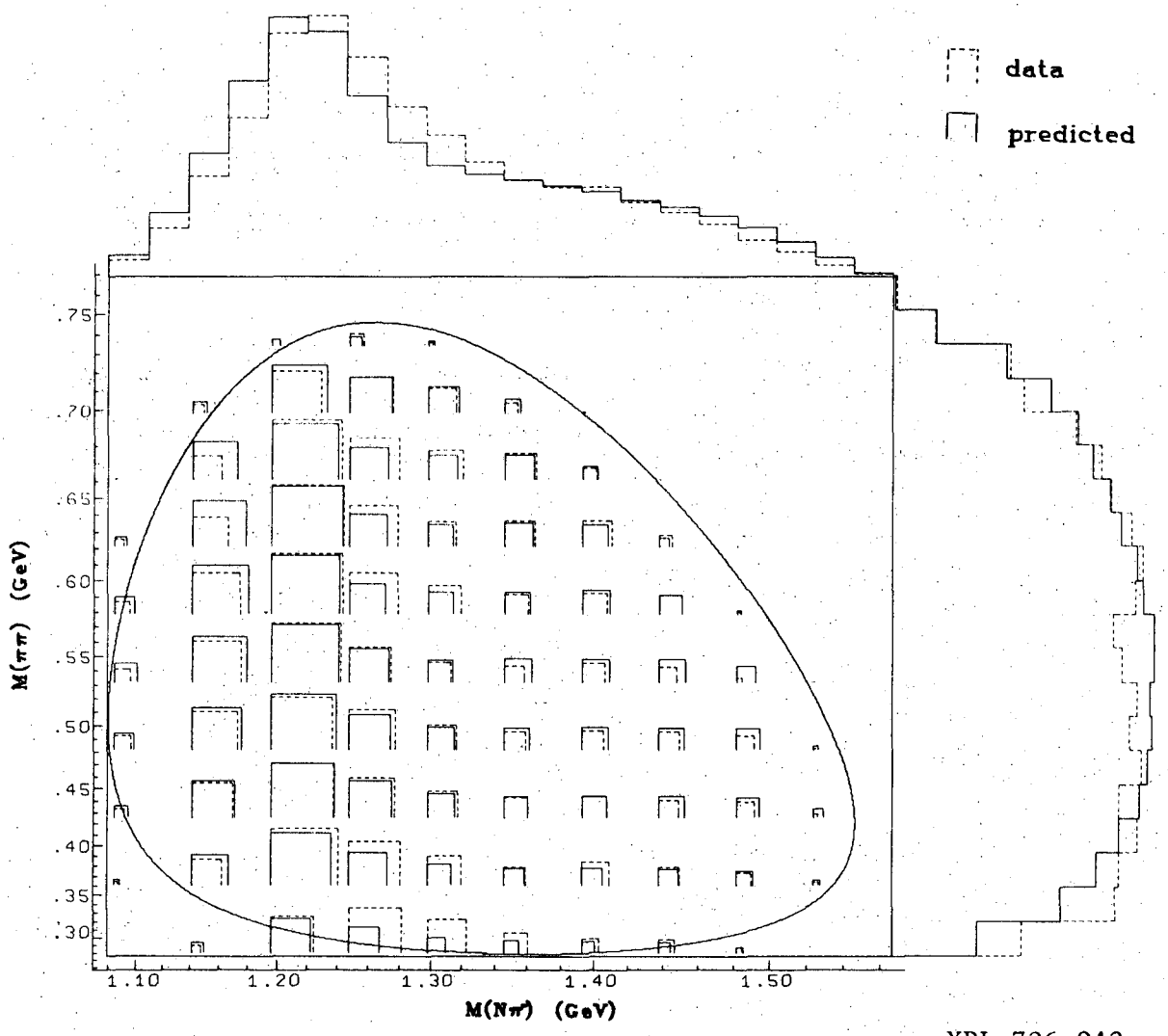

XBL 726-942

Fig. 18b.

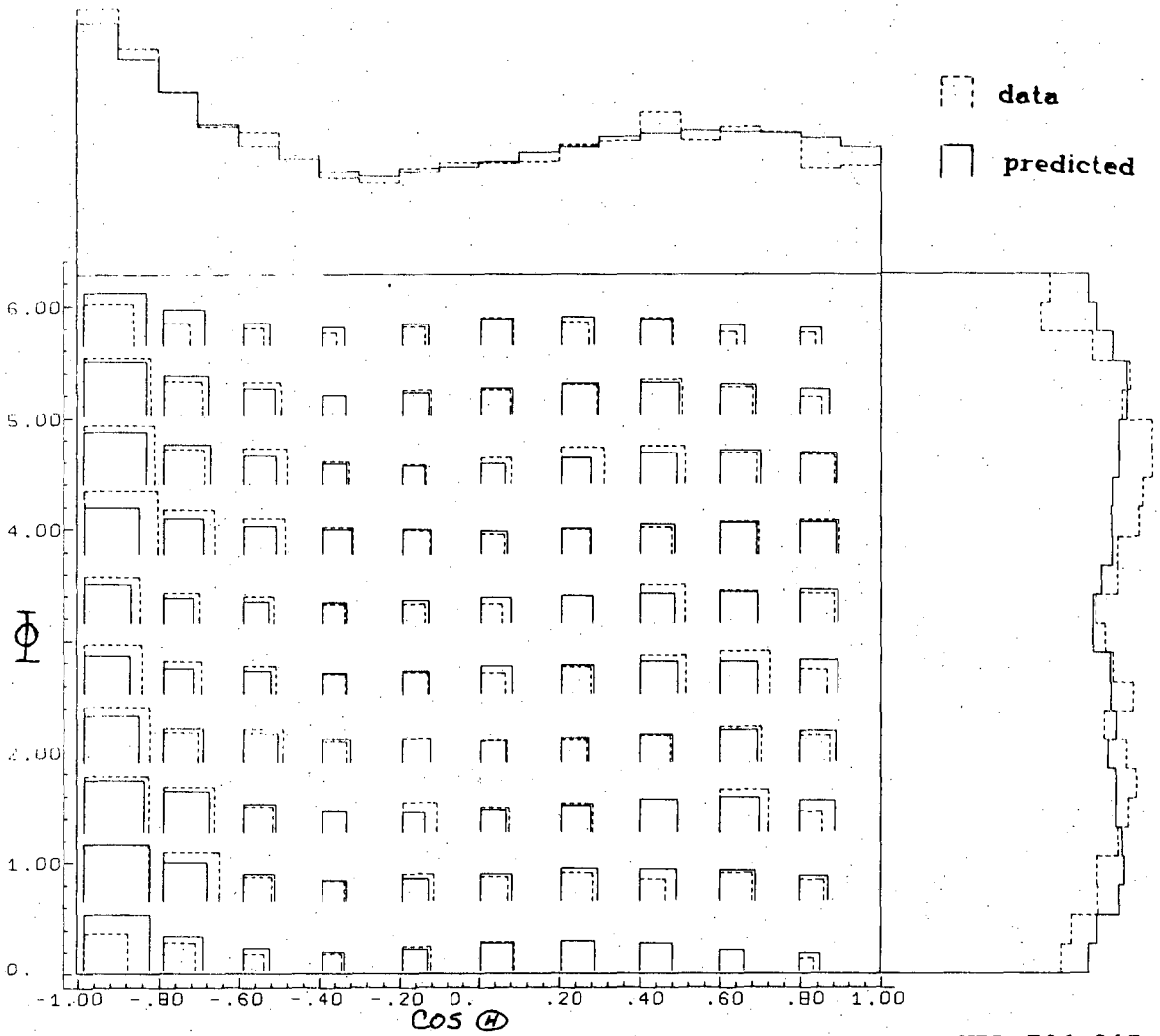
data
predicted
6.00
5.00
4.00
Φ
2.00
1.00
0.
-1.00 -.80 -.60 -.40 -.20 0. .20 .40 .60 .80 1.00
Cos Θ
XBL 726-943

Fig. 18c.

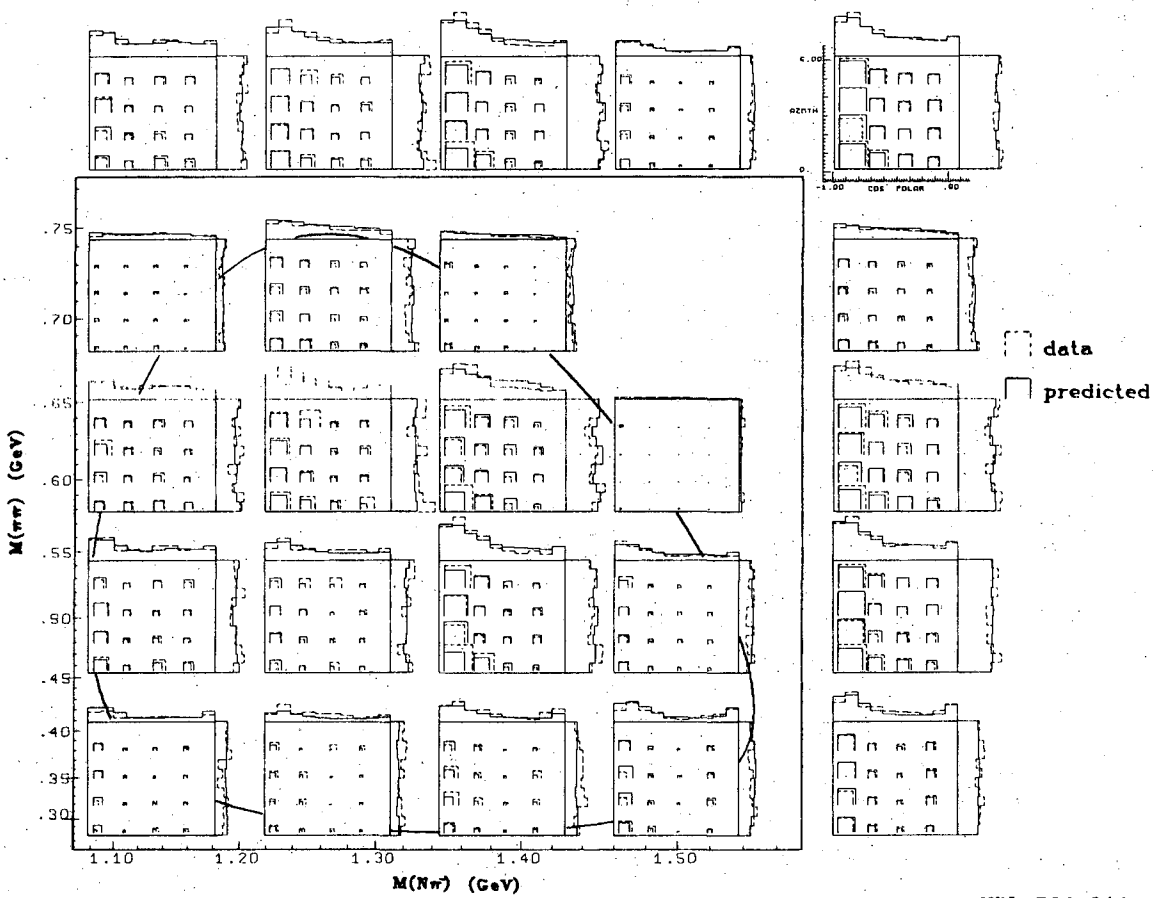

XBL 726-944

Fig. 19a.

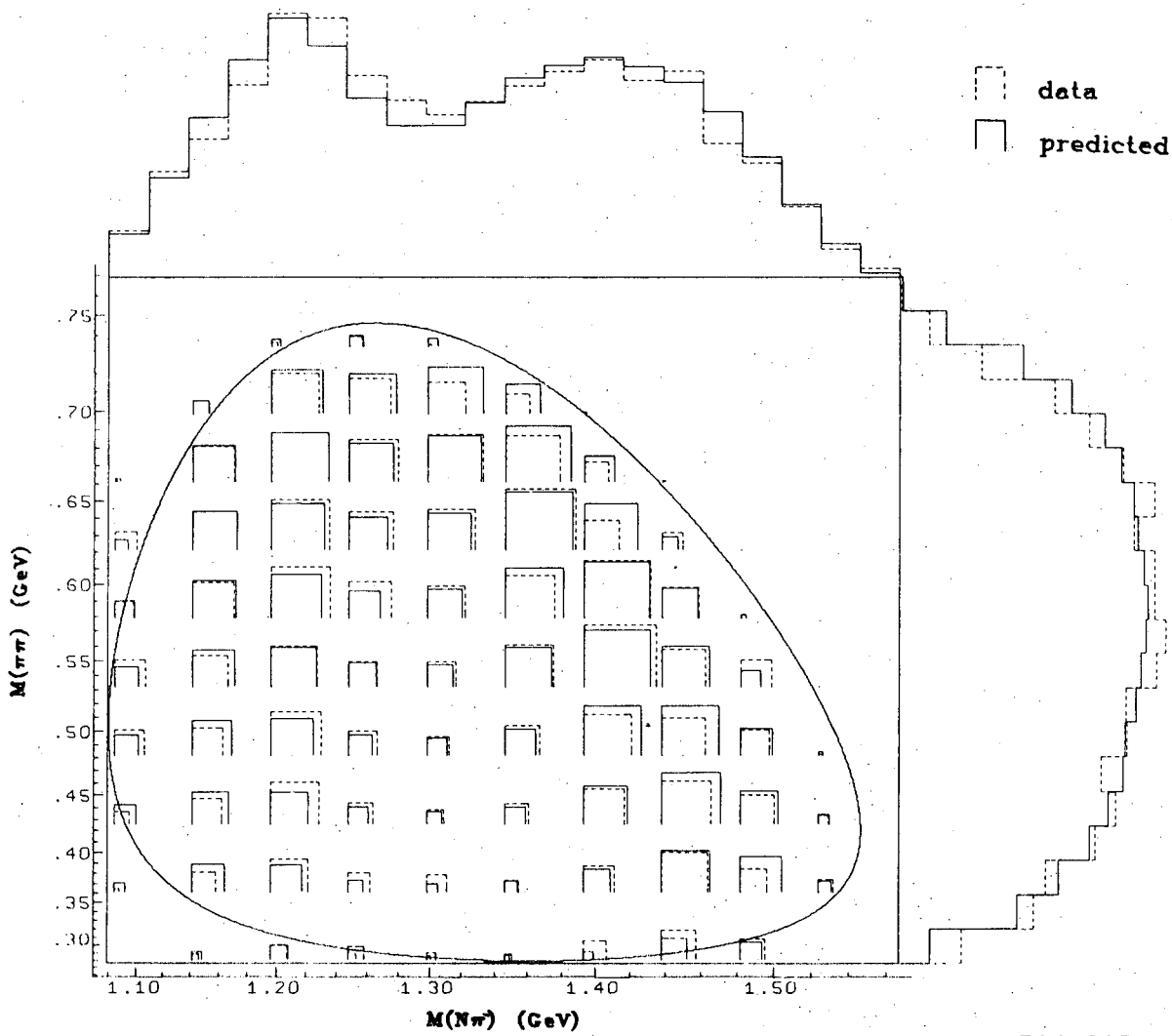

XBL 726-945

Fig. 19b.

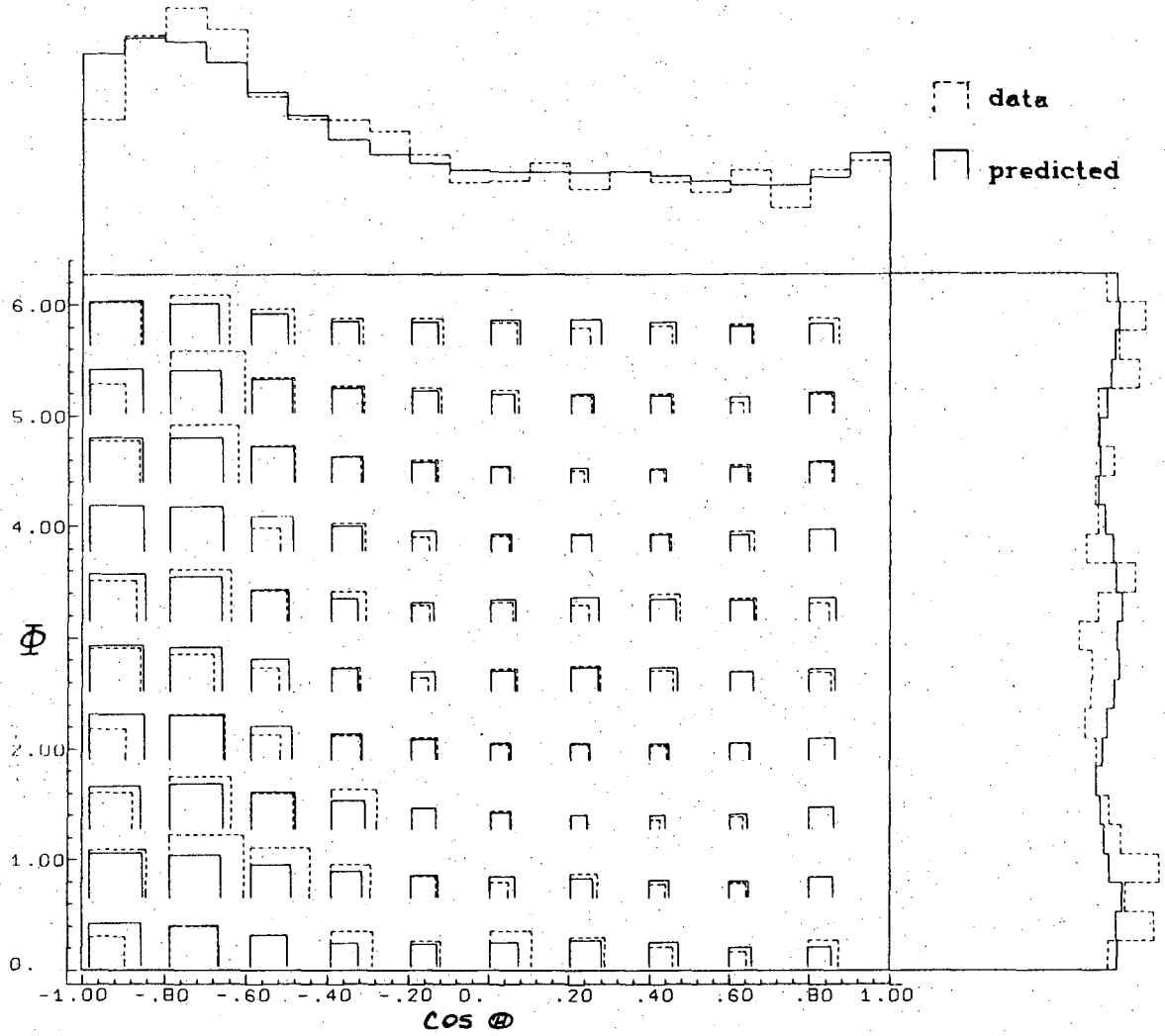

XBL 726-946

Fig. 19c.

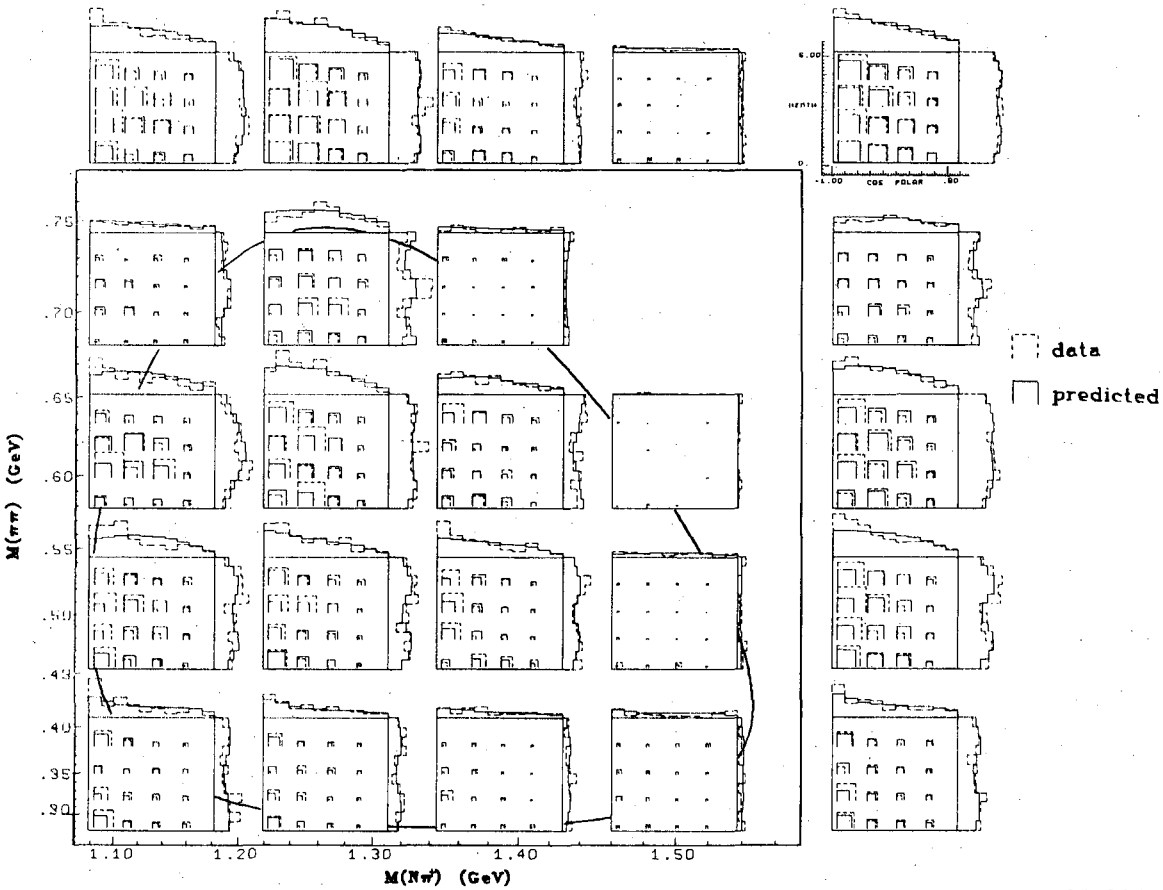

XBL 726-947

Fig. 20a.

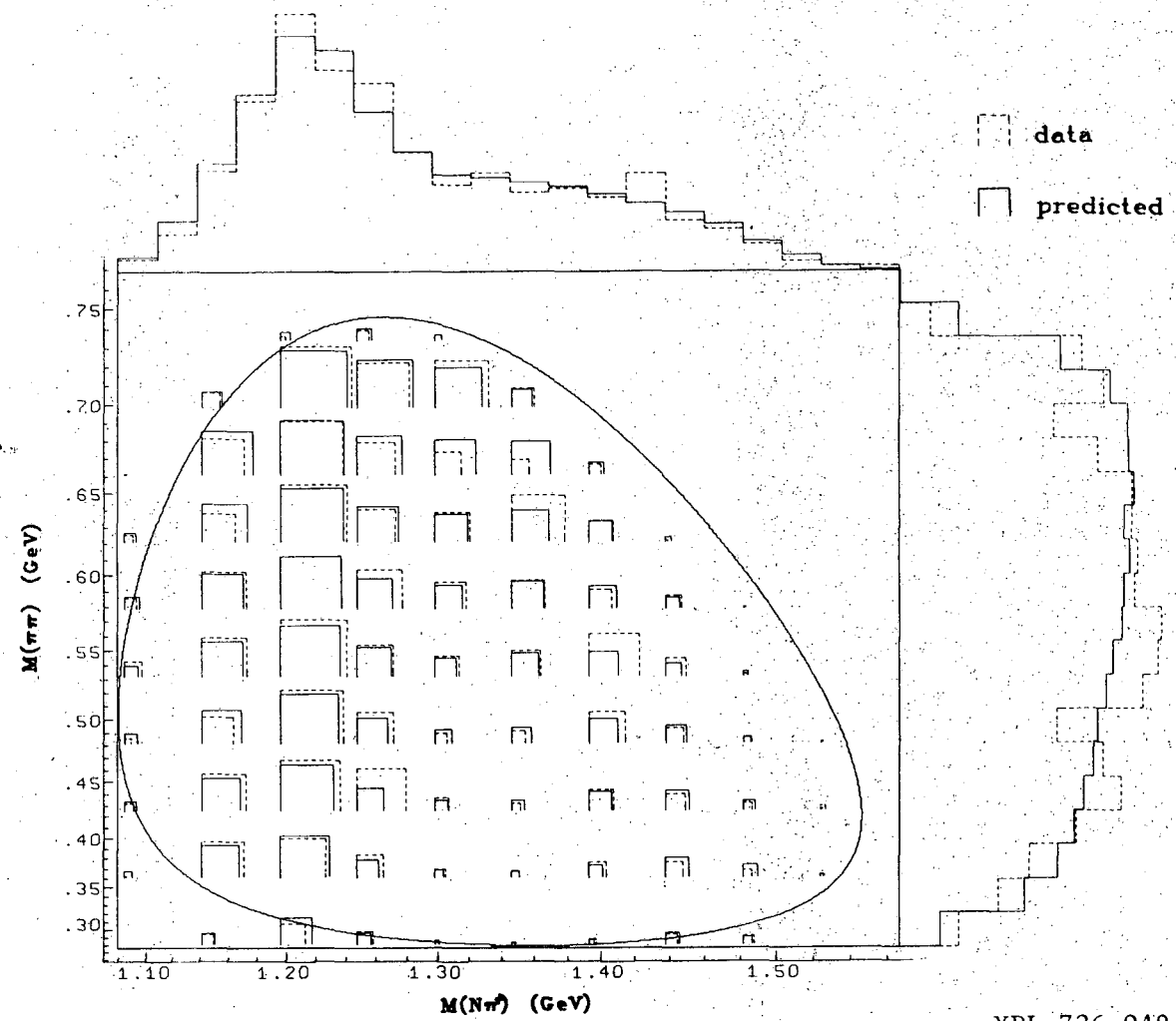

XBL 726-948

Fig. 20b.

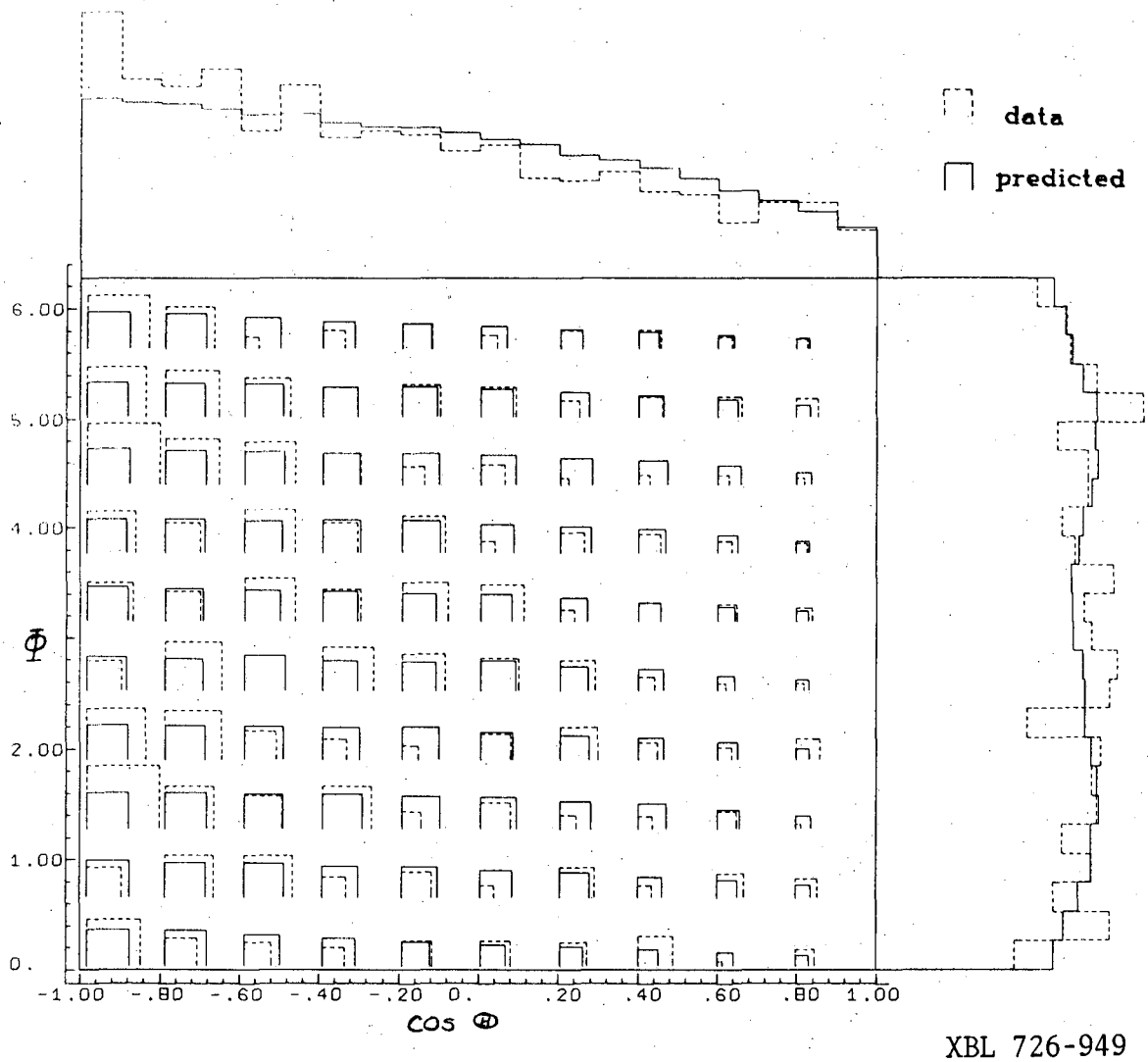
data
predicted
6.00
5.00
4.00
Φ
2.00
1.00
0.
-1.00 -.80 -.60 -.40 -.20 0. .20 .40 .60 .80 1.00
cos Θ
XBL 726-949

Fig. 20c.

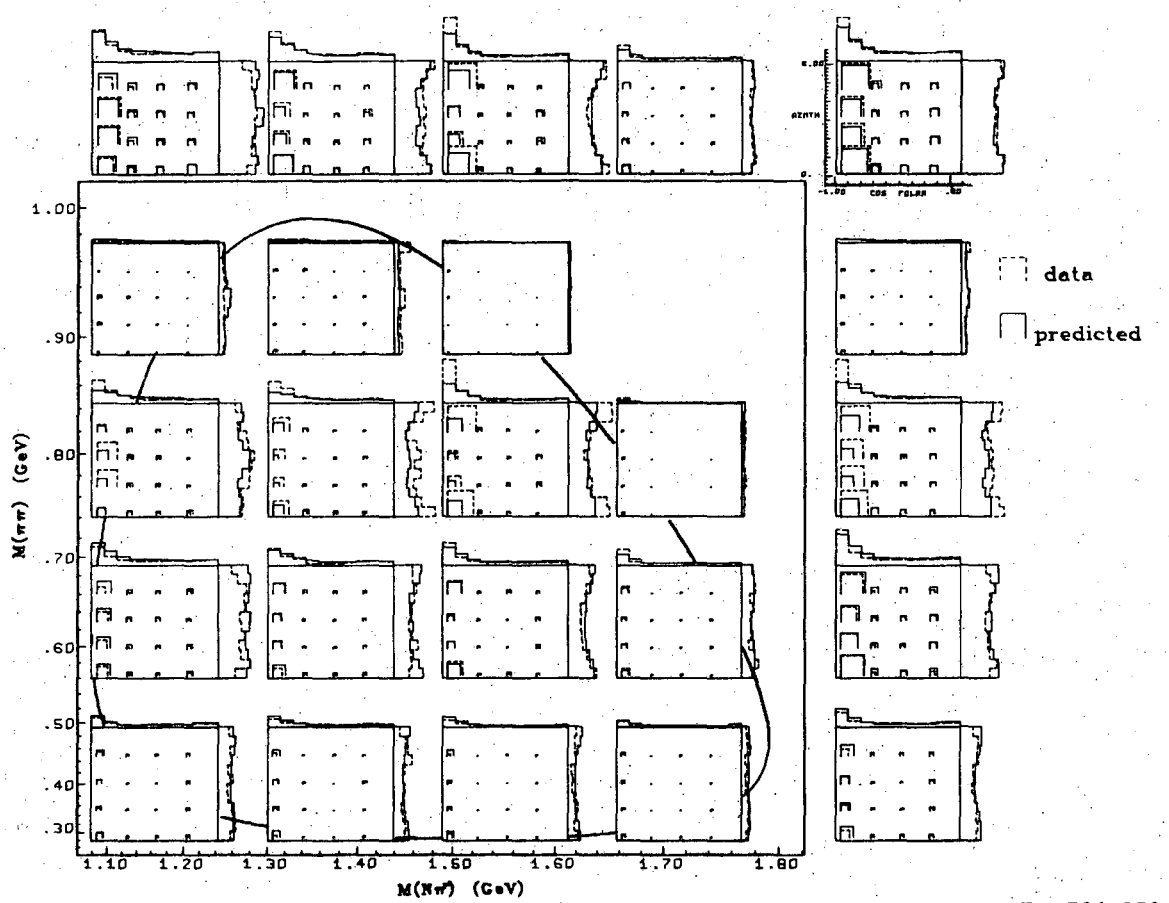
data
predicted
M(πw) (GeV)
M(Nw) (GeV)
1.00
.90
.80
.70
.60
.50
.40
.30
1.10
1.20
1.30
1.40
1.50
1.60
1.70
1.80
XBL 726-950

Fig. 21a.

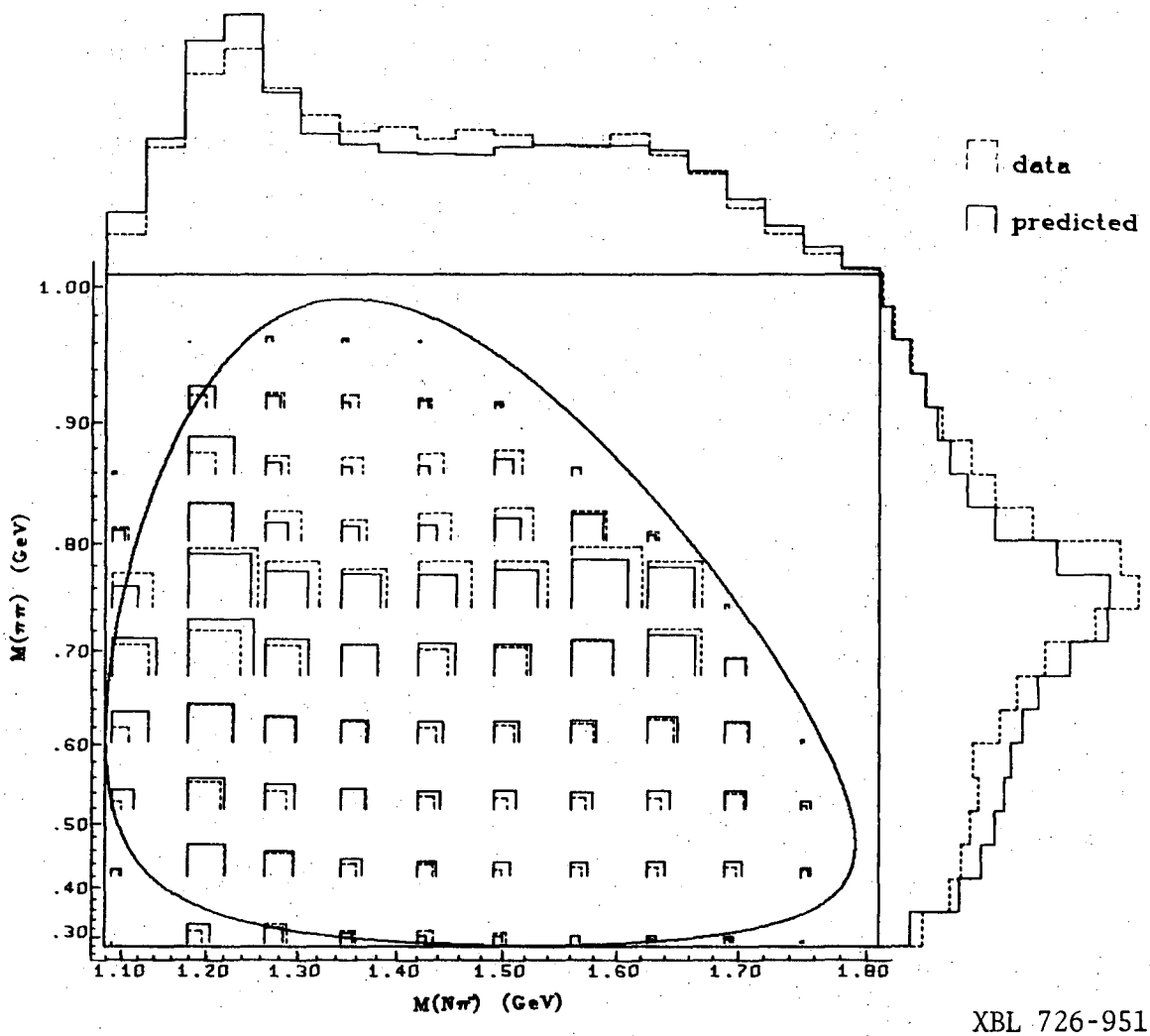
data
predicted
1.00
.90
.80
.70
.60
.50
.40
.30
M(ππ) (GeV)
1.10
1.20
1.30
1.40
1.50
1.60
1.70
1.80
M(Nπ) (GeV)
XBL 726-951

Fig. 21b.

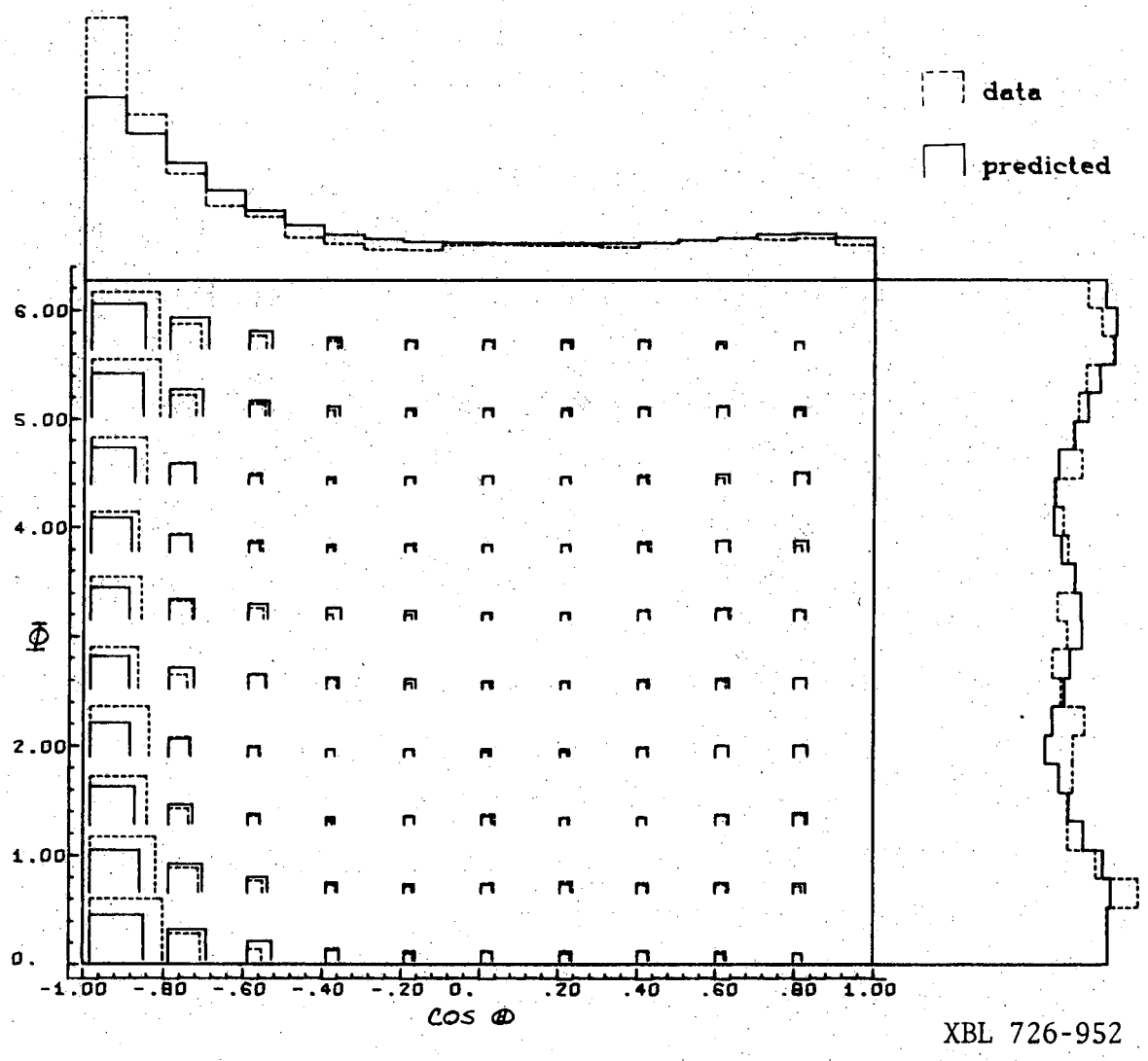
data
predicted
6.00
5.00
4.00
Φ
2.00
1.00
0.
-1.00
-.80
-.60
-.40
-.20
0.
.20
.40
.60
.80
1.00
cos Φ
XBL 726-952

Fig. 21c.

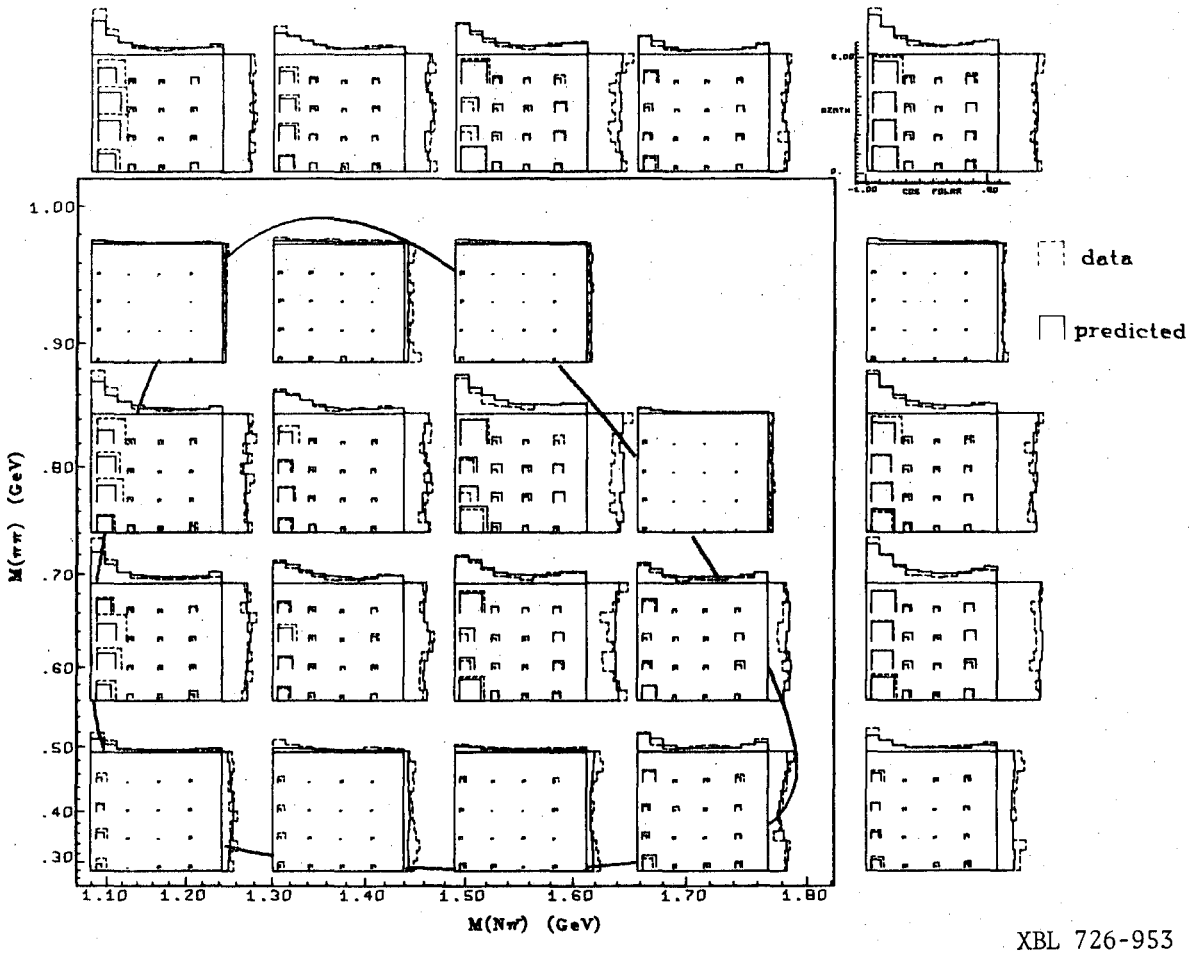

Fig. 22a.

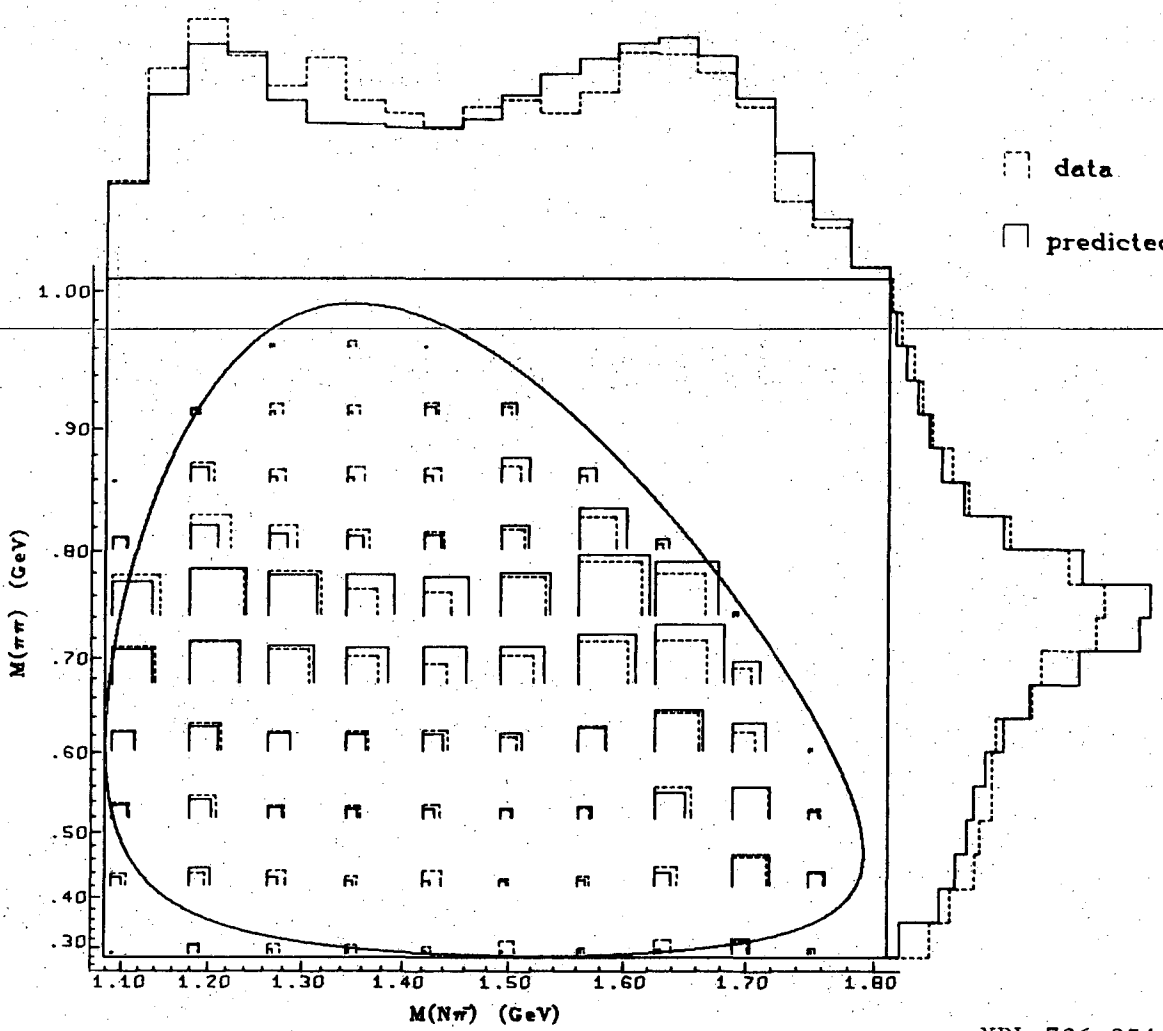

XBL 726-954

Fig. 22b.

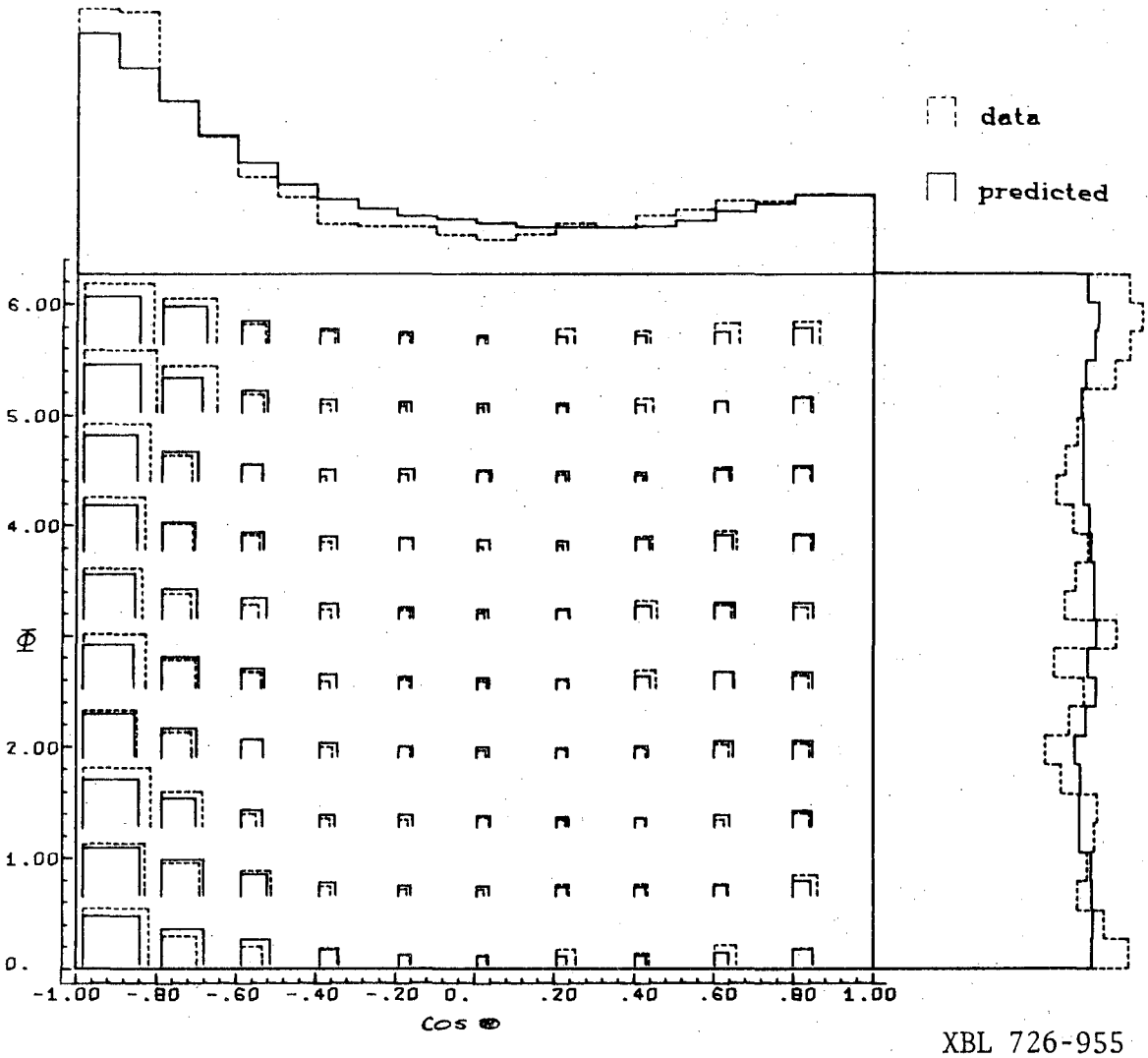

Fig. 22c.

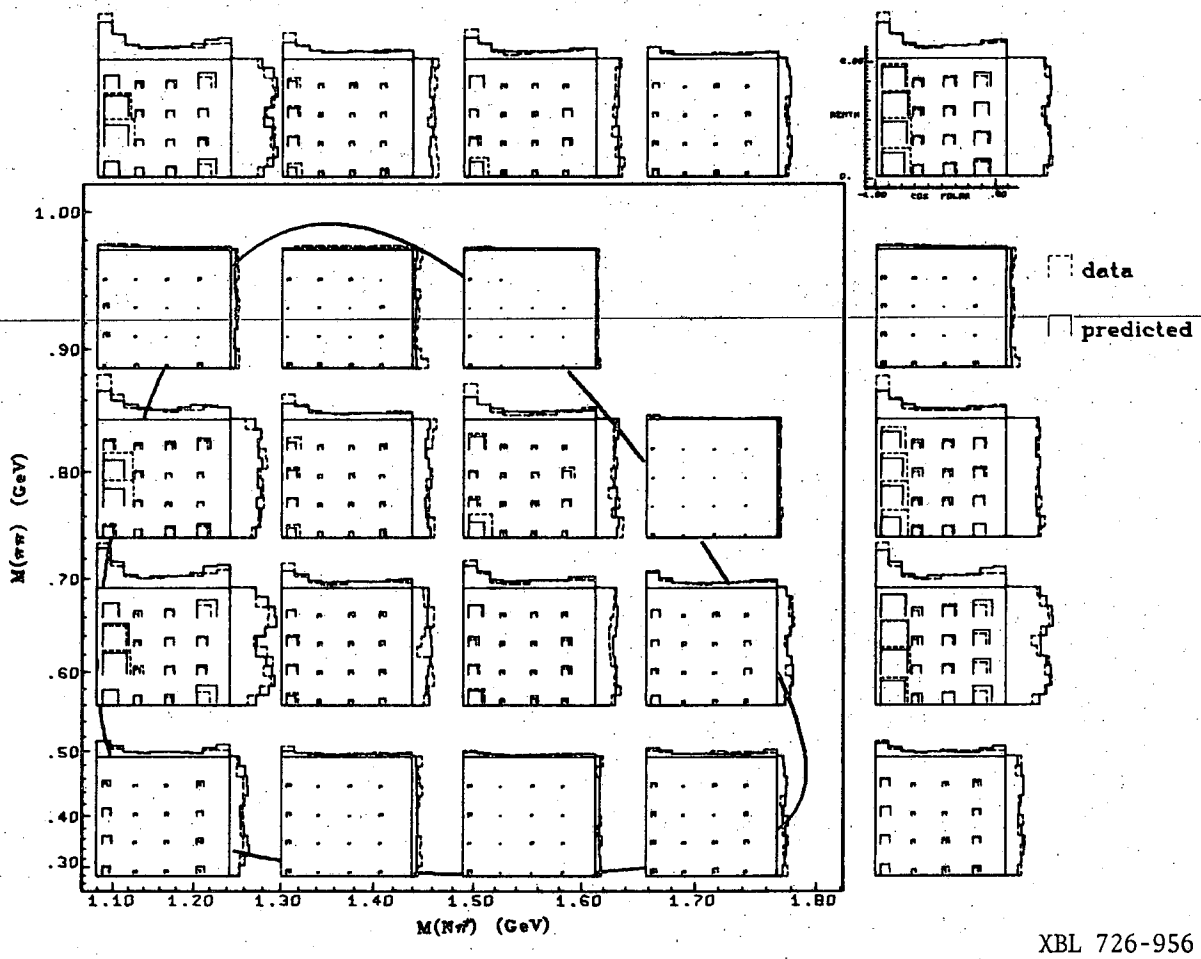

XBL 726-956

Fig. 23a.

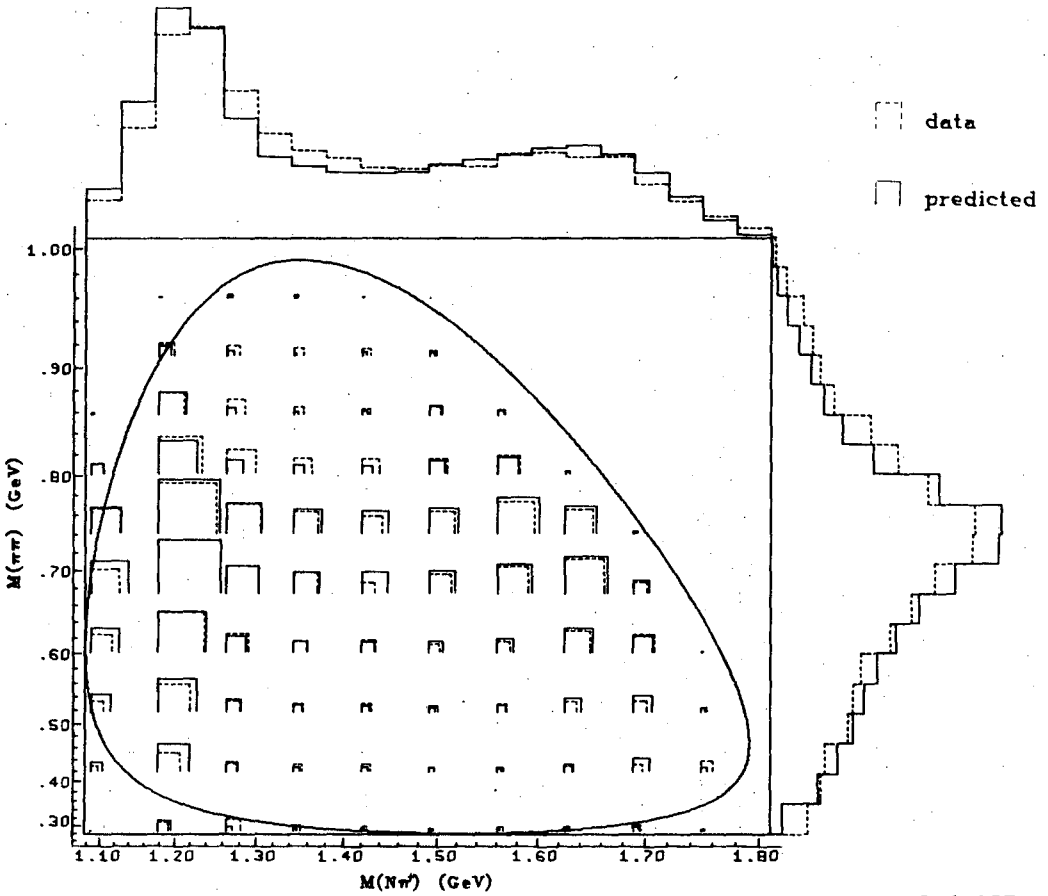

XBL 726-957

Fig. 23b.

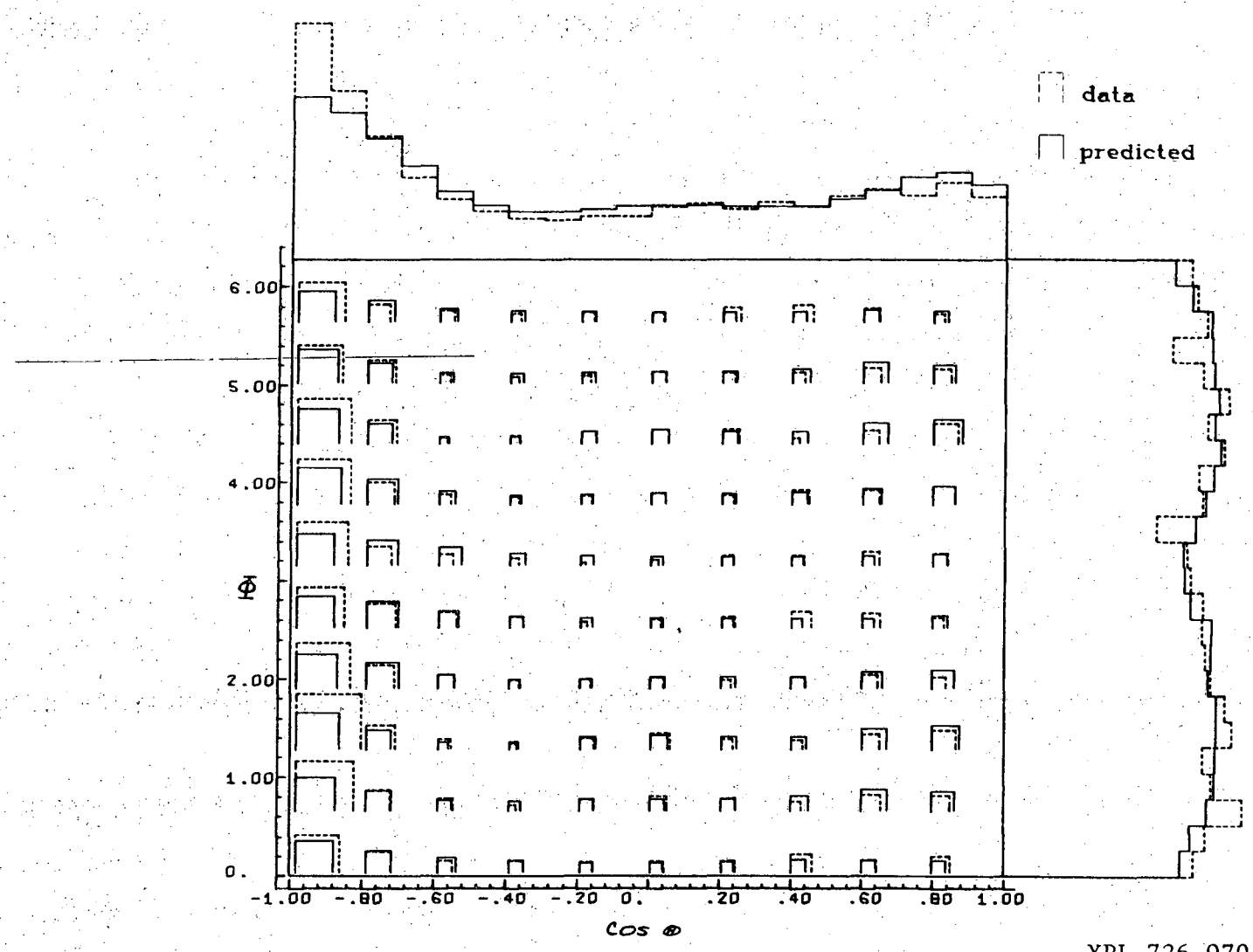

XBL 726-970

Fig. 23c.

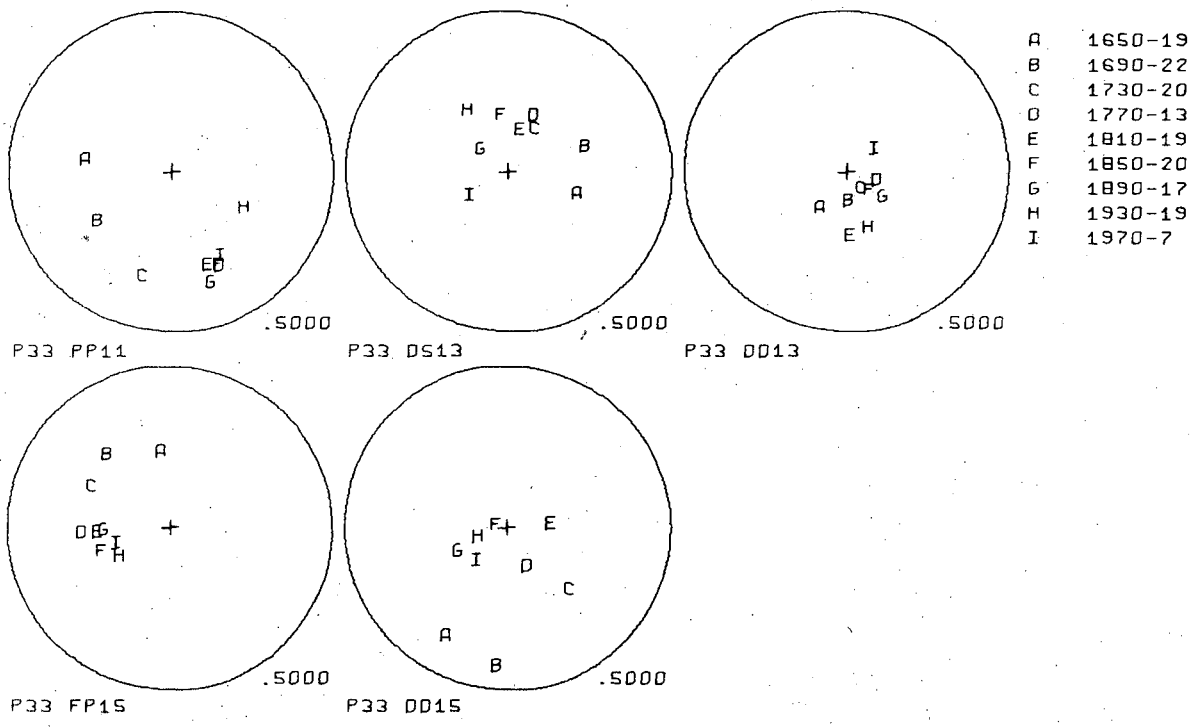

XBL 726-971

Fig. 24.

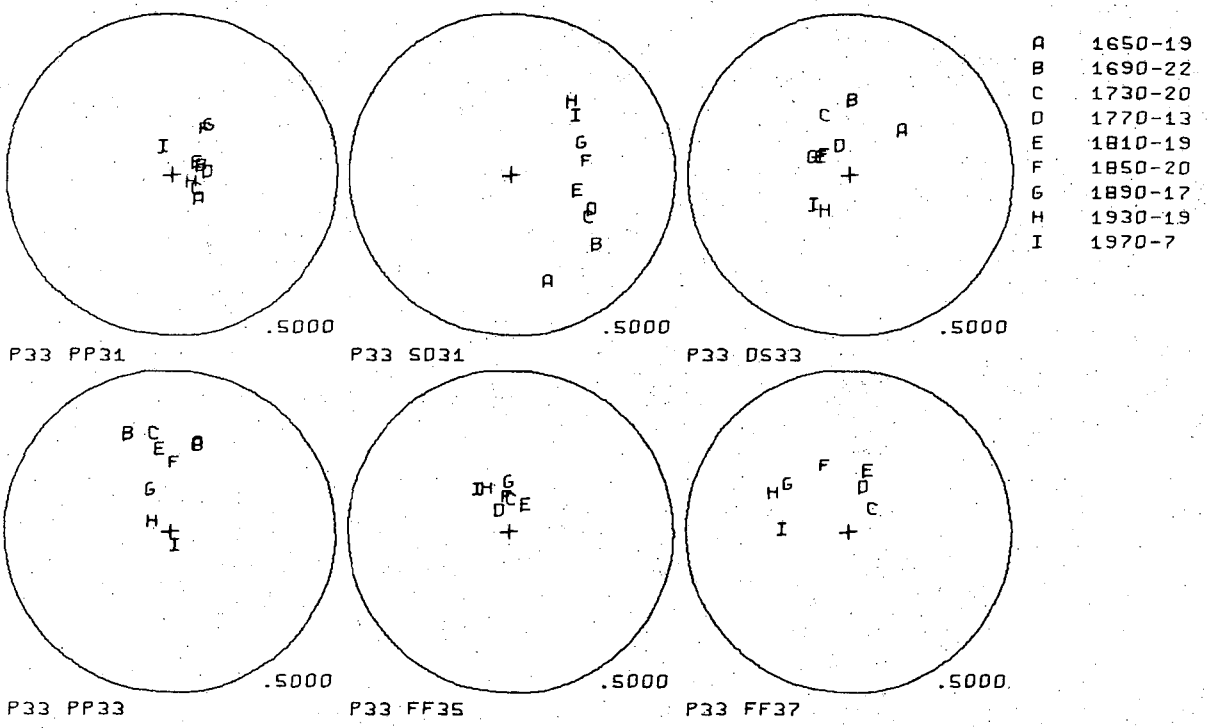

XBL 726-972

Fig. 25.

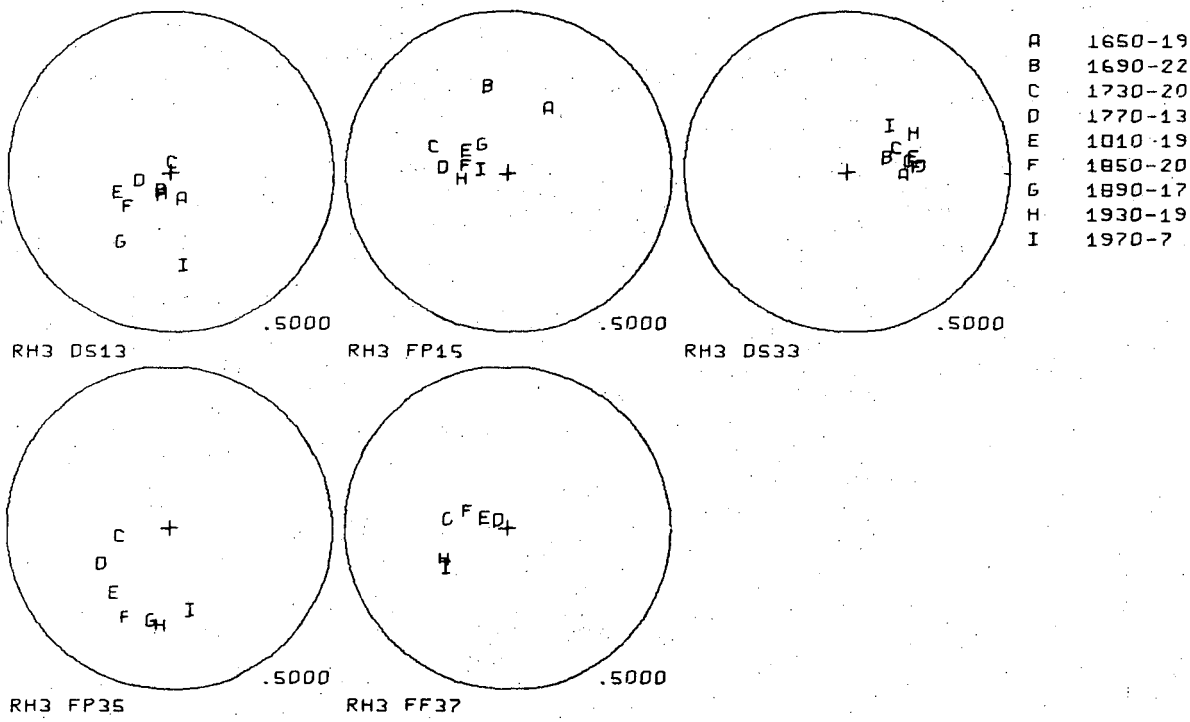

XBL 726-973

Fig. 26.

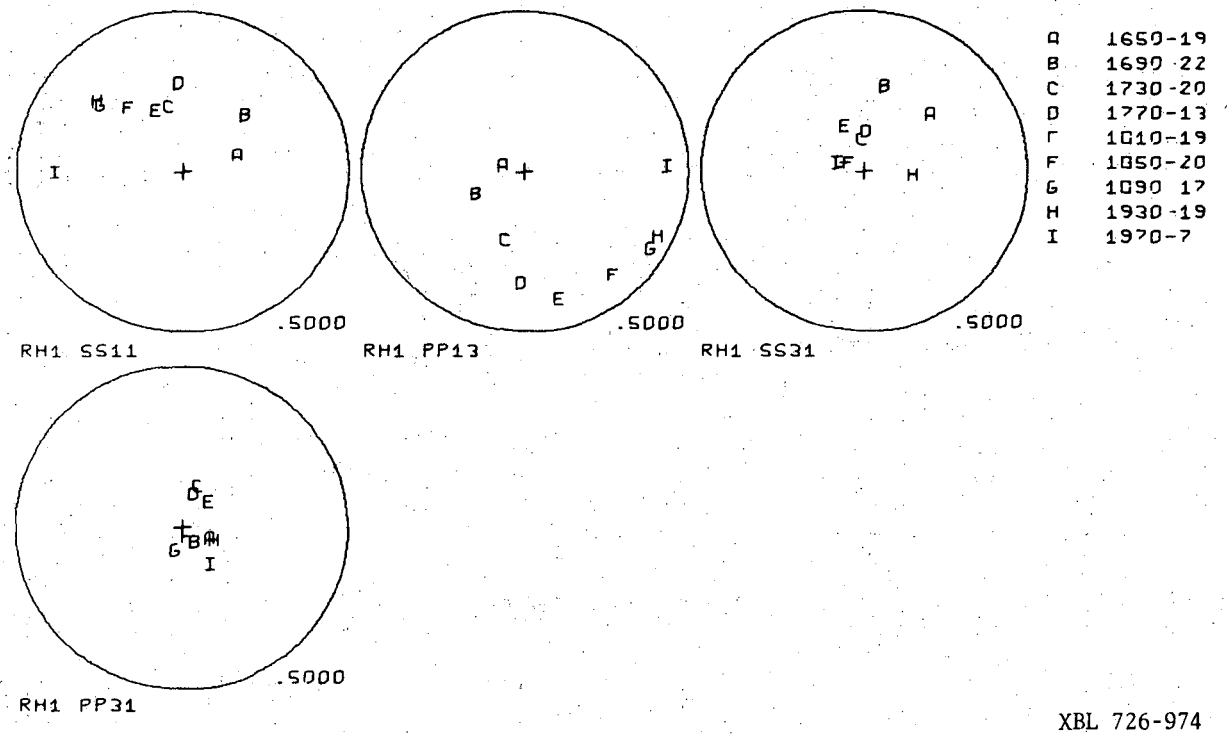

XBL 726-974

Fig. 27.

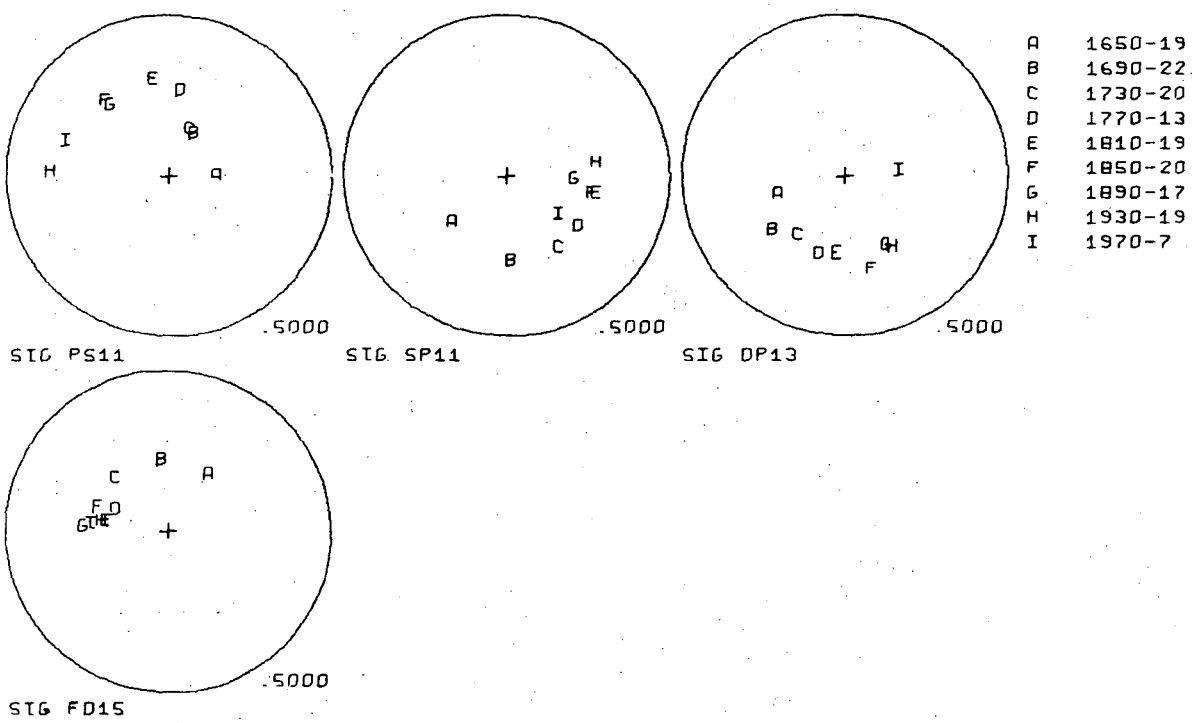

XBL 726-975

Fig. 28.

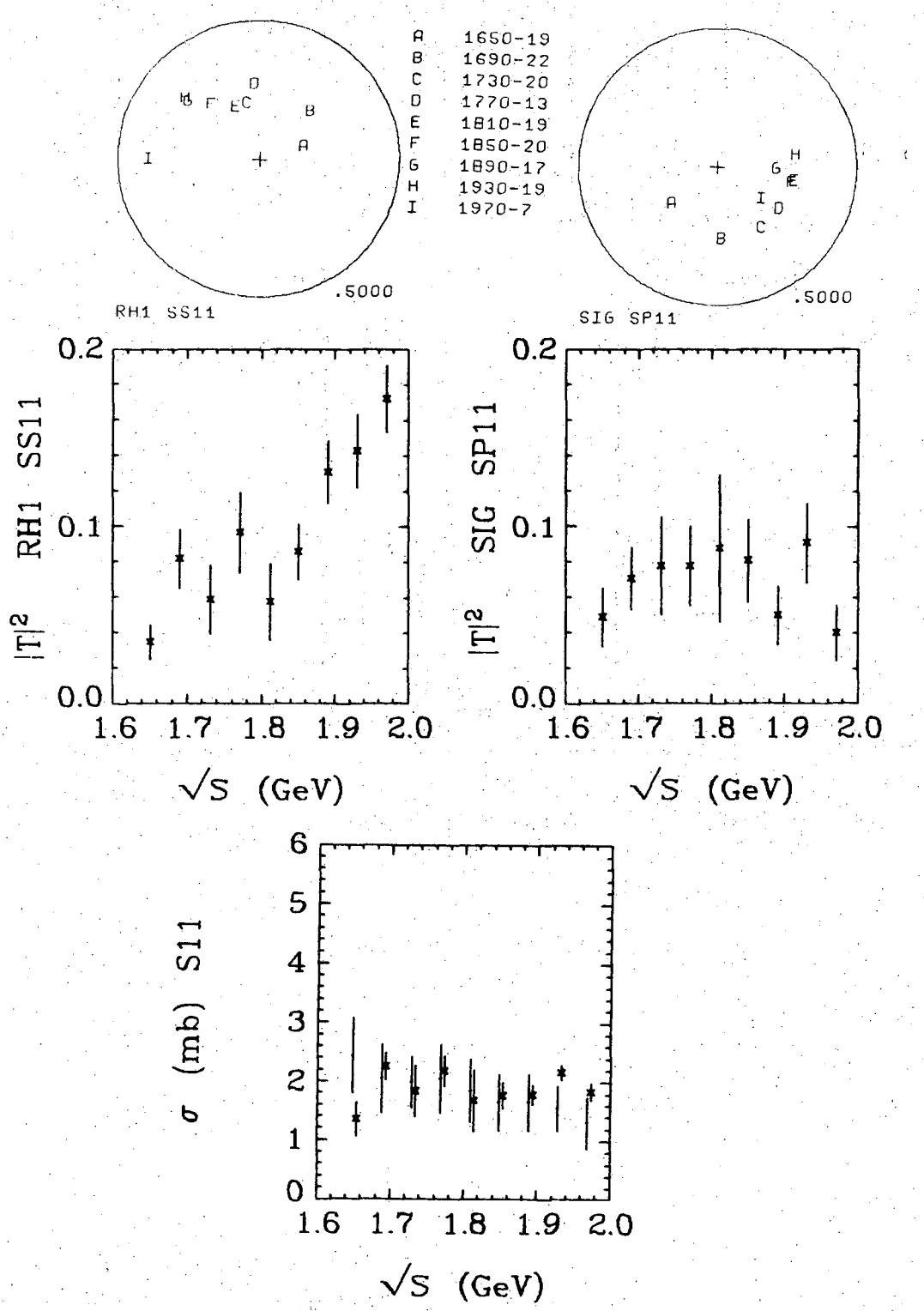

XBL 726-976

Fig. 29.

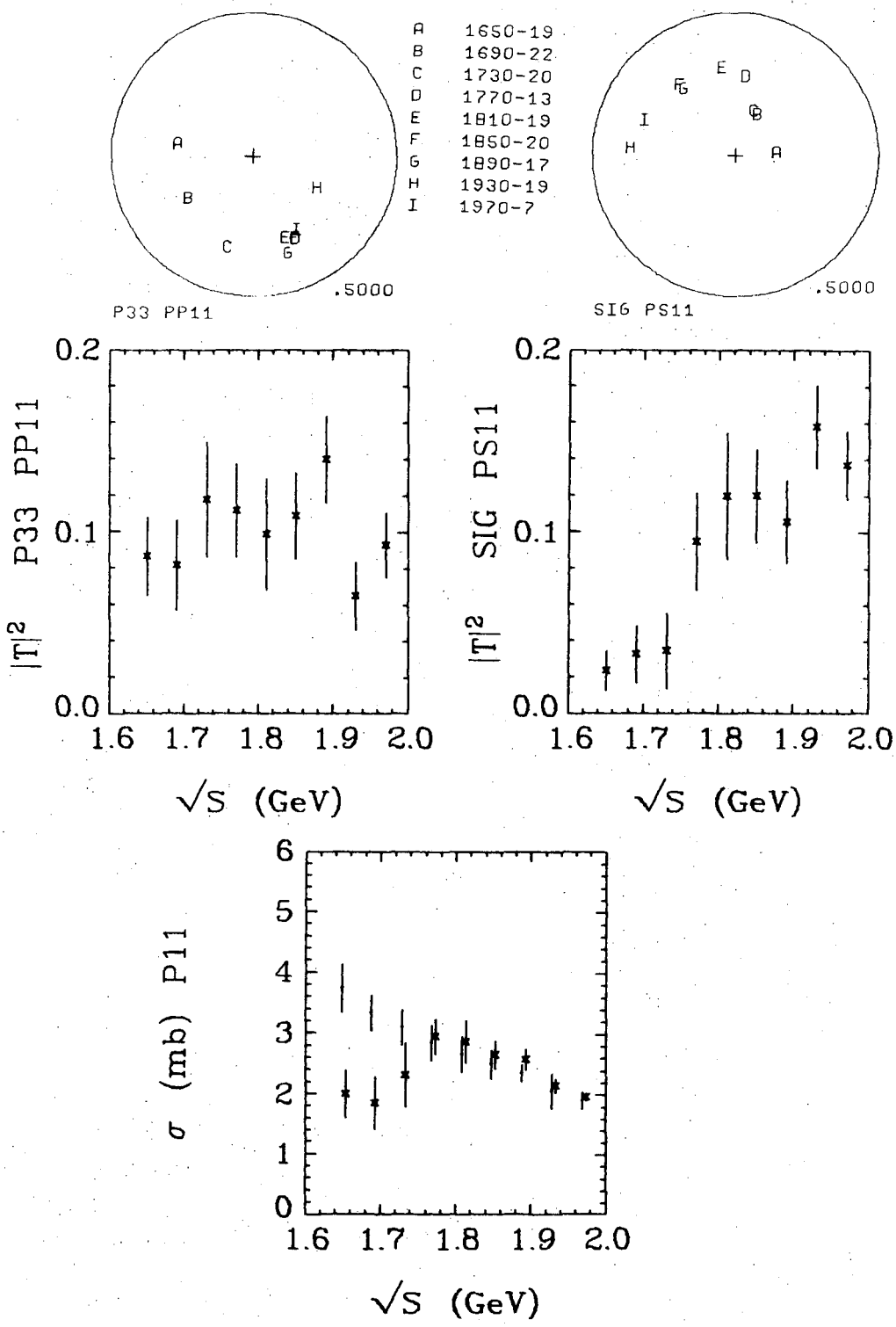

XBL 726-977

Fig. 30.

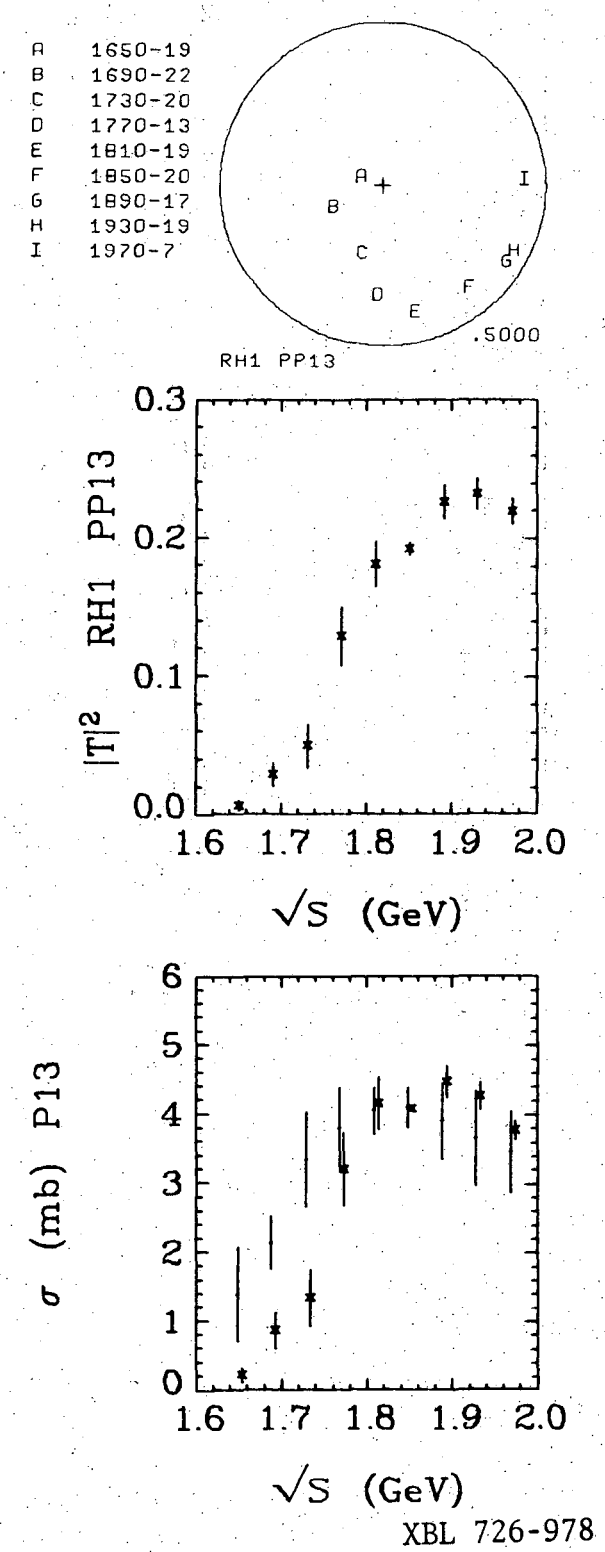
A 1650-19
B 1690-22
C 1730-20
D 1770-13
E 1810-19
F 1850-20
G 1890-17
H 1930-19
I 1970-7
A
B
C
D
E
F
G
H
I
.5000
RH1 PP13
$|T|^2$ RH1 PP13
0.3
0.2
0.1
0.0
1.6 1.7 1.8 1.9 2.0
√S (GeV)
σ (mb) P13
6
5
4
3
2
1
0
1.6 1.7 1.8 1.9 2.0
√S (GeV)
XBL 726-978

Fig. 31.

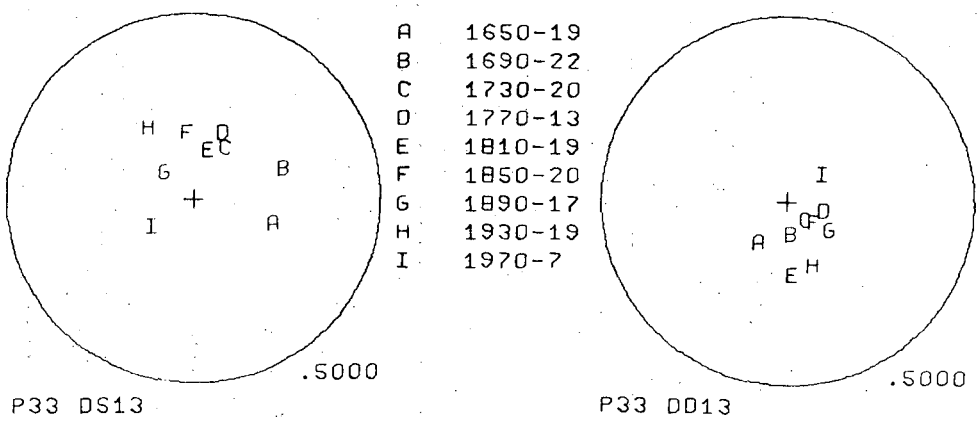

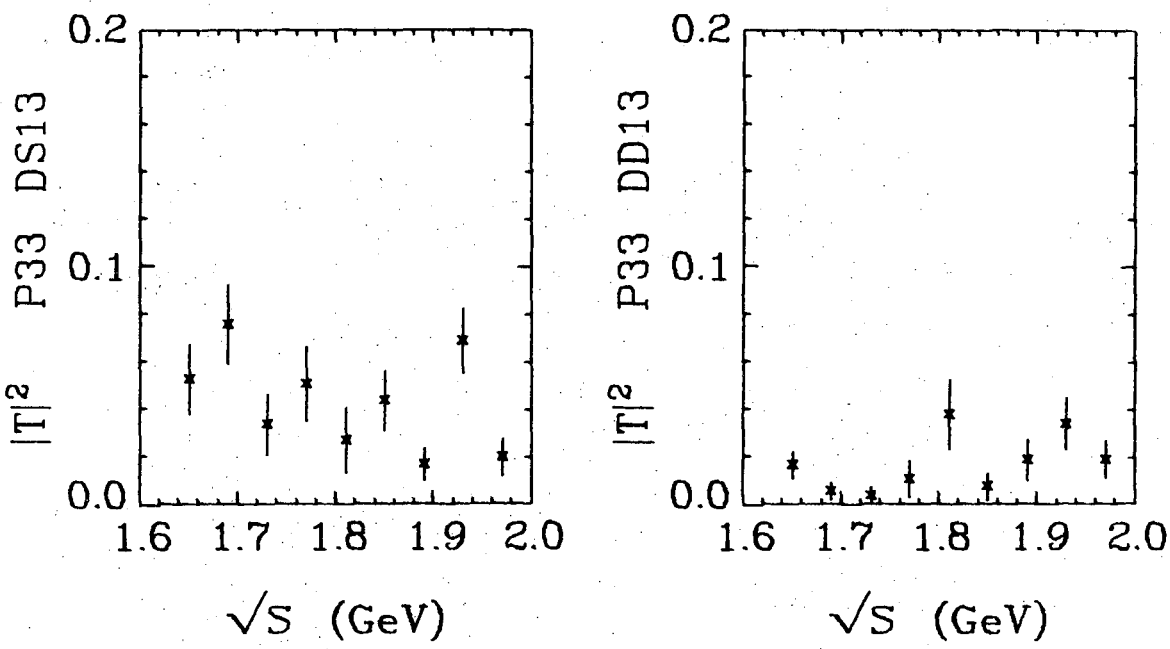

XBL 726-979

Fig. 32a.

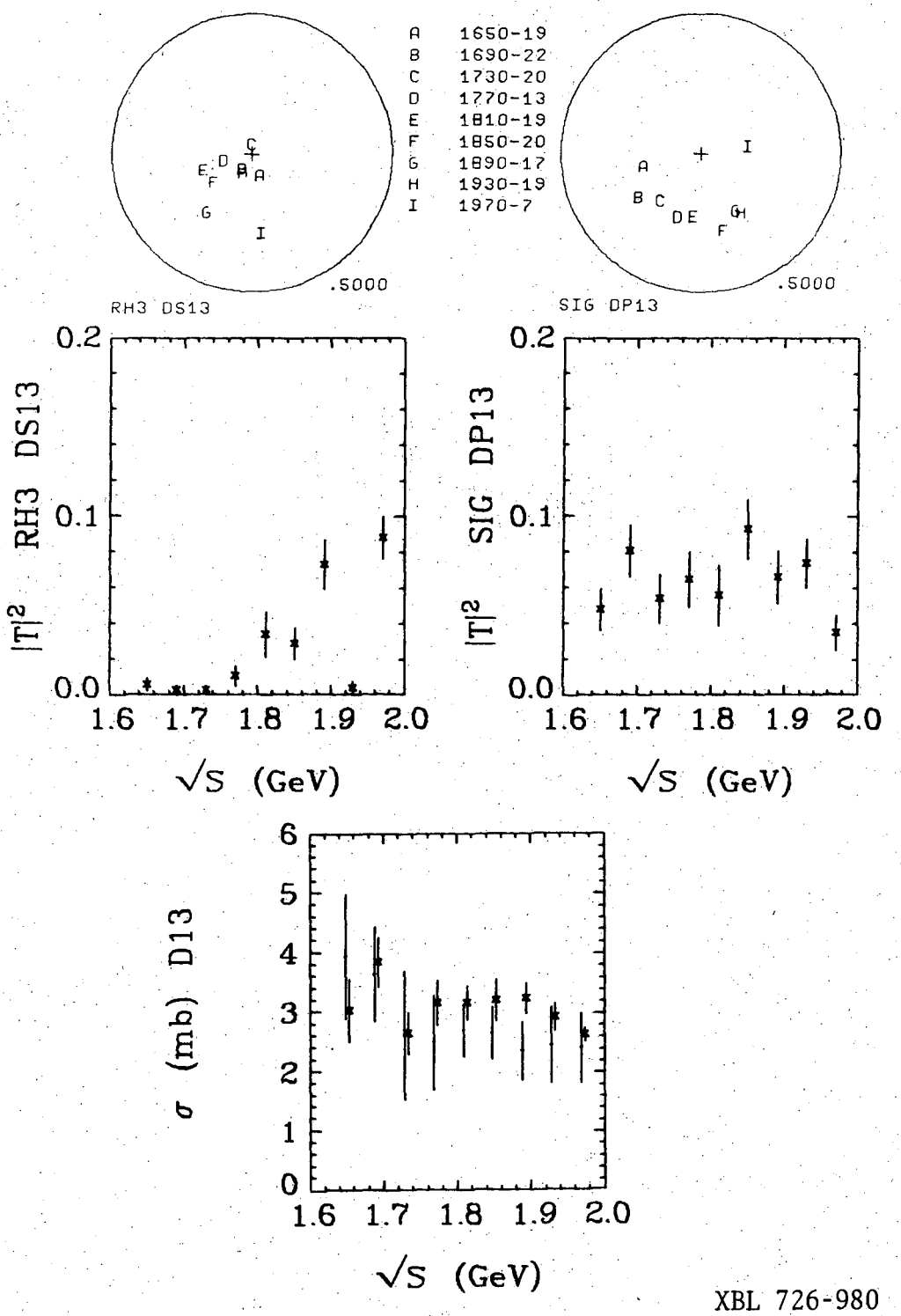
A 1650-19
B 1690-22
C 1730-20
D 1770-13
E 1810-19
F 1850-20
G 1890-17
H 1930-19
I 1970-7
.5000
RH3 DS13
SIG DP13
$|T|^2$ RH3 DS13
$|T|^2$ SIG DP13
$\sqrt{s}$ (GeV)
σ (mb) D13
XBL 726-980

Fig. 32b.

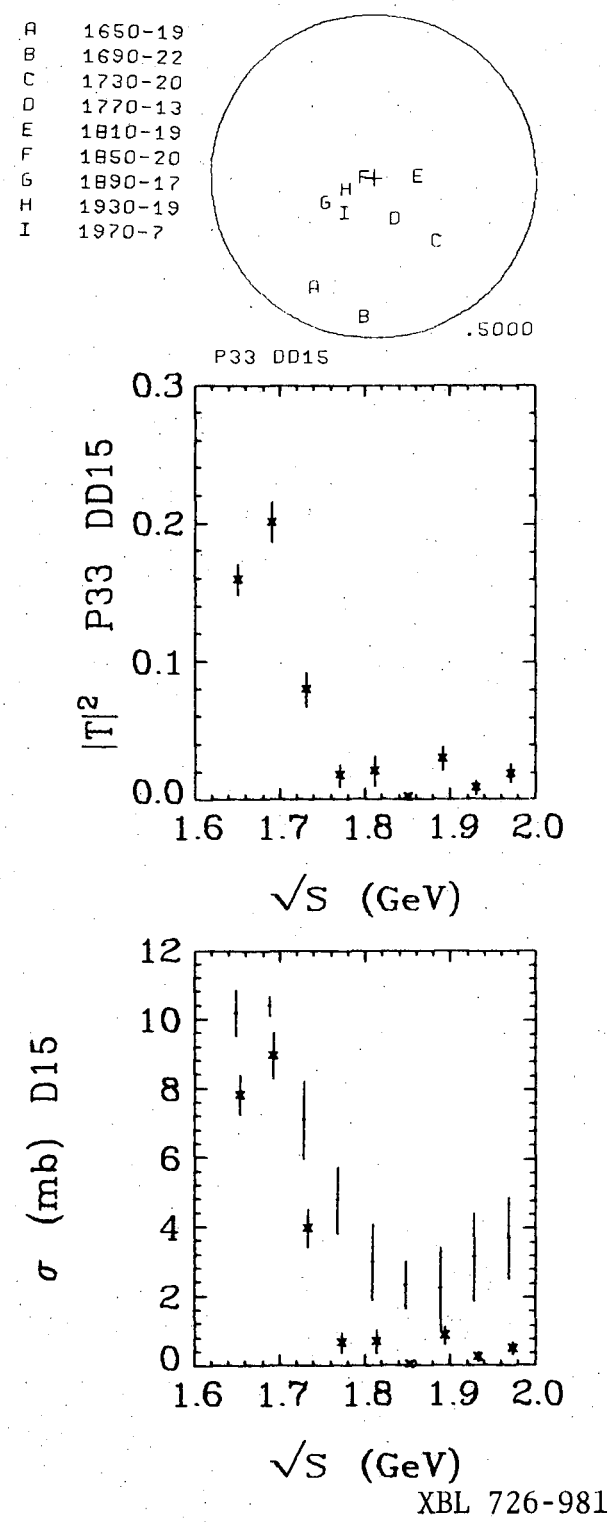
A 1650-19
B 1690-22
C 1730-20
D 1770-13
E 1810-19
F 1850-20
G 1890-17
H 1930-19
I 1970-7
.5000
P33 DD15
$|T|^2$ P33 DD15
0.3
0.2
0.1
0.0
1.6 1.7 1.8 1.9 2.0
$\sqrt{s}$ (GeV)
σ (mb) D15
12
10
8
6
4
2
0
1.6 1.7 1.8 1.9 2.0
$\sqrt{s}$ (GeV)
XBL 726-981

Fig. 33.

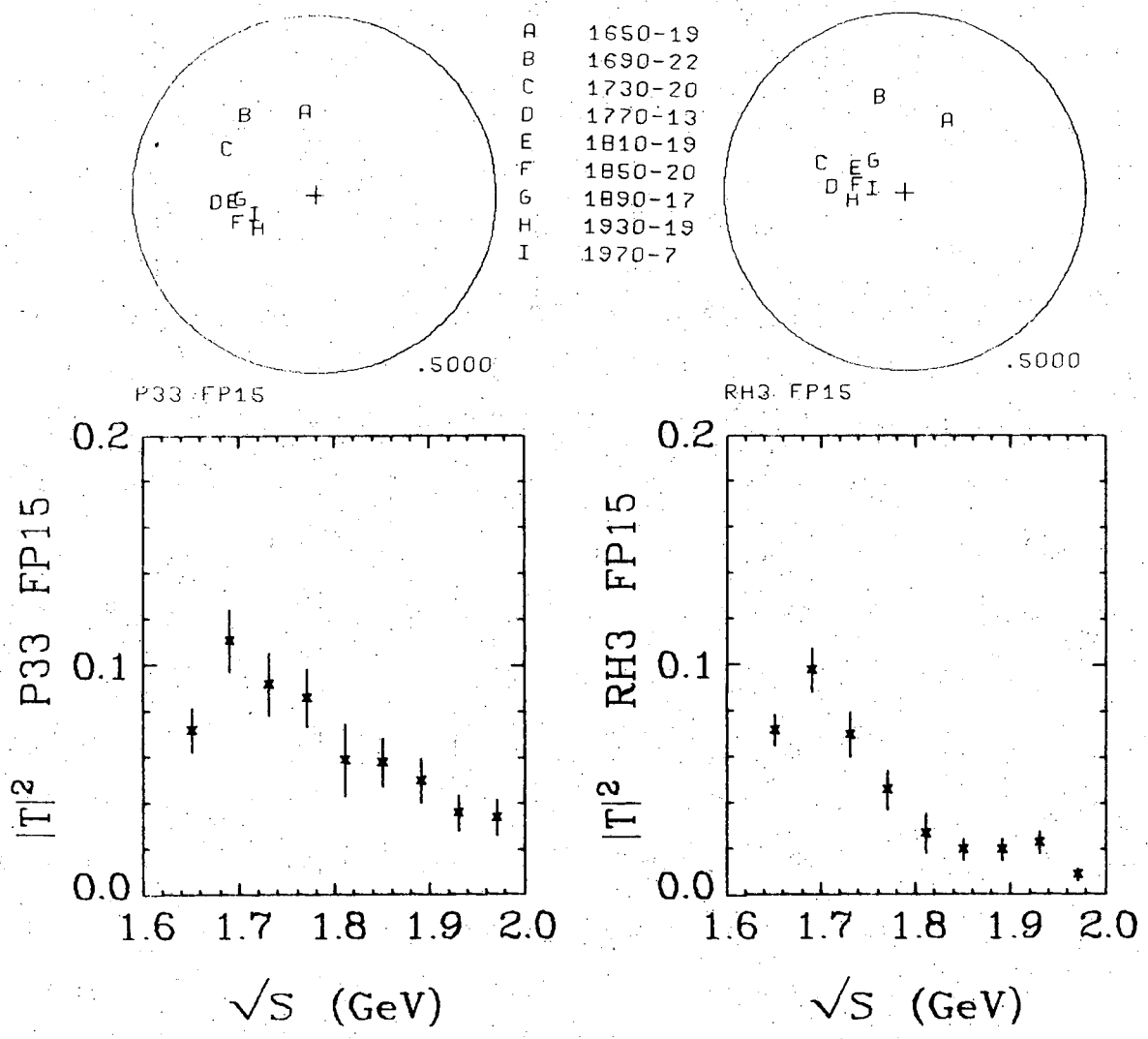

XBL 726-982

Fig. 34a.

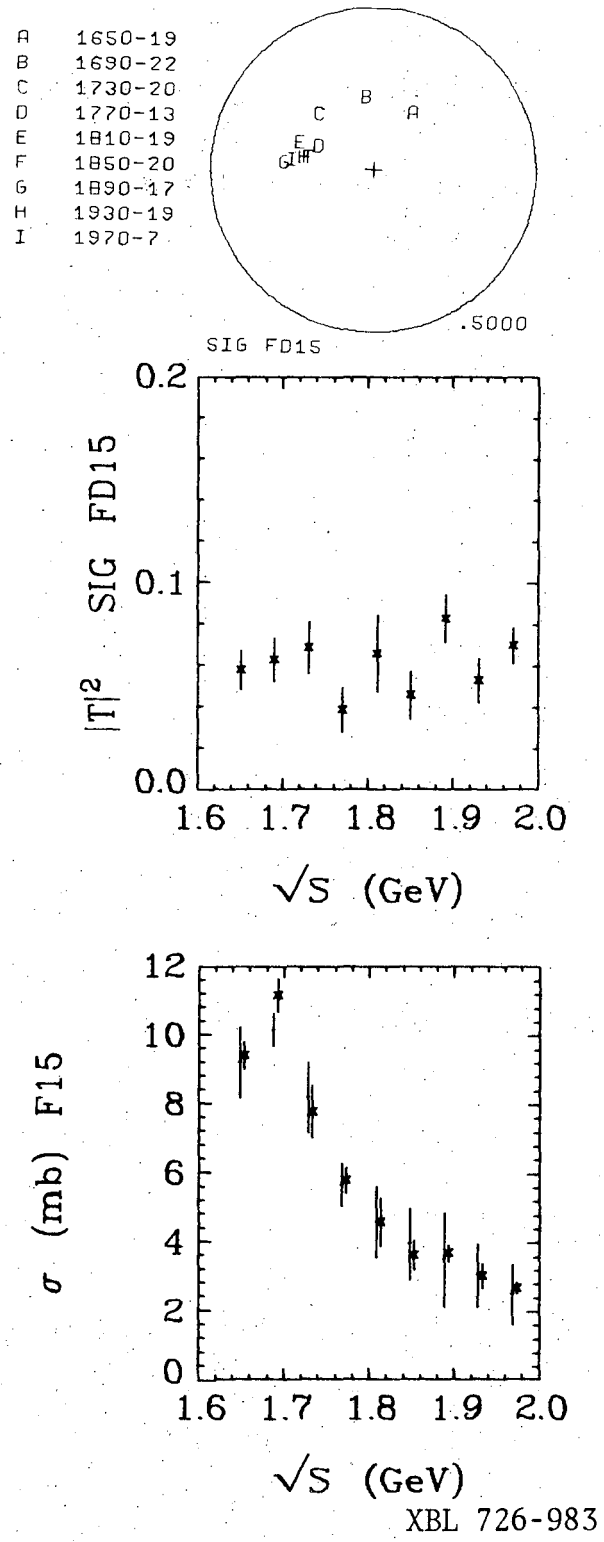
A 1650-19
B 1690-22
C 1730-20
D 1770-13
E 1810-19
F 1850-20
G 1890-17
H 1930-19
I 1970-7
.5000
SIG FD15
$|T|^2$ SIG FD15
0.2
0.1
0.0
1.6 1.7 1.8 1.9 2.0
$\sqrt{S}$ (GeV)
σ (mb) F15
12
10
8
6
4
2
0
1.6 1.7 1.8 1.9 2.0
$\sqrt{S}$ (GeV)
XBL 726-983

Fig. 34b.

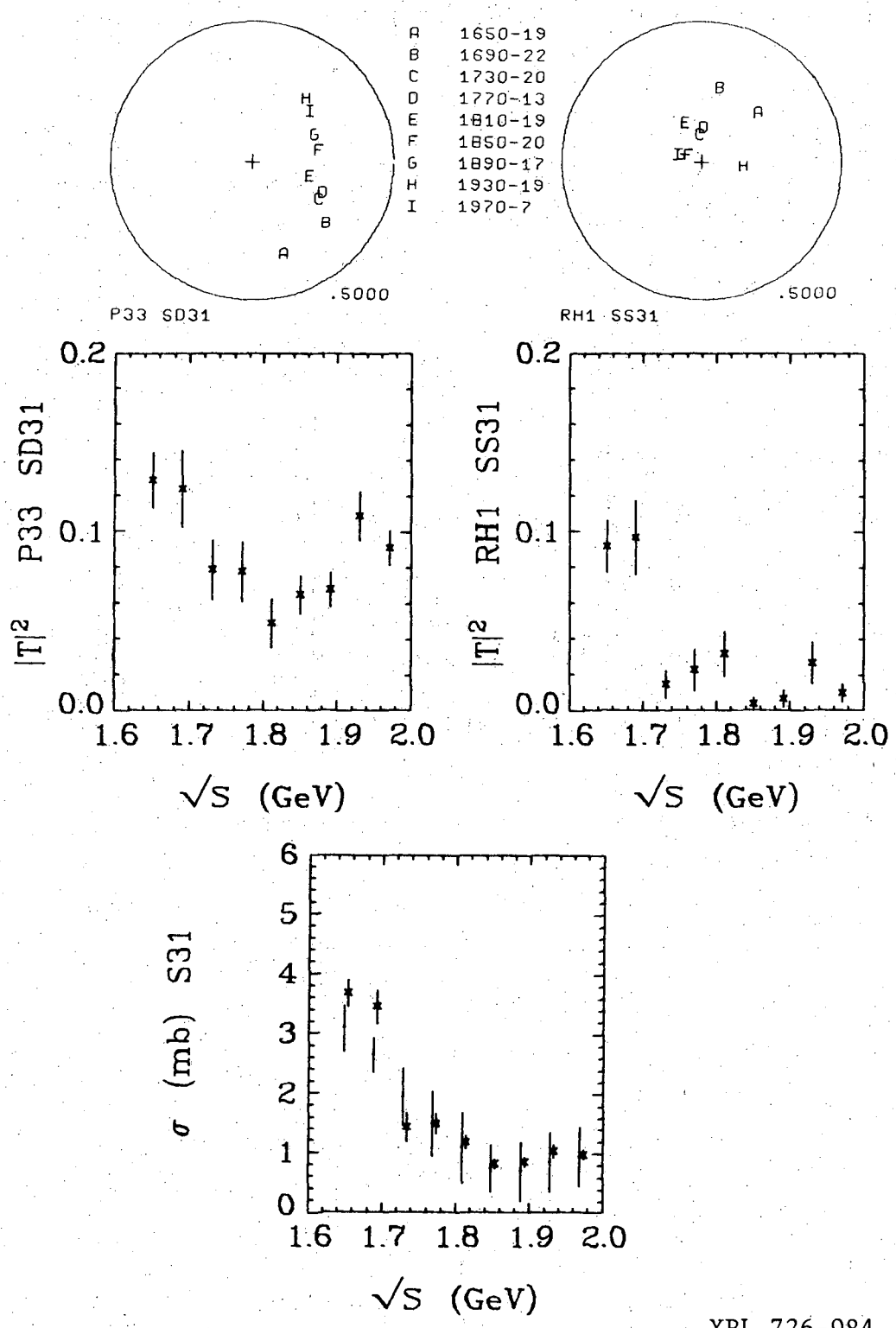

XBL 726-984

Fig. 35.

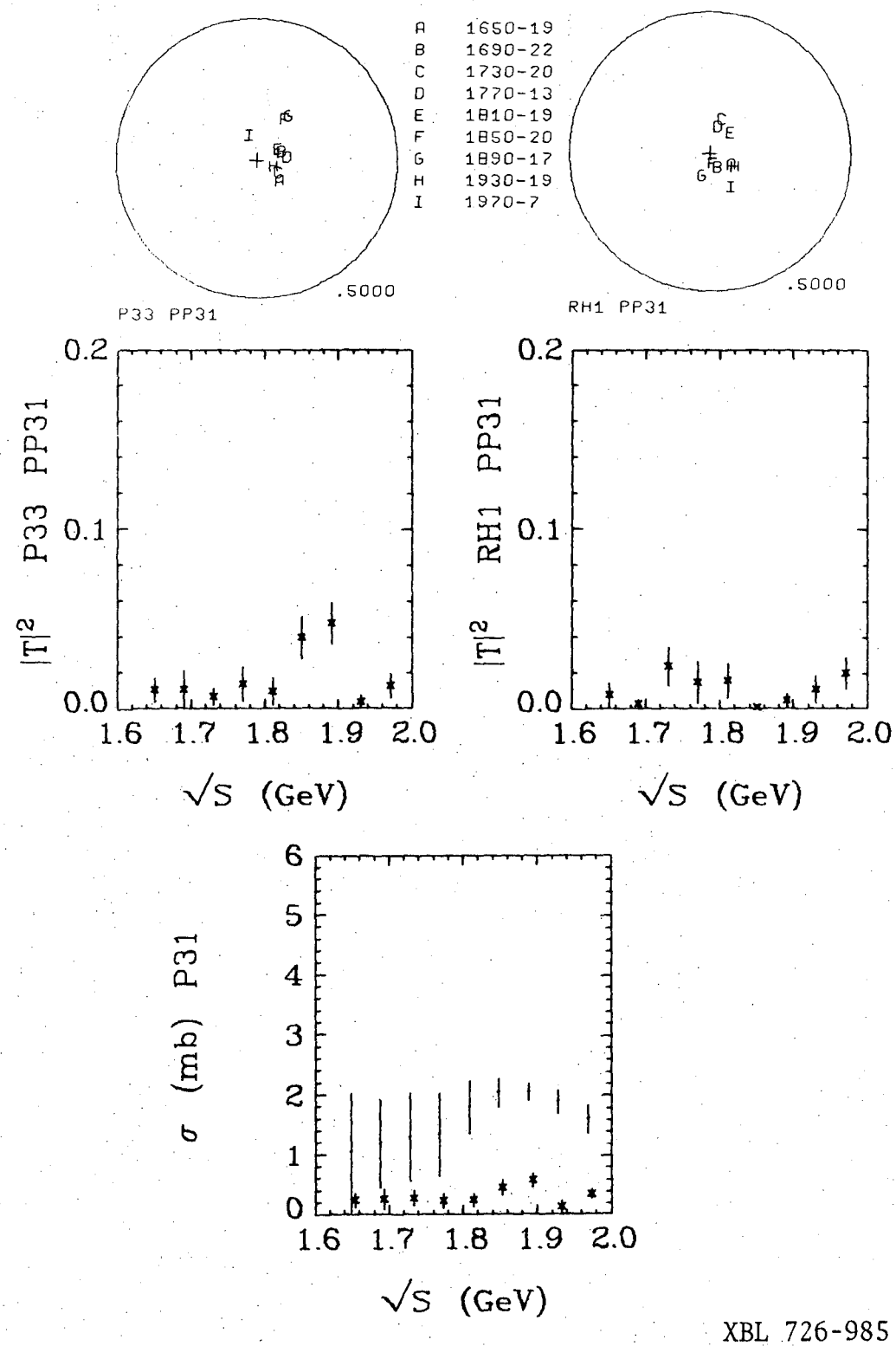

XBL 726-985

Fig. 36.

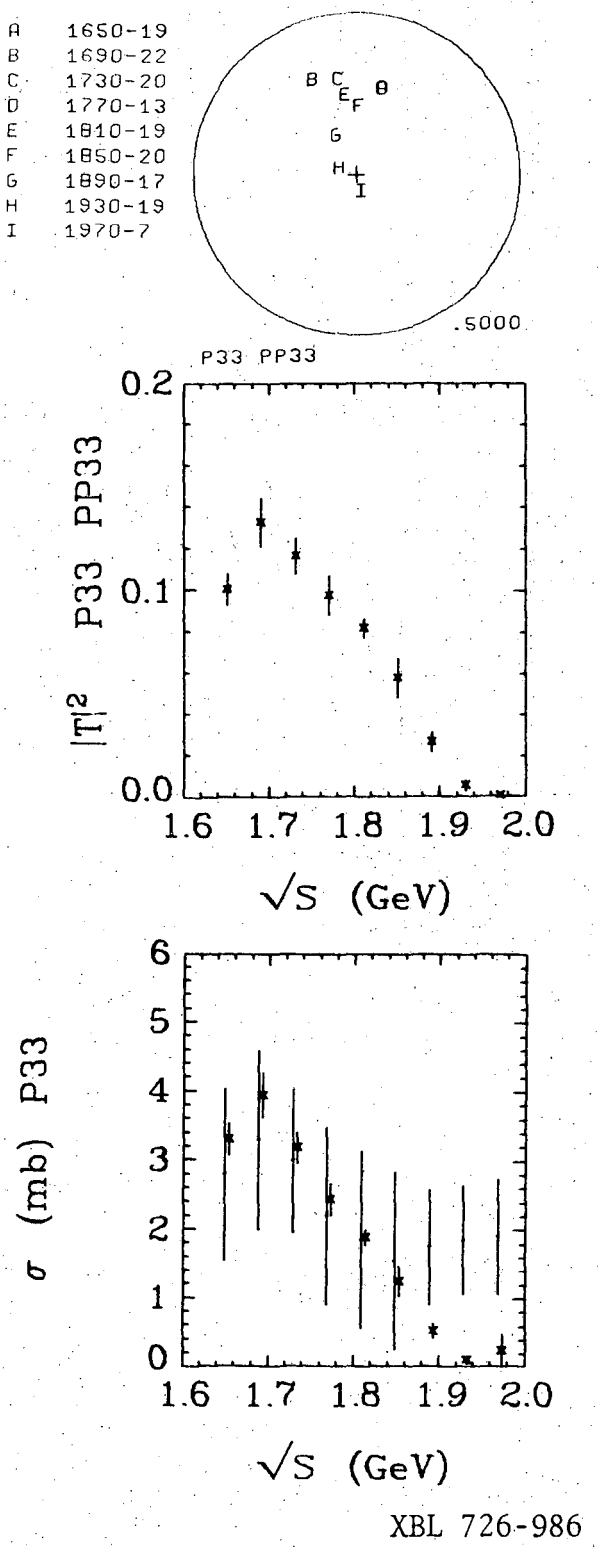

XBL 726-986

Fig. 37.

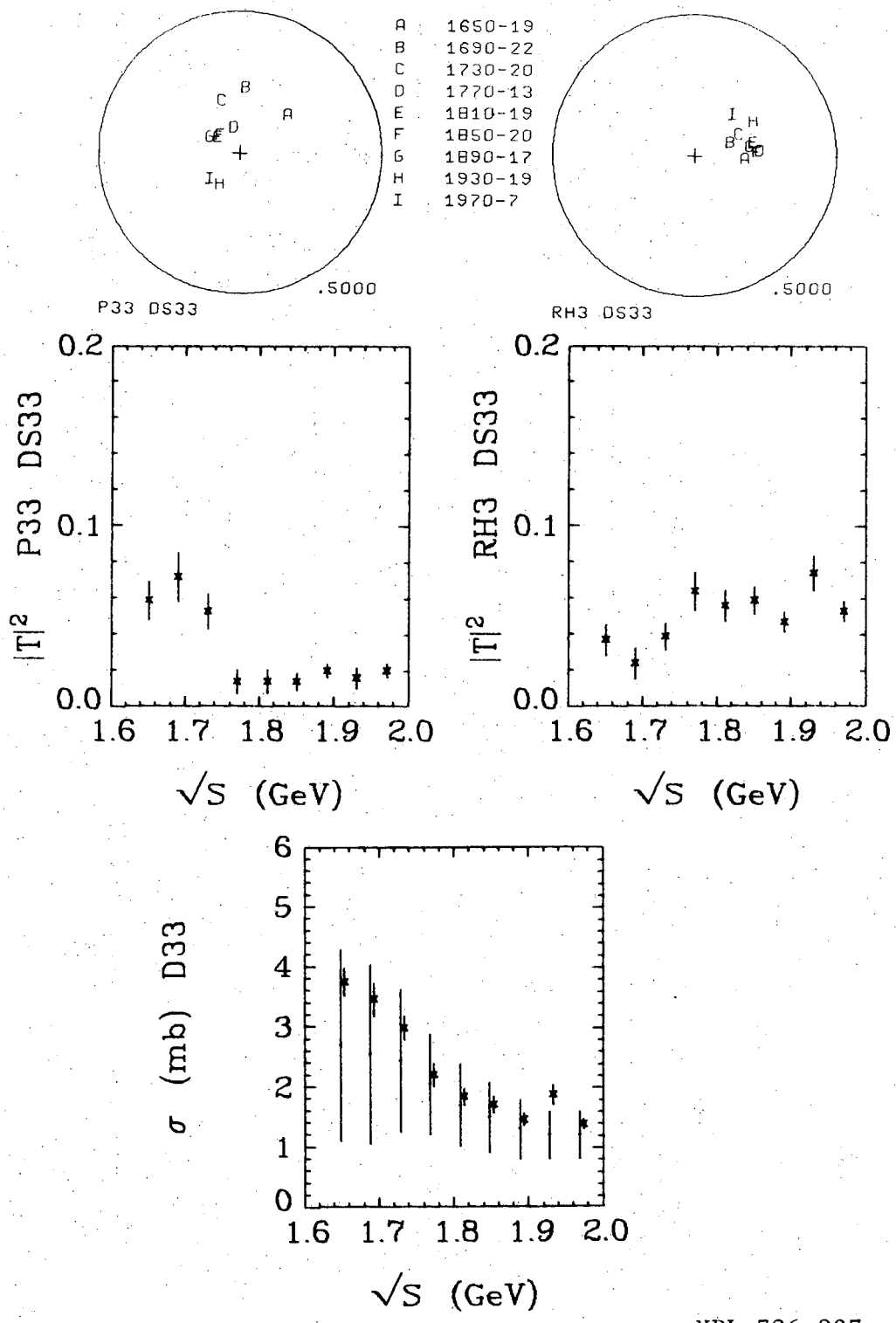

XBL 726-987

Fig. 38.

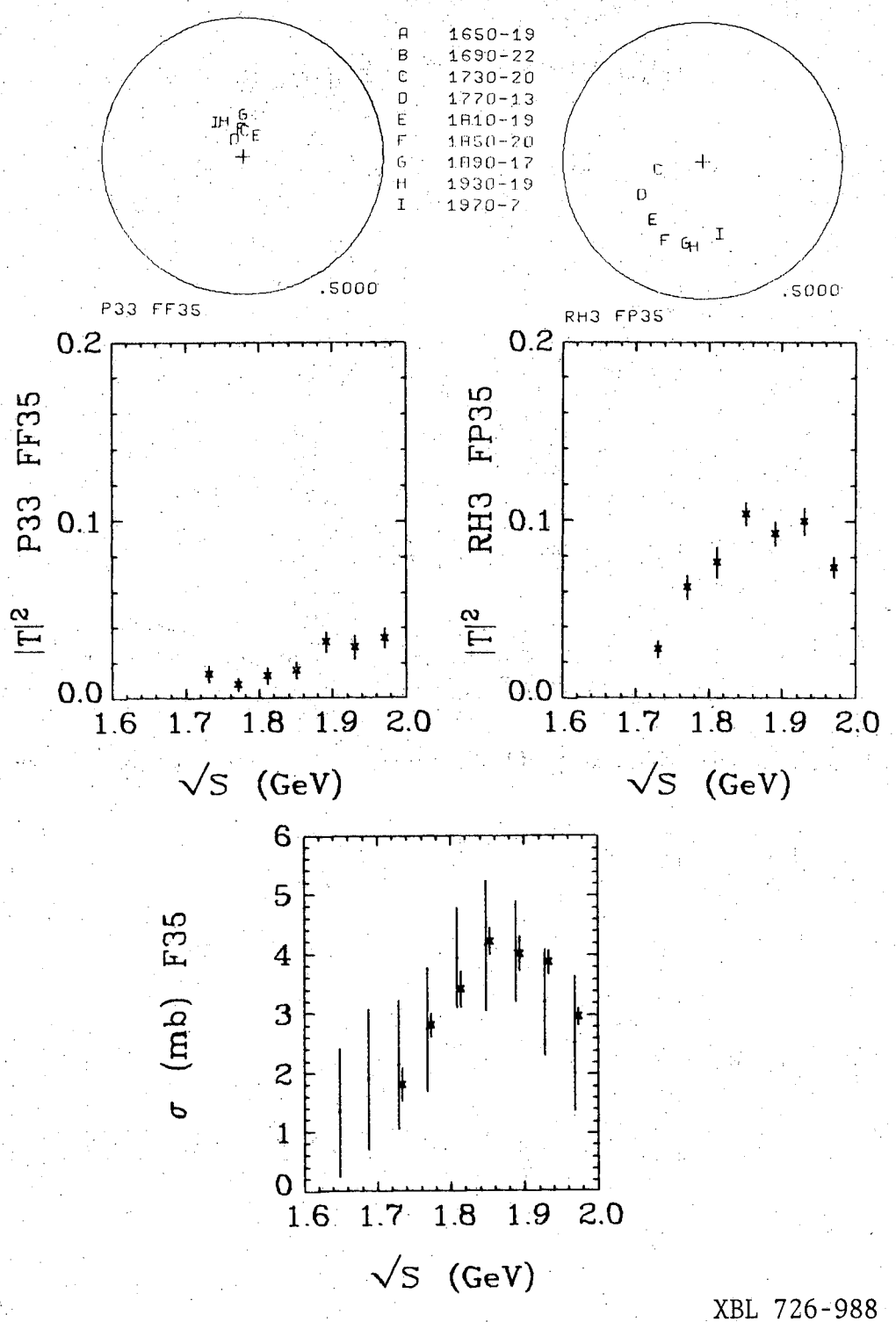

XBL 726-988

Fig. 39.

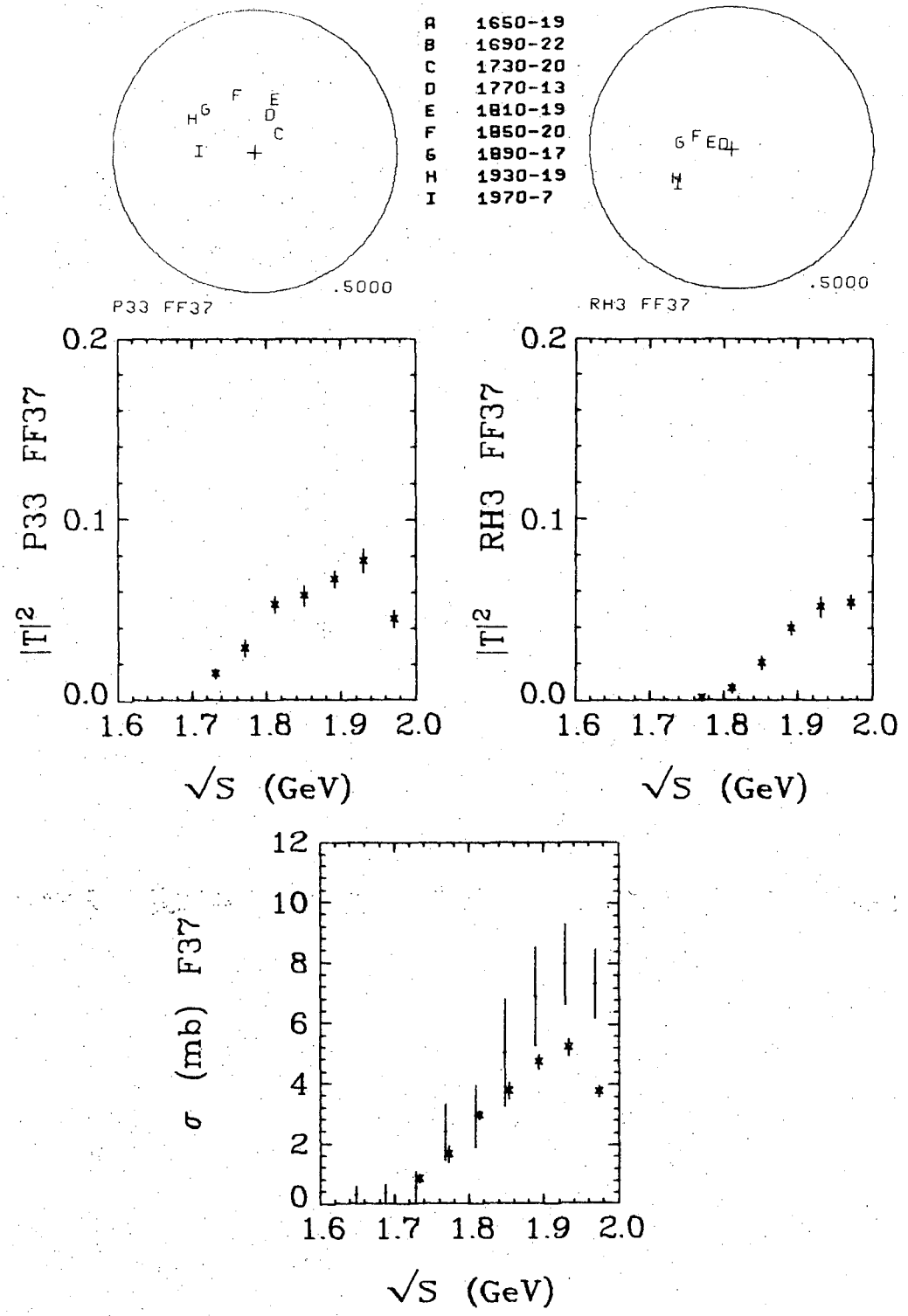

XBL 726-989

Fig. 40.

APPENDIX I

In this Appendix, we wish to review another property of the variance matrix, E, and the second derivative matrix, D, where D is E^{-1}. E (or D) is positive definite. This is necessary to insure a maximum in the likelihood, $\mathcal{L}$, rather than a saddle point or a minimum.

Defining the origin of the parameter space to be at the maximum, we can write

$$\mathcal{F} = \ell n \mathcal{L} = \ell n \mathcal{L}_0 - 1/2 \chi^2 \tag{A.1}$$

and near the origin we can expand χ^2 as

$$\chi^2 = \underset{\sim}{A} \cdot D \cdot \underset{\sim}{A} \tag{A.2}$$

The surface, enclosing the origin, defined by $1 = \underset{\sim}{A} \cdot D \cdot \underset{\sim}{A}$ is known as the error ellipsoid. This surface intercepts each axis at the points

$$A_i^{int} = (D_{ii})^{-1/2}. \tag{A.3}$$

This is sketched, in two dimensions, in Fig. A.1. It can be shown* that the planes defining the circumscribed box intercept the axes at the points A_i^{max}, given by

$$A_i^{max} = (E_{ii})^{1/2} \equiv \delta A_i. \tag{A.4}$$

(The plane $A_1 = A_1^{max} = \delta A_1$ is the dashed line of Fig. A.1). In A.4 we have written

$$E = \begin{pmatrix} \delta A_1 \delta A_1 & \delta A_1 \delta A_2 c_{12} & \cdots & \delta A_1 \delta A_n c_{1n} \\ \delta A_1 \delta A_2 c_{12} & \delta A_2 \delta A_2 & \cdots & \delta A_2 \delta A_n c_{2n} \\ \vdots & & & \\ \delta A_1 \delta A_n c_{1n} & \delta A_2 \delta A_n c_{2n} & \cdots & \delta A_n \delta A_n \end{pmatrix} \tag{A.5}$$

* Rosenfeld, A.H. and Solmitz, F.T. Lawrence Berkeley Laboratory Group A Memo 753 (unpublished, 1972).

and $|c_{ij}| < 1$ and are the correlation coefficients. Now (as is evident from Fig. A.1)

$$(D_{ii})^{-1/2} \leq \delta A_i \qquad (A.6)$$

and the equality holds if and only if $c_{ij} = 0$ for all $j \neq i$. Thus one can get a measure of how strong the correlations are by comparing $(D_{ii})^{-1/2}$ with δA_i.

In Table AI we compare δA_i and $(D_{ii})^{-1/2}$ for all the waves at a typical energy, $\sqrt{s}$ = 1690 MeV. Note that there are three entries for $(D_{ii})^{-1/2}/\delta A_i$, which exceed 1.0, one of them by 20%! This difficulty presumably has to do with invalid approximations in the inversion of D. Remember that we fit in a space of two too many variables; i.e., we use the real and imaginary part of all amplitudes, even though the overall amplitude and phase are undetermined. Therefore, D is singular, and we have to subtract two eigenvalues -- see Eq. 14 of Miller's thesis, Ref. 4. Apparently approximations in this procedure can introduce errors at the 10-20% level.

Table AI. Comparison of δA_i and $(D_{ii})^{-1/2}$ for all the waves at a typical energy, $\sqrt{s}$ = 1690 MeV.

		Re			Im		
		δA_i	$(D_{ii})^{-1/2}$	$(D_{ii})^{-1/2}/\delta A_i$	δA_i	$(D_{ii})^{-1/2}$	$(D_{ii})^{-1/2}/\delta A_i$
P33	PP11	0.0755	0.0630	0.834	0.0734	0.0528	0.719
	DS13	0.0206	0.0162	0.786	0.0208	0.0144	0.692
	DD13	0.1520	0.1281	0.843	0.1223	0.1036	0.847
	FP15	0.0589	0.0382	0.649	0.0392	0.0288	0.735
	DD15	0.1916	0.1021	0.533	0.1269	0.1269	0.551
	PP31	0.0913	0.0745	0.816	0.0642	0.0533	0.830
	SD31	0.2283	0.1944	0.852	0.1589	0.1346	0.847
	DS33	0.0264	0.0194	0.735	0.0189	0.0134	0.709
	PP33	0.1006	0.0689	0.685	0.0295	0.0327	> 1
	FF35						
	FF37						
RH3	DS13	0.0973	0.0767	0.788	0.0882	0.0647	0.734
	FP15	0.3184	0.2347	0.737	0.1910	0.1493	0.782
	DS33	0.980	0.0742	0.757	0.0979	0.0701	0.716
	FP35						
	FF37						
RH1	SS11	0.1111	0.0976	0.878	0.1356	0.0974	0.718
	PP13	0.3066	0.2297	0.749	0.2924	0.2474	0.846
	SS31	0.1549	0.1198	0.773	0.1414	0.1037	0.733
	PP31	0.5790	0.4471	0.772	0.4885	0.4268	0.874
SIG	PS11	0.2106	0.1559	0.740	0.1927	0.1675	0.869
	SP11	0.6360	0.5678	0.893	0.4441	0.4621	> 1
	DP13	0.3282	0.2855	0.870	0.3741	0.3107	0.831
	FD15	0.4801	0.5859	> 1	0.6085	0.5367	0.882

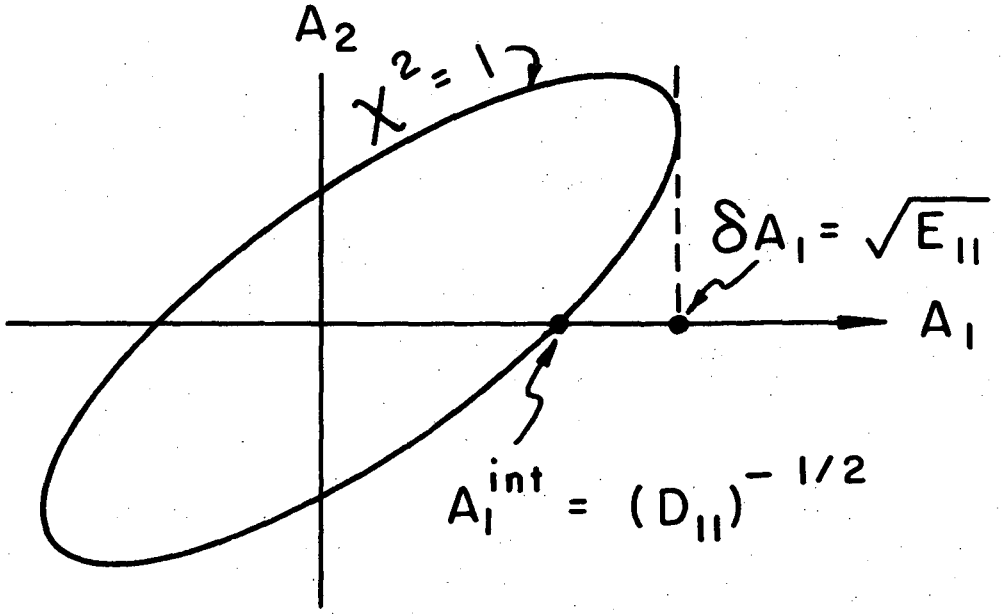

XBL727-3577

Fig. A.1

TECHNICAL INFORMATION DIVISION
LAWRENCE BERKELEY LABORATORY
UNIVERSITY OF CALIFORNIA
BERKELEY, CALIFORNIA 94720